

# **SENSR Data Quality Simulations Final Report**

F. Nai, J. Boettcher, D. Schwartzman, C. Curtis, and S. Torres

Cooperative Institute for Mesoscale Meteorological Studies, University of Oklahoma  
and NOAA/National Severe Storms Laboratory

Norman, OK

December 2019

## **Executive Summary**

Through a Service Life Extension Program (SLEP), the National Weather Service (NWS) will extend the operational capability of the current Weather Surveillance Radar-1988 Doppler (WSR-88D) until 2040. Thus, the National Weather Service (NWS) will need to make a key decision by the late 2020s: either continue maintaining the current system or replace it with a new radar system. Effectively informing this important decision requires an improved understanding of the tradeoffs between system performance and cost for any future replacement system. One critical aspect of system performance is the quality of the radar data that are used by NWS forecasters and automated algorithms (e.g., Quantitative Precipitation Estimation) to serve the critical NWS mission of protecting lives and property. A replacement system has to meet the specified technical requirements to achieve the desired data quality. There is a direct relationship between system requirements and cost; that is, the more stringent the requirements, the higher the cost. Therefore, to properly assess the tradeoffs between system performance and cost, decision makers should understand the impacts that differing levels of radar data quality have on users.

To support NWS decision makers' eventual selection of the WSR-88D replacement system, we conducted a qualitative assessment of the impact of different types of data quality changes on forecasters' interpretation of radar data. We chose to focus on the impacts on forecasters' interpretation because radar data are the primary source of information that support a variety of forecasts and warnings for hazardous weather events that directly address the NWS mission. Our goal was to understand the relationship between several sources of potential data quality change and their associated impacts on forecasters' interpretation of the data. To achieve this, we utilized a novel approach that involved radar engineers and meteorologists working together through cycles of developing and improving a unique, high-fidelity radar-data simulator,

selecting appropriate weather cases, and analyzing the simulated data to assess data quality impacts.

Our study evaluated three radar design parameters that directly affect data quality and system cost. We developed and implemented simulation and analysis methodologies that included independent qualitative assessments of the impact on forecasters' interpretation of radar data. The three radar design parameters for this study were: 1) spatial resolution (i.e., the sidelobe levels and the beamwidth of the antenna radiation pattern), 2) azimuthal sampling (i.e., the placement and width of radials in a radar image), and 3) system sensitivity (i.e., the minimum detectable signal by the radar).

For spatial resolution, we performed two separate studies: one focused on the impact of changing the antenna radiation pattern sidelobe levels and the other on its beamwidth. To qualitatively assess the impact of changing antenna sidelobe levels, we simulated data from 13 supercell storms. The selected supercell cases have a characteristic structure likely to cause sidelobe contamination that may disrupt data interpretation during severe weather warning operations. For each supercell storm case, we simulated 10 sets of radar data as though collected by radars with antennas exhibiting different sidelobe levels. An experienced forecaster with both operational and training experience served as a representative of the NWS forecaster population and analyzed the simulated radar data using a process that is similar to the real-time data analysis used during warning operations. Her assessment used a five-level scoring system based on her evaluation of the extent that the sidelobe contamination present in the data would affect forecasters' interpretation of the weather event. Using these scores, we constructed an impact model that could be used by decision makers to evaluate the impact of different radar antenna-

radiation-pattern sidelobe levels on forecasters' data interpretation for mission-critical severe weather events.

The second aspect of spatial resolution that we evaluated in this study is the beamwidth of the antenna radiation pattern. Since planar phased-array radar (PAR) is a promising candidate as the replacement system for the WSR-88D due to its rapid update capability, we studied the impact of beam broadening on forecasters' interpretation of radar data. We simulated and compared radar data from a PAR (with a beamwidth that increases as the radar beam is steered away from broadside) to data from two dish-antenna systems (with constant beamwidth as a function of scan angle). Because the beamwidth of the antenna pattern can affect the observation of important weather features in radar images, our assessment of the impact of beam broadening was based on the preservation and observation of important weather features in a wide variety of hazardous weather events. Our preliminary results showed that the PAR beam broadening effect did not result in any artifacts or misrepresentations in radar data that would negatively affect forecasters' interpretation of that data. Moreover, we showed that a planar PAR system that satisfies the current beamwidth requirements (i.e., beamwidth  $\leq 1^\circ$  for all scanning angles) performs similarly to the WSR-88D for a large majority of non-circulation cases. Such a PAR also performs better than the WSR-88D for circulation cases if other aspects (e.g. sidelobe levels, sensitivity, azimuthal sampling, etc.) of the two radar systems are identical. Furthermore, our preliminary results showed that a PAR with four stationary faces must satisfy the current beamwidth requirements to prevent negative impacts on forecasters. On the other hand, a rotating PAR with limited electronic steering in azimuth (e.g., within  $\pm 22.5^\circ$  of array broadside) could still perform similarly to the WSR-88D even if does not meet the current requirements (i.e., its beamwidth is greater than  $1^\circ$  for some scanning angles).

The second parameter of data quality change we studied is the placement of the azimuthal sampling grid, which determines the location of radials in a radar image. Of the weather events that we studied, effective sampling of circulations was particularly sensitive to the placement of the azimuthal sampling grid. We first compared simulated PAR data on a sampling grid similar to the grid used by the WSR-88D (i.e., adjacent radials were spaced half a beamwidth apart for super-resolution data) to PAR data on a grid with variable spacing between adjacent radials. Each comparison was assessed based on the presentation and preservation of important weather features. Our results showed that denser sampling grids are always better for non-circulation cases. On the other hand, we initially showed that for circulation cases, which are crucial to the NWS mission, there is no single preferred sampling grid. To further investigate the impact of the azimuthal sampling grid on radar observation of circulations, we used systematic simulations to quantify changes to the radar-estimated rotational velocity, a commonly used indicator of circulation strength, for a variety of circulations with different sizes and at different ranges. In this study, we kept the effective beamwidth of the radar constant and evaluated sampling grids with azimuthal sampling intervals of  $1^\circ$ ,  $0.5^\circ$ ,  $0.25^\circ$ , and  $0.125^\circ$ . That is, we evaluated the effects of using sampling grids with increasingly overlapped radials on the resulting radar estimate of the rotational velocity of circulations. We also systematically shifted the sampling grid by small increments in azimuth to evaluate the performance of the different sampling grids for all possible relative positions of the sampling grid with respect to the center of a circulation. Our preliminary results showed that reducing the azimuthal sampling spacing leads to more accurate rotational velocity estimates for all circulations. Moreover, it leads to estimates that are less dependent on the position of the circulation with respect to the sampling grid. This is a significant improvement to the interpretation of radar data because any short-term variations in observed circulation strength can

be mostly attributed to storm evolution and not to radar sampling. We further validated these simulation results by re-processing raw data from a tornadic supercell as observed by the National Severe Storms Laboratory (NSSL) research WSR-88D. The results largely matched our simulation results and showed the same enhanced circulation patterns.

The last parameter of radar design we studied in the context of data quality and system cost is sensitivity. For this parameter, we simulated data for a variety of hazardous weather events as though radars with systematically differing sensitivity collected them. The simulated radar data was analyzed and assessed based on the presentation and preservation of important weather features such as the size of the storm and the detection of outflow boundaries and circulations. We quantified the assessments of our simulated data with a five-level scoring system and constructed a similar impact model as we did for the study on the impact of changing antenna sidelobe levels. With additional data from an expanded study that uses more cases, this impact model could be used by decision makers to evaluate the impact on operational forecasters for any radar system by comparing its sensitivity to that of the WSR-88D.

In summary, our study was a crucial first step to develop simulation and analysis methodologies that connect data quality changes to impact on forecasters who use radar data as a primary source of information in all types of hazardous weather warning decisions. It is important to note that our results should not be interpreted as providing recommendations for changing technical requirements for the replacement system. This is because our study was limited in scope and only focused on one part of the overall impacts caused by data quality changes: forecaster interpretation of base data. A more comprehensive study that includes many more cases, involves a diverse group of forecasters, and includes data quality impacts on algorithms will be needed to provide more valid recommendations for changing any technical requirements. Instead, our results

can be used as a proof of concept for the simulation and analysis methodologies. Eventually, the results obtained from an extension of such an approach can be used by decision makers to evaluate the possible operational impacts of any proposed radar designs, which is an important component of the evaluation of tradeoffs between system performance and cost.

While our study is an important step, there are several other areas of research that need to be conducted to support NWS decision makers on selecting a replacement system for the WSR-88D. Since phased-array technology offers additional flexibilities such as adaptive scanning and adaptive beamforming, these novel approaches should be investigated to evaluate their potential to improve radar data quality and/or meet other evolutionary requirements. For example, adaptive beamforming could adjust antenna pattern features (such as sidelobes) to improve observations of particularly threatening weather with strong reflectivity gradients (such as supercells). The Command and Control (CC) framework developed in parallel with this study can be used as a first step to investigate concept of operations that exploit adaptive scanning techniques to reduce the scan time without sacrificing spatial coverage or data quality. The CC framework is also capable of ingesting several volumes of archived data from the WSR-88D, which allows us to pick from a variety of weather events. This framework provides realistic and fair comparisons between different adaptive scanning techniques and allows emulation of different radar architectures (e.g., single rotating PAR face, four stationary PAR faces, or rotating parabolic reflector). As the Advanced Technology Demonstrator PAR system (ATD) becomes available for weather observations, we will be able to demonstrate these techniques and verify our results from the CC framework and data quality simulations. In parallel with investigations of adaptive techniques to mitigate radar data-quality challenges, a continued qualitative assessment of the resulting data interpretation impacts is recommended to keep this work salient for NWS forecasters. Our

methodologies, which directly translate radar design changes to data quality changes and their impacts to NWS forecasters, are invaluable tools that can be used to evaluate various aspects of weather radar design in future studies.

## TABLE OF CONTENTS

<b>1. INTRODUCTION .....</b>	<b>1</b>
<b>2. IMPACTS OF SPATIAL RESOLUTION .....</b>	<b>5</b>
2.1. INTRODUCTION .....	5
2.2. IMPACT OF CHANGING ANTENNA SIDELOBE LEVELS .....	7
2.2.1. <i>Simulation Methodology</i> .....	7
2.2.2. <i>Case Selection and Data Analysis Process</i> .....	24
2.2.3. <i>Simulation Results</i> .....	32
2.3. IMPACT OF BEAM BROADENING FOR PLANAR PAR.....	37
2.3.1. <i>Simulation Methodology</i> .....	37
2.3.2. <i>Case Selection and Data Analysis Process</i> .....	41
2.3.3. <i>Simulation Results</i> .....	49
2.4. CONCLUSIONS .....	52
<b>3. IMPACTS OF AZIMUTHAL SAMPLING.....</b>	<b>54</b>
3.1. INTRODUCTION .....	54
3.2. AZIMUTHAL SAMPLING FOR PAR.....	56
3.2.1. <i>Simulation Methodology</i> .....	56
3.2.2. <i>Data Analysis Process</i> .....	58
3.2.3. <i>Simulation Results</i> .....	62
3.3. AZIMUTHAL SAMPLING OF CIRCULATIONS.....	65
3.3.1. <i>Simulation Methodology</i> .....	65
3.3.2. <i>Simulation Results</i> .....	70

3.3.3. <i>Real Data</i> .....	75
3.4. CONCLUSIONS .....	83
<b>4. IMPACT OF SENSITIVITY.....</b>	<b>85</b>
4.1 INTRODUCTION.....	85
4.2 SIMULATION METHODOLOGY.....	86
4.3 CASE SELECTION AND DATA ANALYSIS PROCESSES .....	87
4.4. SIMULATION RESULTS.....	94
4.5. CONCLUSIONS .....	97
<b>5. PROJECT CONCLUSIONS .....</b>	<b>98</b>
<b>6. REFERENCES .....</b>	<b>99</b>
<b>APPENDIX A: SUMMARY OF CASES IN TABLE 2-2 .....</b>	<b>103</b>
<b>APPENDIX B: SUMMARY OF CASES IN TABLE 2-4.....</b>	<b>110</b>
<b>APPENDIX C: SUMMARY FOR CASES IN TABLE 4-1.....</b>	<b>119</b>
<b>APPENDIX D: SENSR PRELIMINARY REPORT.....</b>	<b>124</b>

## **1. Introduction**

Through a Service Life Extension Program (SLEP), the National Weather Service (NWS) will extend the operational capability of the current Weather Surveillance Radar-1988 Doppler (WSR-88D) until 2040. Thus, the National Weather Service (NWS) will need to make a key decision by the late 2020s: either continue maintaining the current system or replace it with a new radar system. The functional requirements for a replacement radar system consist of threshold requirements, which must be met by the replacement radars, and objective requirements, which the replacement radars should try to approach without compromising any threshold requirements (NOAA/NWS 2015). To meet these demanding requirements, any replacement radar system will likely involve tradeoffs between performance and cost, which must be evaluated in a manner that can lead to a preferred solution. For example, conventional radar technology (e.g., a dish-antenna system) can meet most of the threshold requirements but would have difficulties in meeting the objective one-minute-or-less volume update-time requirement. On the other hand, a four-face phased-array radar (PAR) could achieve the desired volume update time but would require a more expensive aperture to meet the angular resolution requirements. Additionally, complex calibration would be needed to ensure that the quality of the polarimetric data from a phased-array system is comparable to that of the WSR-88D (Lei et. al 2015). Radar data quality, which impacts the decisions and products generated by radar data users, is a major aspect of system performance that will be involved in the tradeoffs with system cost. Therefore, to properly balance system cost and performance, it is important for decision makers to understand the impacts of changing radar data quality on end users. Since the NWS forecasters use radar data as a primary source of information in their threat assessment and warning decisions, they are likely to be impacted by data quality changes. This

work is a first step to characterize the relationships between data quality changes and their impacts on forecasters.

Studying the impacts of data quality changes on forecasters requires both a process to produce radar data with different data quality and a method to quantify the data quality impacts. One way to produce radar data with different data quality for the same weather event is to build prototypes of different radar designs and collect data at the same time. However, this approach is expensive and impractical. A more practical way to produce radar data with different data quality for the same weather event is through realistic simulations. The Signal Processing and Radar Characteristic (SPARC) simulator offers a flexible framework for studying the impact of signal processing techniques and radar system characteristics on radar-variable estimates required to support the NWS weather-surveillance mission (Schvartzman and Curtis 2019). It is a versatile two-dimensional weather-radar time-series scenario simulator that ingests archived fields of spectral moments and polarimetric variables (also referred to as base data) and produces time-series (I/Q) data, which can be processed to produce base data as it would be observed by different radar systems. In contrast with other simulators, the SPARC simulator allows for an end-to-end evaluation that considers the interactions between radar sub-systems (e.g., the transmitter, the antenna, the receiver), scanning strategies (e.g., the pulse repetition time, the number of samples per dwell), and the signal processing. This makes the SPARC simulator a suitable tool to simulate data with different degrees of quality.

Simulated radar data with varying quality must be analyzed and compared in a systematic way to quantify the impacts on forecasters. The statistical biases and variances of the radar-variable estimates can be used to quantify the data quality changes, but they are not enough to completely characterize the impact on forecasters. For example, the spatial distribution of biases could matter

more than the magnitude of the biases when a forecaster is assessing the potential threat of a storm. To account for data quality changes that affect forecasters' interpretation of the radar data, our evaluations of the data quality impacts are based on the preservation or presentation of important weather features in the data. We developed scoring systems to quantify the amount of data quality impacts for scenarios in which the data quality changes were progressive. Alternatively, we used comparative analysis to determine the better data set for scenarios in which the data quality changes were subtle. While any data quality change will also impact algorithms that use those data, these impacts are outside the scope of this work and should be investigated in future studies.

In this study, we used the SPARC simulator to simulate data from radar systems with different spatial resolution, azimuthal sampling, and/or sensitivity. The different radar characteristics (e.g., varying beamwidth and sidelobe levels) and scan strategies (e.g., varying azimuthal sampling) used in this study were selected to correspond to potential tradeoffs associated with a PAR, which is a promising candidate to replace the WSR-88D. The simulated data were analyzed by one of the authors (Boettcher), who has over 20 years of experience training NWS forecasters as well as 10 years of operational forecasting experience. Her vast experience in interacting with a variety of NWS forecasters (from novices to experts) makes her uniquely qualified as a representative for the broader NWS forecaster population. To support her goal of seeing the data through the eyes of a broad population of NWS forecasters, she had numerous discussions with operational forecasters throughout data collection and analysis. Based on our results, we characterized the relationship between any degradations to the spatial resolution, azimuthal sampling, and/or sensitivity of the radar system and their impacts on forecasters. Our conclusions can be used by decision makers to evaluate future radar designs in the context of tradeoffs between system performance and cost.

The rest of the report is organized as follows. Section 2 describes our study on the impacts of changing the radar's spatial resolution. Section 3 documents our findings on the impacts of changing the radar's azimuthal sampling grid. Section 4 presents our results on the impact of radar sensitivity changes. Finally, Section 5 concludes with a discussion on the significance and limitations of our results, including some potential avenues for future work.

## **2. Impacts of Spatial Resolution**

### **2.1. Introduction**

One cost-driving radar characteristic that has a significant impact on data quality is the spatial resolution of the radar. The spatial resolution (measured in the azimuth, elevation, and range dimensions) is tied to the radar's ability to resolve small-scale weather features and to produce accurate observations in the presence of strong reflectivity gradients. Although both angular (azimuth and elevation) and range resolutions are important for weather radars, this study focuses on angular resolution. The angular resolution is mainly determined by the effective antenna radiation pattern, which includes the intrinsic antenna pattern and any antenna motion and signal processing effects. The effective antenna radiation pattern consists of a main lobe, which determines the transmitted and received power in the direction of interest, and sidelobes, which determine the transmitted and received power from directions away from the direction of interest. Hereafter, the effective antenna radiation pattern is referred to simply as the pattern.

In the context of a planar PAR, we need to study the impact of two types of angular resolution change. The first type of angular resolution change consists of changing the sidelobe level of the antenna pattern. In general, the impact of sidelobe contamination can be reduced if the sidelobes are reduced, but there are important tradeoffs associated with modifying a radar's antenna patterns. For example, pattern sidelobe levels for a phased-array antenna can be reduced via tapering (i.e., an uneven weighting of the signals transmitted and/or received by each antenna element). In this case, if the beamwidth at broadside is to be preserved, the size of the antenna must be increased, which is more costly to build and operate (Doviak and Zrnić 2006). Whereas sidelobe contamination comes from all directions other than the direction of interest, it is typically categorized based on how it manifests in the radar data. If the sidelobe contamination is mainly

due to reflectivity gradients in the azimuthal dimension, it is commonly referred to as azimuthal (or horizontal) sidelobe contamination. Similarly, the term elevation (or vertical) sidelobe contamination is loosely used to describe the situation when contamination is mainly caused by reflectivity gradients *not* in the azimuthal dimension. Operationally, azimuthal sidelobe contamination is more intuitive to identify in the radar data because the dominant reflectivity gradients are on the plane of collection. Thus, its presence can be verified using radar data from a single elevation angle, and the reflectivity gradient that produces it is readily apparent. However, identification of elevation sidelobe contamination likely requires interrogation of multiple radar variables (e.g., reflectivity, Doppler velocity, spectrum width, and correlation coefficient) from multiple elevations. Typically, forecasters analyzing and interpreting radar data in real time find it more challenging to identify elevation sidelobe contamination compared to its azimuthal counterpart. Furthermore, the data quality impacts of elevation sidelobes on forecasters' interpretation of radar data may have more critical implications because this type of contamination is more likely to occur when observing intense convective storms that must be interrogated for a potential severe thunderstorm warning and/or tornado warning. Therefore, our study on the impact of changing sidelobe levels is focused on the operational impacts of elevation sidelobe contamination.

The second type of angular resolution change for a planar PAR is the broadening of its main lobe as the radar scans off broadside. This implies that radar data from a planar PAR will have different angular resolution at different scanning angles. It is possible that the variable resolution could impact the observation of some weather features. For example, changing the angular resolution of the radar can impact the radar-measured rotational velocities of circulations (Brown et al. 2002). Moreover, this beam broadening effect directly impacts the cost of the radar.

Current angular resolution requirement specifies that the beamwidth must be less than or equal to  $1^\circ$  for all scanning angles (NOAA/NWS 2015). To meet this requirement, the size of the phased-array antenna must be chosen such that its beamwidth is  $1^\circ$  when the radar is scanning at  $45^\circ$  away from broadside. It is possible to reduce the system cost if the beamwidth is allowed to exceed  $1^\circ$  for scan angles near  $\pm 45^\circ$  away from broadside as long as the data quality is not significantly impacted. For these reasons, it is important to understand the potential impacts on forecasters from the beam broadening effect. The rest of this section describes the simulation methodology, case selection and data analysis process, and conclusions from our studies on these two types of angular resolution change.

## **2.2. Impact of Changing Antenna Sidelobe Levels**

### **2.2.1. Simulation Methodology**

The SPARC simulator provides a way to simulate weather data as observed by radars with varying azimuthal sidelobe levels (Schvartzman and Curtis 2019). It ingests archived WSR-88D base data (i.e., fields of spectral moments and polarimetric variables) and produces dual-polarization, time-series data corresponding to the same event but observed with differing radar designs. The simulation process consists of four basic steps. First, archived WSR-88D data (fields of the six radar variables) are processed to correct errors (e.g., velocity aliasing) and fill in missing data due to censoring, which ensures that all six radar variables are available at each range location that has significant weather signals. Then, the so-called “conditioned” fields of radar variables are interpolated to a fine azimuth-by-range grid, where the spacing of this grid depends on the scan strategy being simulated. For this study on sidelobe levels, this grid has smaller azimuthal spacing but identical range spacing compared to the WSR-88D data. Each point in the interpolated field is referred to as a “scattering center.” Next, for each scattering center, the SPARC simulator uses the

corresponding radar variables as inputs to a time-series data simulator based on spectral shaping methods (Zrnić 1975 and Galati and Pavan 1995) whose output is a dwell of simulated polarimetric time-series data with the desired characteristics. The time-series data for each scattering center represent the weighted sum of backscattered signals from many hydrometeors, where the weights are the WSR-88D pattern (in the azimuth-elevation plane) and the range weighting function (in the range dimension). Thus, the simulated time-series data for each scattering center already include the effects of the WSR-88D pattern. These effects are intrinsic to the simulated time-series data and must be accounted for when attempting to simulate data that correspond to a different antenna pattern. The last step in the simulation process is weighting and summing the time-series data from a neighborhood of scattering centers to generate the time-series data for a range cell corresponding to the radar and scan strategy being simulated. For example, by choosing the scattering center weights to be a delta function (i.e., a weight of 1 for the scattering center with the same azimuth, elevation, and range as the desired range cell and 0 for all other scattering centers), the SPARC simulator can produce time-series data that correspond to the WSR-88D radar used to collect the input data. However, even in this case, the radar data obtained after processing the time-series data obtained with the SPARC simulator are not an exact match to the input WSR-88D base data due to the randomness introduced by the time-series simulation process. In general, by adjusting the scattering center weights, effects of degraded antenna patterns (both co-polar and cross-polar patterns) and range-weighting functions can be studied. Note that the SPARC simulator cannot simulate any arbitrary pattern that has a narrower beamwidth or lower sidelobe levels than the intrinsic WSR-88D pattern.

To simulate the effects of degraded antenna pattern sidelobes, time-series data for scattering centers from multiple azimuths and elevations must be weighted and summed. The

scattering center weights are the only user-controllable parameters that can be adjusted to construct simulated patterns with varying sidelobe levels, but they alone do not determine the sidelobe levels of the simulated patterns. As mentioned before, the time-series data for each scattering center already include effects from the intrinsic pattern of the WSR-88D. Therefore, after weighting and summing the time-series data from all scattering centers, the simulated pattern is the convolution of the scattering center weights and the WSR-88D pattern. This means that we can simulate full 2D patterns with the same main lobe as that of the WSR-88D pattern and increasingly degraded sidelobes. Note that all sidelobes are increased in our simulations not only those in the principal horizontal and vertical planes.

To simulate realistic patterns where the main lobe width is equal to that of the WSR-88D pattern but the sidelobes are degraded, the scattering center weights must satisfy some restrictions. The first restriction is that the weight for the scattering center in the direction of interest must be 1 while the weights for scattering centers in directions other than the one of interest must be much smaller than 1. This restriction makes sense because the scattering center located in the direction of interest should be most heavily weighted so that the main lobe of the simulated pattern matches the main lobe of the WSR-88D pattern. In addition, scattering centers within a neighborhood ( $2^\circ$  in azimuth and  $1^\circ$  in elevation) of the direction of interest must have zero weights so as to minimize distortions to the main lobe of the simulated pattern. The  $2^\circ$  buffer zone in azimuth is chosen because antenna sidelobe specifications (NOAA/NWS 2015) begin at  $2^\circ$ . The reason for the  $1^\circ$  buffer zone in elevation compared to that of  $2^\circ$  in azimuth is due to the limited sampling in elevation by the WSR-88D;  $1^\circ$  is also the minimum separation that ensures that the main lobes of the intrinsic patterns for adjacent scattering centers do not overlap. The second restriction is that the non-zero scattering center weights outside of the main lobe are monotonically decreasing as

the scattering centers become farther away from the direction of interest. This restriction is reasonable because, for real antenna patterns, sidelobes become smaller as the angular distance increases from the main lobe, and it is rare for sidelobes that are close to each other to have large fluctuations in amplitude. The last restriction is that the non-zero weights are coarsely spaced so that the simulated patterns have realistic sidelobe structures. If the scattering center weights were too finely spaced, the sidelobes of the simulated pattern would be a flat envelope instead of the lobed structure seen in actual antenna patterns. The coarser spacing also prevents artificially inflated sidelobe contamination.

With the stated restrictions in mind, we generated the initial set of scattering center weights based on the Spectrum Efficient National Surveillance Radar (SENSR) Preliminary Performance Requirements (2018) and systematically increased the non-zero weights to simulate full 2D patterns with progressively higher sidelobe levels. We chose the SENSR requirements because they are the latest requirements provided by NOAA and the most realistic requirements that describe the sidelobe levels of the WSR-88D antenna. The angular distance between the direction of a scattering center and the direction of interest was used to determine the weight for that scattering center based on the sidelobe envelope specified in the SENSR Preliminary Performance Requirements. For each weather case, time-series data for scattering centers covering the entire  $360^\circ$  in azimuth and  $0.5^\circ$  to  $8.0^\circ$  in elevation with acquisition parameters (i.e., number of pulses, pulse repetition time, etc.) identical to those used in NEXRAD's Volume Coverage Pattern (VCP) 12 were weighted and summed to simulate data from elevations  $0.5^\circ$  through  $5.1^\circ$ . Data for elevations higher than  $5.1^\circ$  were not simulated because they would be less useful because of large vertical sampling gaps in the input data.

Fig. 2-1 shows a section of the scattering center weights we used to simulate a pattern that is pointing at  $0^\circ$  azimuth and  $2.4^\circ$  elevation. The x-axis and y-axis correspond to azimuth and elevation angles, respectively. The color of each pixel represents the scattering center weight for a scattering center located in that direction (note that the pixels have different sizes in elevation to match the irregular vertical sampling of the input data). The scattering center weights are circularly symmetric and depend on the angular distance between the direction of the scattering centers and the direction of interest. As the angular distance between the direction of a scattering center and the direction of interest increases, the weight linearly decreases from  $-15$  dB at  $1^\circ$  separation to  $-50$  dB for separation  $\geq 10^\circ$ . It is also clear that these scattering-center weights satisfy the restrictions discussed above. That is, the scattering center in the direction of interest receives unit weight while neighboring scattering centers receive zero weights; the non-zero scattering center weights outside of the main lobe are monotonically decreasing; and the azimuthal gap between non-zero weights outside of the main lobe is  $2^\circ$ . Note that scattering centers located off the principal horizontal and vertical planes have non-zero weight, meaning effects of sidelobes in all directions are simulated.

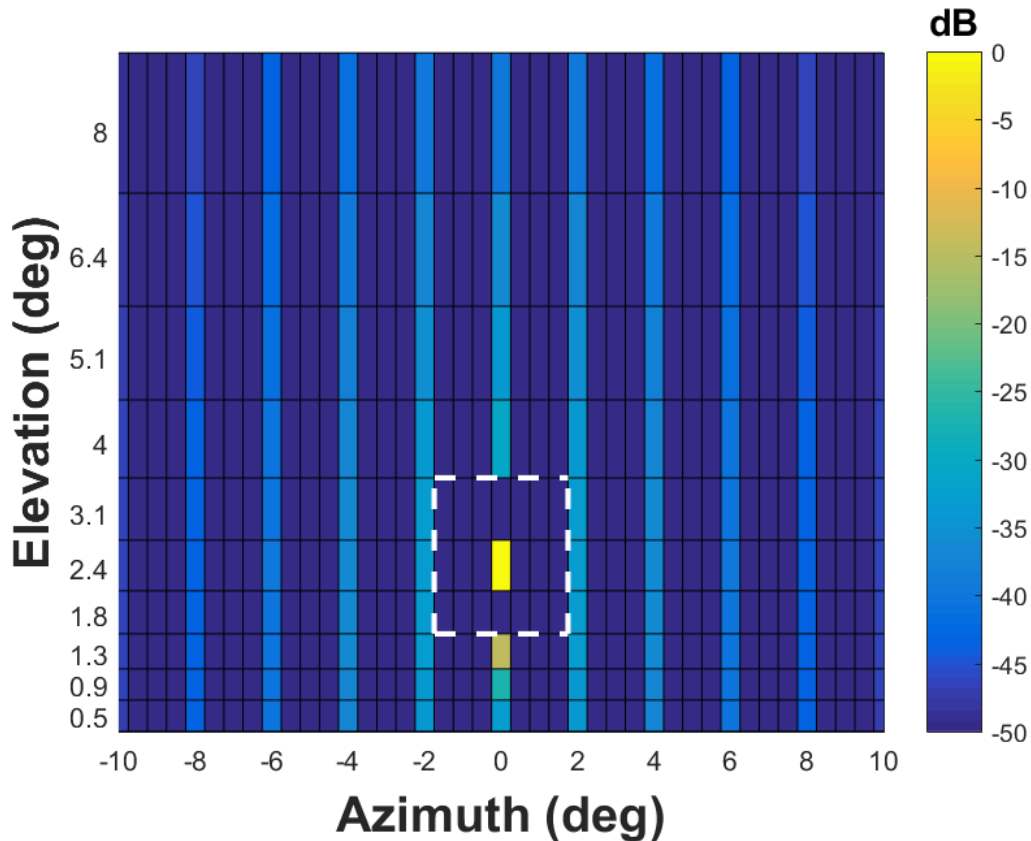


Fig. 2-1. Scattering center weights used to simulate a pattern that is pointing at  $0^\circ$  azimuth and  $2.4^\circ$  elevation. The axes correspond to azimuth and elevation angles, and the color indicates the magnitude of the weight for each scattering center in logarithmic units. The scattering center in the direction of interest received unit weight. The scattering centers within  $2^\circ$  azimuth and  $1^\circ$  elevation of the direction of interest (inside the white dashed-line box) received zero weight (shown as  $-50$  dB here). The weights for other scattering centers are based on their angular distance from the direction of interest.

Fig. 2-2 shows an illustration of the process we used to modify sidelobe levels in our simulations. In this illustration, we utilized a measured KOUN pattern between  $\pm 13^\circ$  (blue line) to represent a cut of the intrinsic WSR-88D pattern for each scattering center. Note that the available measurement limited the KOUN pattern to be within  $\pm 13^\circ$ , but the intrinsic WSR-88D patterns in our simulations are full 2D patterns. The WSR-88D specifications (solid black line) and the SENSAR sidelobe requirements (dashed black line) are shown as references. A cut of a simulated pattern (red curve) and the associated scattering center weights in the same dimension (green dots)

are shown. It is clear that the sidelobe levels of the simulated pattern are mainly determined by the scattering center weights for the directions where the scattering center weights are much larger than the sidelobe levels of the intrinsic WSR-88D pattern (e.g., at  $\pm 2^\circ$ ,  $\pm 4^\circ$ , and  $\pm 6^\circ$ ). Therefore, by uniformly increasing the scattering center weights, we can simulate full 2D antenna patterns with higher sidelobes.

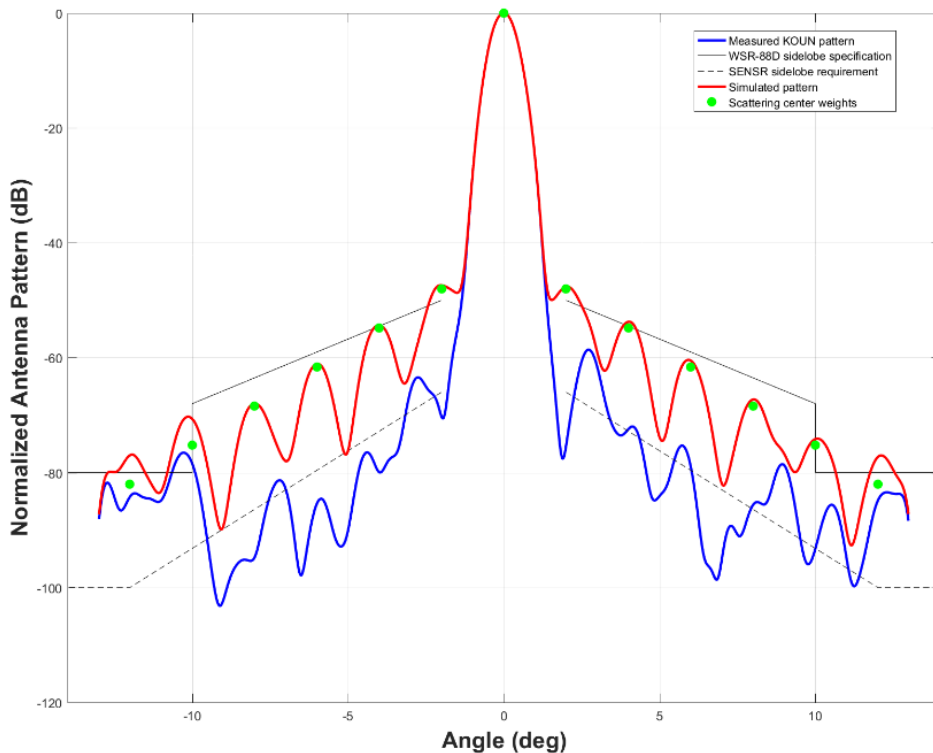


Fig. 2-2. 1-dimensional cut of the normalized 2-way antenna radiation pattern measured for KOUN (blue curve) and a simulated pattern (red curve) with its associated scattering center weights (green dots). The WSR-88D specifications (solid black line) and the SENSR sidelobe requirements (dashed black line) are shown as references.

The straightforward way to quantify sidelobe levels is to measure them from the simulated patterns. Since the simulated pattern is the convolution of the scattering center weights with the intrinsic WSR-88D pattern, we need precise knowledge of the WSR-88D pattern in addition to the known weights to be able to calculate the sidelobe levels of the simulated patterns. Unfortunately,

only certain cuts of the WSR-88D pattern are available (Doviak and Zrnić 1998, 2006), so the simulated 2D patterns cannot be obtained precisely. An alternative approach to quantify sidelobes is through measuring the relative sidelobe degradations compared to the WSR-88D pattern, which eliminates the need to build representative models for WSR-88D patterns at different sites. This can be done without precise knowledge of the intrinsic WSR-88D pattern by assuming that its sidelobe levels are much lower than its main lobe and that the scattering center weights satisfy the restrictions stated in the previous subsection. Under these conditions, the contribution to the sidelobes of the simulated pattern from each scattering center is mainly determined by the main lobe of the intrinsic WSR-88D pattern. One measure to quantify sidelobe performance for weather radars is the integrated sidelobe level (ISL), which is the ratio of the power received through the sidelobes to the power received through the main lobe. Since the main lobe of the simulated pattern is the same as that of the WSR-88D pattern by design, the difference (in linear units) between the ISL of each simulated pattern and the WSR-88D pattern can be estimated as the sum of the weights that were applied to scattering centers outside of the direction of interest.

For this study, we used the difference in ISL (referred to as “delta” ISL and denoted by  $\Delta$ ISL) to quantify the relative sidelobe degradation of each simulated pattern compared to the WSR-88D pattern. Since the ISL of the simulated pattern is the sum of its  $\Delta$ ISL and the ISL of the intrinsic WSR-88D pattern, the  $\Delta$ ISL of the simulated patterns must be comparable to or larger than the ISL of the intrinsic WSR-88D pattern to prevent the effects of the intrinsic WSR-88D pattern from dominating the quality of the simulated data. In our simulations, we chose the scattering center weights to be systematically larger than the requirement envelope (see Fig. 2-2). This assumes that the sidelobes of the intrinsic pattern are less than or equal to the SENSr requirement envelope, which is known to be true based on measurements (Doviak 2017). Selecting

the scattering center weights in this manner guarantees that the resulting  $\Delta$ ISL is greater than or equal to the intrinsic ISL (i.e., the simulated patterns have sidelobes that are at least 3-dB larger than those of the intrinsic pattern). From the example shown in Fig. 2-2, it is clear that by uniformly increasing the scattering center weights, the  $\Delta$ ISL of the simulated patterns will match or surpass the ISL of the intrinsic pattern. For each weather case, 10 different patterns with varying  $\Delta$ ISL were simulated by uniformly increasing the scattering center weights in directions away from the direction of interest. The simulated patterns and their associated  $\Delta$ ISL (in both linear and dB units) are listed in Table 2-1 in order of increasing sidelobe degradation.

Table 2-1. Simulated patterns and their associated  $\Delta$ ISL in linear and dB units. The intrinsic WSR-88D pattern is used as a reference to calculate  $\Delta$ ISL and has a  $\Delta$ ISL of 0 (in linear units).

Simulated Pattern	$\Delta$ ISL	$\Delta$ ISL (dB)
Pattern A	0.0161	-17.9
Pattern B	0.0322	-14.9
Pattern C	0.0483	-13.2
Pattern D	0.0643	-11.9
Pattern E	0.0804	-10.9
Pattern F	0.0965	-10.2
Pattern G	0.1126	-9.5
Pattern H	0.1287	-8.9
Pattern I	0.1448	-8.4
Pattern J	0.1608	-7.9

To demonstrate the fidelity of our simulations, we compared simulated data to WSR-88D data, and we found two types of compromised data due to elevation sidelobe contamination. Hereafter, compromised data due to elevation sidelobe contamination will be referred to simply as compromised data. The first type of compromised data that is seen in the WSR-88D is questionable low-level circulations. For this type of compromised data, the sidelobe contamination dominates the received power from the main lobe, resulting in Doppler velocity estimates that appear to be valid. Since this signature may or may not be a valid circulation, forecasters' cognitive resources are diverted toward diagnosing the validity of this signature (i.e., they must interrogate spectrum

width and correlation coefficient). To demonstrate this type of compromised data, Figs. 2-3a and 2-3b show WSR-88D data collected by the KLRX radar at 04:45Z 22 July 2014 at 0.5° elevation (left column) and simulated data for this case without (middle column) and with moderate sidelobe degradation (right column). Note that this comparison of the same data with and without sidelobe contamination is only possible via simulations. Fig. 2-3a displays fields of reflectivity (Z, top row), storm-relative velocity (SRM, middle row) and spectrum width (W, bottom row), where storm-relative velocity is simply Doppler velocity with storm motion subtracted. Fig. 2-3b displays differential reflectivity (ZDR, top row), specific differential phase (KDP), and correlation coefficient (CC, bottom row). The color bars we used to display our data are enlarged in Fig. 2-4 for easier reference, and the same color bars are used for the remainder of this report. Comparing the left columns to the middle columns of Figs 2-3a and 2-3b shows that the SPARC simulator can produce data that are well matched to WSR-88D data for all radar variables. The increase in the number of 0 m s<sup>-1</sup> spectrum width estimates is due to our digital signal processor using a different spectrum width estimator compared to the digital signal processor of the WSR-88D. Comparing the middle columns to the right columns of Figs. 2-3a and 2-3b clearly shows the impact of increasing sidelobe levels. This is especially apparent in storm-relative velocity where higher sidelobe levels result in an expanded footprint of inbound velocities (in the circled region) that corresponds to low reflectivity, large spectrum width, and reduced correlation coefficient. To verify that our simulations of this type of compromised data are realistic, we compared our simulated data to WSR-88D data from other sites that contained similar questionable circulations. Fig. 2-5 shows the fields of reflectivity (top left), storm-relative velocity (top right), spectrum width (bottom left), and correlation coefficient (bottom right) for a storm observed by the KDFX radar at 23:02Z 15 May 2014 at 0.5° elevations. In the real data, we see an expanded footprint of

inbound velocities (in the circled region) that corresponds to low reflectivity, large spectrum width, and reduced correlation coefficient. These features match well with our simulated data for this type of compromised data (i.e., compare the corresponding images in the right column of Figs. 2-3a and 2-3b to Fig. 2-5). Note that in Figs. 2-3a and 2-3b and subsequent figures, radar features are circled in reflectivity and storm-relative velocity, while dashed circles are used for other radar variables. This is to reinforce the significantly greater salience of reflectivity and storm-relative velocity for observing this feature during real-time warning operations. Also note that, for storm interpretation purposes, the collocation of important features, especially a possible circulation in Z and SRM (as well as any other radar variables), must be assessed.

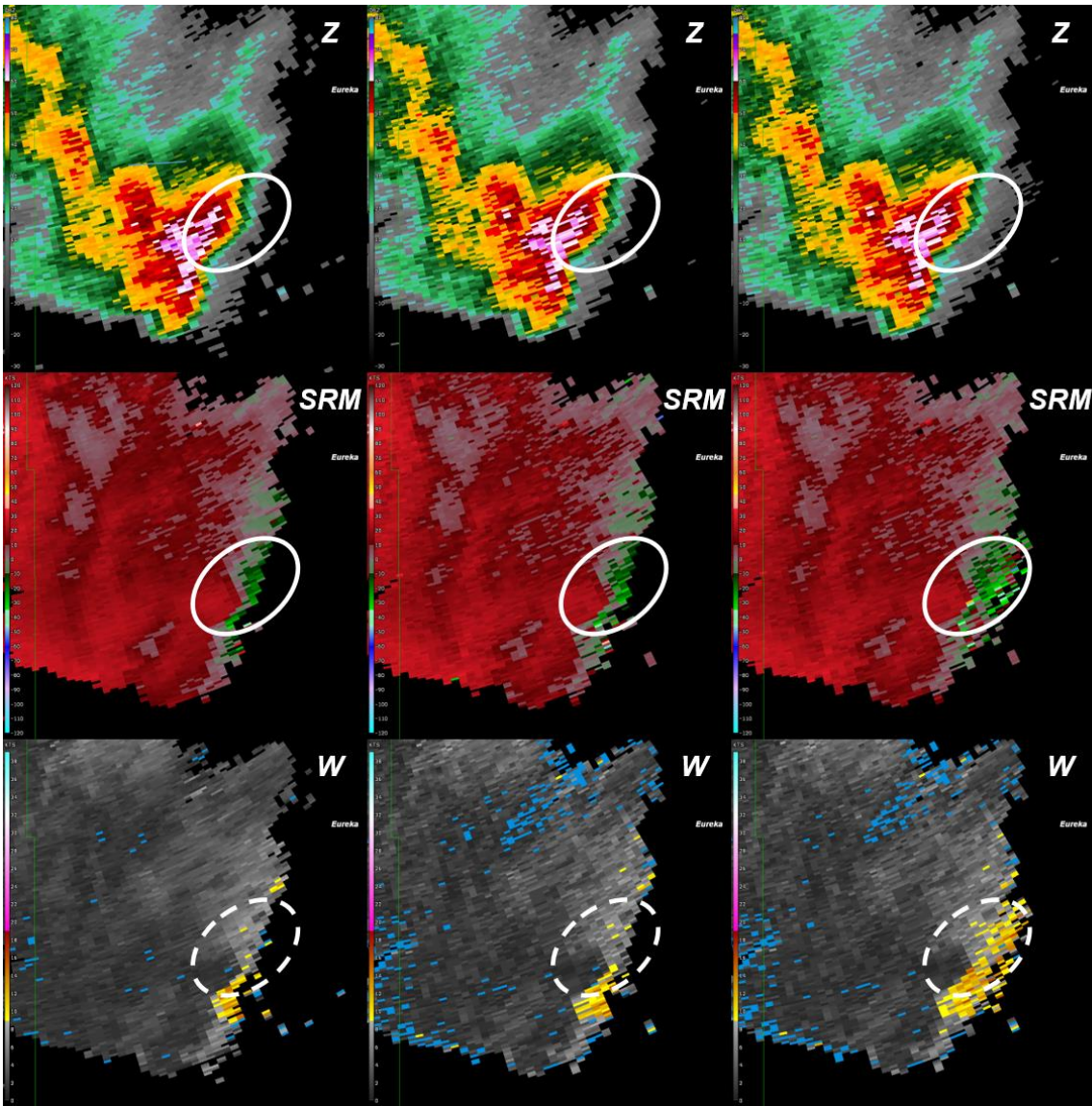


Fig. 2-3a. Reflectivity (top row), storm-relative velocity (middle row), and spectrum width (bottom row) at  $0.5^\circ$  elevation for a storm observed by the KLRX radar at 04:45Z 22 July 2014 (left column), simulated data for this case without (middle column) and with moderate sidelobe degradation (right column).

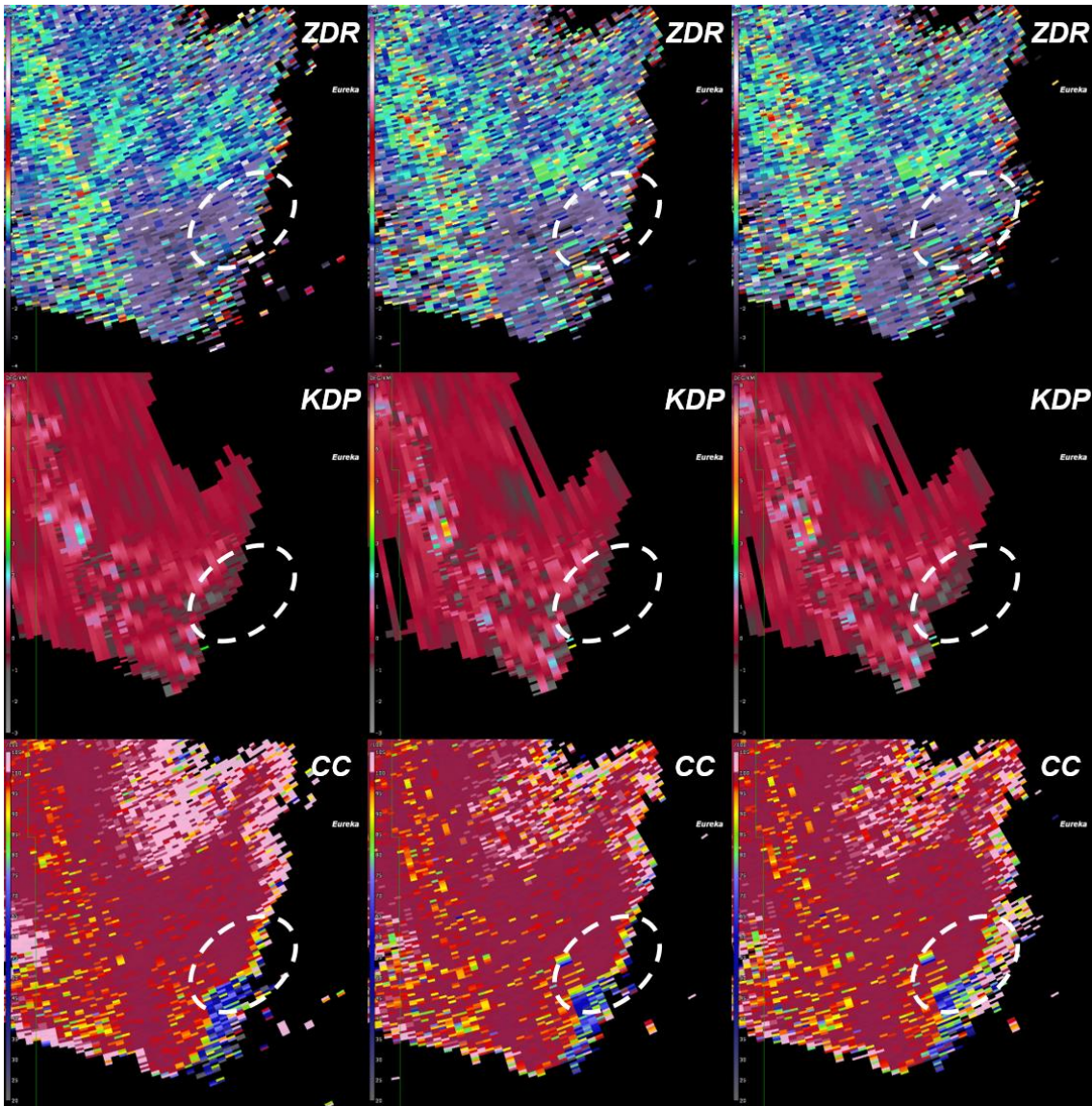


Fig. 2-3b. Same as 3a but showing differential reflectivity (top row), specific differential phase (middle row), and correlation coefficient (bottom row).

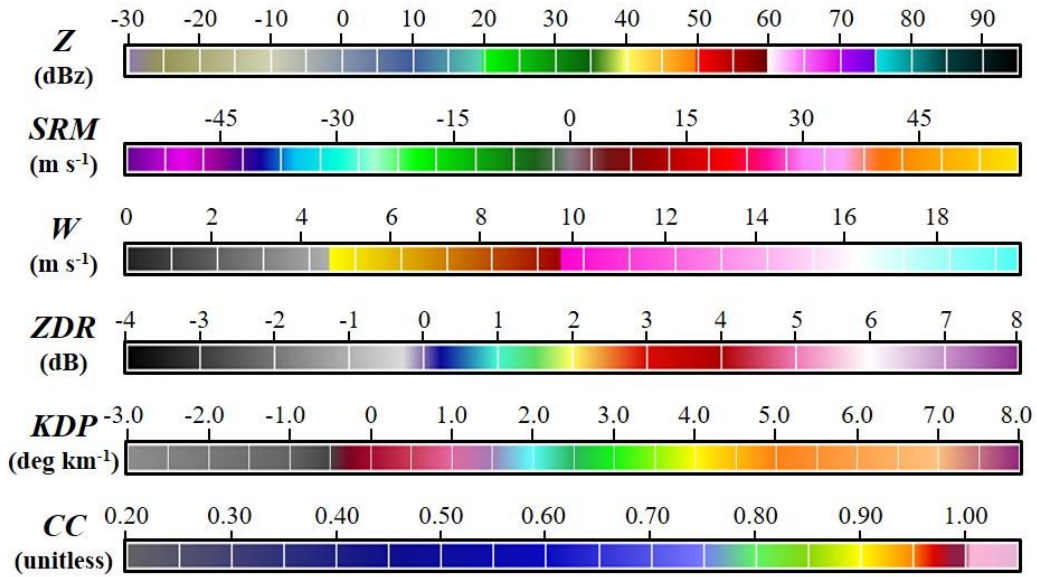


Fig. 2-4. Enlarged color bars used to display reflectivity (top row), storm-relative velocity (second row), spectrum width (third row), differential reflectivity (fourth row), specific differential phase (fifth row) and correlation coefficient (bottom row).

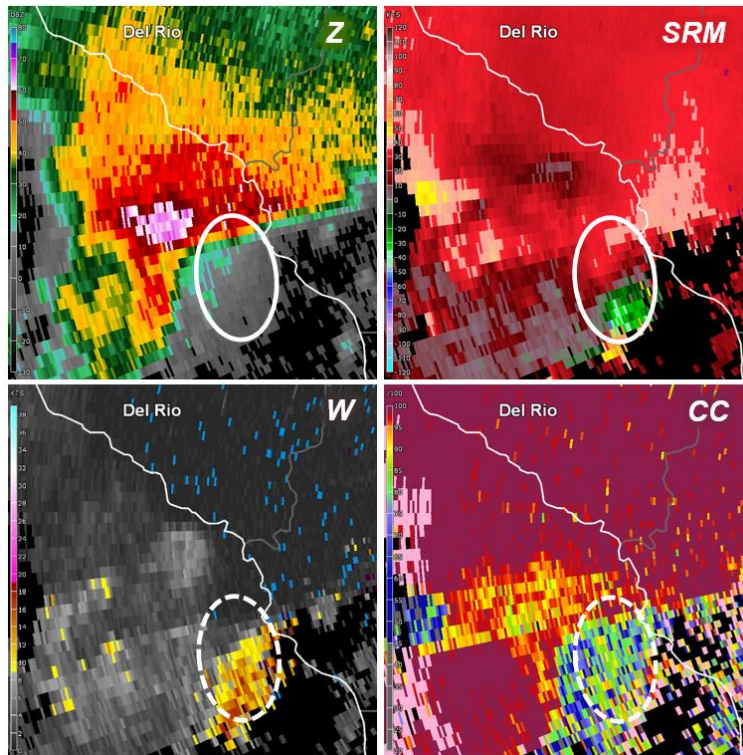


Fig. 2-5. Reflectivity (top left), storm-relative velocity (top right), spectrum width (bottom left) and correlation coefficient (bottom right) at 0.5° elevation for a storm observed by the KDFX radar at 23:02Z 15 May 2014.

The second type of compromised data consists of noisy velocity data (both base velocities and storm-relative velocities) in the low-level storm inflow region. For this type of compromised data, the sidelobe contamination is more comparable to the received power from the main lobe, resulting in less reliable velocity estimates that appear to be invalid. Based on personal communications with multiple NWS operational forecasters, our understanding is that this type of compromised data is not typically being identified as caused by sidelobe contamination by most NWS forecasters. This makes sense as a questionable circulation is visually compelling while noisy velocity data in weak signal areas are visually filtered as non-reliable. Figs. 2-6a and 2-6b show a comparison of WSR-88D data collected by the KGLD radar at 00:39Z 23 May 2015 at 0.5° elevation (left column) and simulated data for this case without (middle column) and with moderate sidelobe degradation (right column) to demonstrate this type of compromised data. An example of this type of contamination in real data is shown in Fig. 2-7 from a storm observed by the KMRX radar at 20:50Z 7 July 2014 at 0.5° elevation. The circled storm inflow region in both real and simulated data contains numerous gates with noisy storm-relative velocity, large spectrum width, and reduced correlation coefficient (i.e., compare the corresponding images in the right columns of Figs. 2-6a and 2-6b to Fig. 2-7). The examples Figs. 2-3 and 2-6 demonstrate that our simulator can reproduce the same types of compromised data as seen in WSR-88D data.

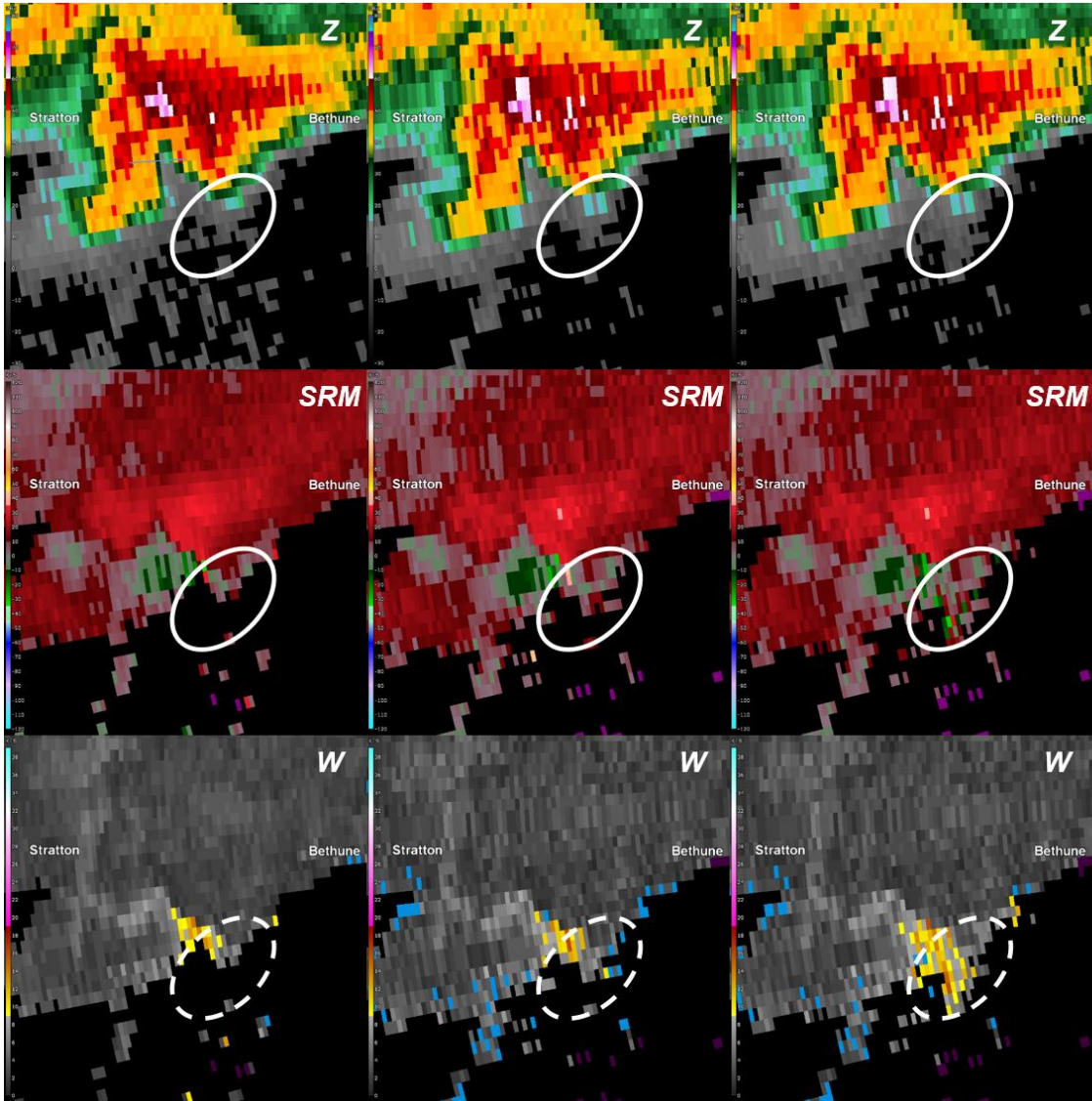


Fig. 2-6a. Same as Fig. 3a except for a storm observed by the KGLD radar at 00:39Z 23 May 2015.

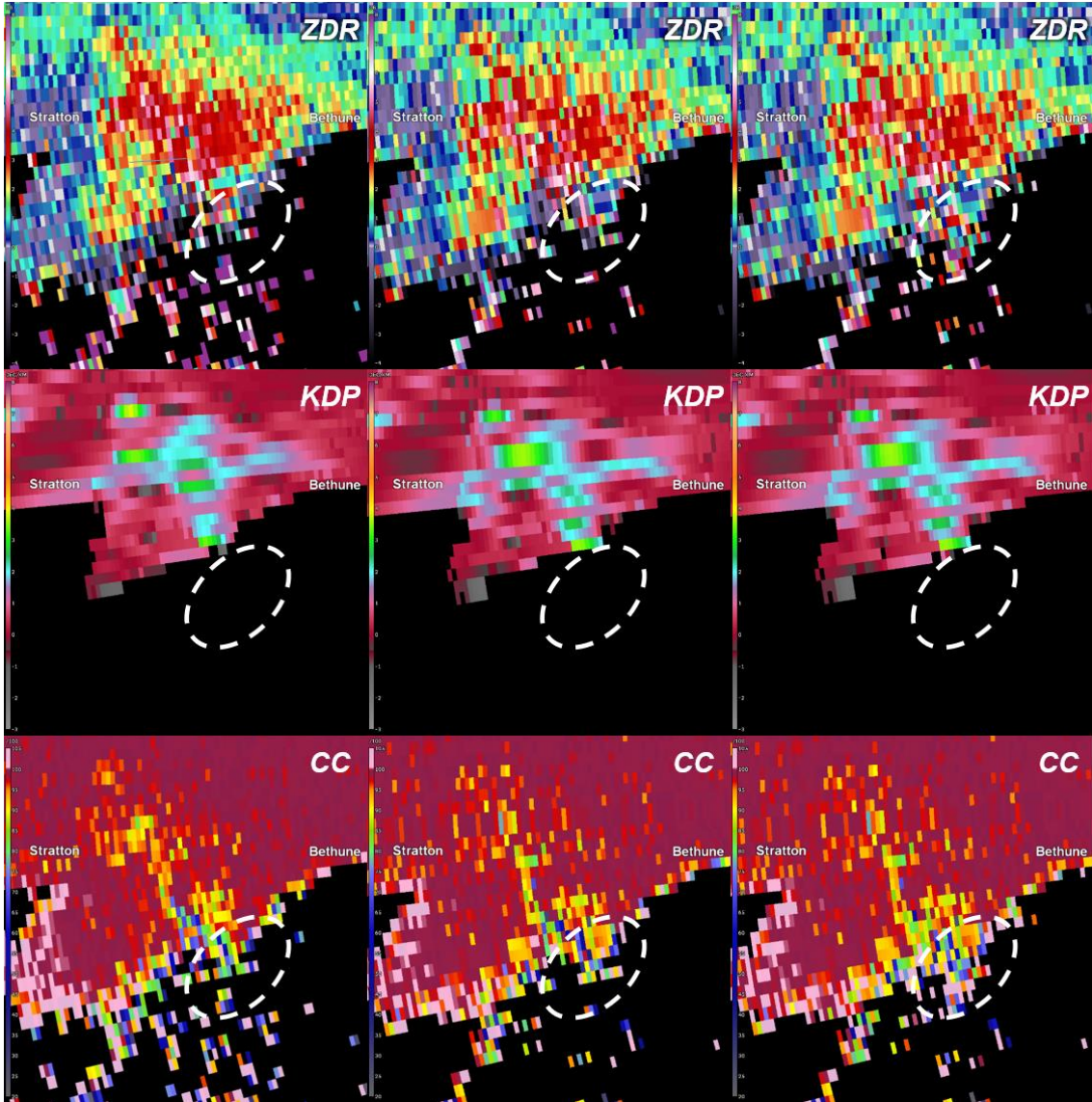


Fig. 2-6b. Same as Fig. 3b except for a storm observed by the KGLD radar at 00:39Z 23 May 2015.

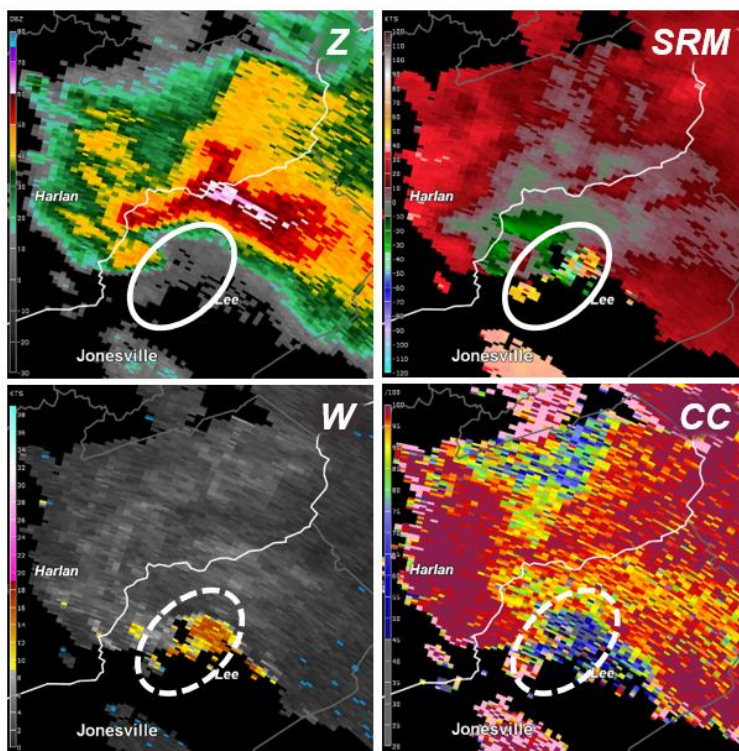


Fig. 2-7. Same as Fig. 5 except for a storm observed by the KMRX radar at 20:05Z 7 July 2014.

### 2.2.2. Case Selection and Data Analysis Process

To improve our understanding of the relationship between relative sidelobe degradation and impact on NWS forecasters’ interpretation of radar data, we selected cases that are most likely to show increased data quality degradation due to elevation sidelobe contamination as sidelobe levels are increased. The storm type that is most prone to produce elevation sidelobe contamination is a supercell with large hail, which is also one of the most difficult storm types to analyze during NWS warning operations. We developed a scoring system based on the extent of data quality “distractions” to quantify the impact on forecasters. The case selection process and the scoring system are discussed next, and examples are shown to demonstrate the analysis process used to arrive at the score for each simulated pattern and to illustrate the data quality differences among the scoring levels.

The storm type used for this study typically has high reflectivity aloft that “overhangs” the low-level clear-air inflow region. Supercells are one of many types of hazardous convection, and convection is one of many threats (e.g., flooding, winter, or fire) addressed by the NWS mission of protecting lives and property. Supercells often warrant a severe thunderstorm warning due to large hail (equal to or in excess of 1” or 2.54 cm) or strong straight-line winds (equal to or in excess of 58 mph or 26 m s<sup>-1</sup>) [NOAA/NWS 2018]. Supercells are also potentially tornadic and require close monitoring of the storm’s structure and its local environment because a tornado warning may also be warranted. Since these warnings are so critical to fulfilling the NWS mission, it is important to understand the impact of data quality degradation on forecasters’ interpretation of radar data that could affect these warning decisions.

For our study, we wanted the different cases to have similar impacts on forecasters given comparable elevation sidelobe degradations. Therefore, it was important for the cases we selected to be consistent in the sense that they had similar storm morphology that could cause increasingly compromised data for antenna patterns with higher sidelobe levels. We used two methods to identify suitable cases. First, we found two examples of supercell storms that resulted in significantly compromised WSR-88D data, which presented as a questionable low-level circulation. For these storms, we chose a scan time without the questionable low-level circulation that is close to the time in which a questionable low-level circulation was observed in the WSR-88D data. This method to select cases is reasonable because we can expect that any degradation to the pattern sidelobes should result in comparable data quality degradation for these storms. In addition to the cases selected using the first method, we also identified multiple supercell storms with the characteristic significant reflectivity overhang structure that did not cause a questionable low-level circulation in the WSR-88D data. These marginal cases allowed us to better understand

the different levels of impact on forecasters as different patterns were simulated. That is, they are the most likely candidates to display the full transition from no impact to significant impact as the sidelobe levels are increased. In total, we selected 13 cases for this study; these are listed in Table 2-2.

Table 2-2. Selected weather cases to evaluate impacts of degraded sidelobes on forecasters’ data interpretation process.

Case Number	Date and Radar
1	20:55Z 27 July 2014, KMRX
2	03:47Z 14 June 2014, KUDX
3	01:20Z 18 September 2015, KTWX
4	19:05Z 4 August 2015, KBOX
5	00:11Z 21 June 2015, KUDX
6	22:03Z 10 September 2015, KUEX
7	23:43Z 26 April 2015, KFWS
8	23:14Z 10 September 2015, KTWX
9	00:50Z 2 April 2014, KDYX
10	22:58Z 25 May 2014, KDFX
11	04:45Z 22 July 2014, KLRX
12	00:39Z 23 May 2015, KGLD
13	21:12Z 1 June 2015, KAFX

The simulated data were analyzed to identify potential “distractions” to forecasters’ interpretation process caused by degraded data quality. Here, a distraction is defined as a misrepresentation of an important weather feature or a lowering of confidence in the validity of the data. Distractions could result in forecasters expending additional attention and working memory toward confirming the validity of the signature, interrogating other radar variables, waiting for additional scans, or issuing a false-alarm warning. These actions are undesirable due to the time constraint of NWS warning operations. For each case, simulated data for elevations 0.5° through 5.1° were analyzed. We mirrored the vertical analysis process for storm interrogation commonly used by NWS forecasters in real-time operations to assess these low-to-middle elevations for distractions caused by compromised data. Factors such as storm history and

environment were not part of the analysis, as the scans were analyzed for the presence or absence of distractions caused by compromised data. The radar variables used for the analysis are reflectivity, storm-relative velocity, spectrum width, and correlation coefficient. For the critical, specific domain of supercell interrogation, diagnosing elevation sidelobe contamination is best done using correlation coefficient among the polarimetric variables (i.e., differential reflectivity and differential phase have negligible benefit). As explained in Section 1, Boettcher analyzed our simulated data for this study while representing the broader NWS forecaster population. In addition to gaining a better knowledge of the varying understanding of elevation sidelobe contamination among forecasters, she also learned there is wide variation in real-time methodology when analyzing this particularly difficult type of compromised data (e.g., differing usage of spectrum width and/or correlation coefficient for data quality analysis). For each case, the data analysis was performed without her knowledge of the underlying parameters of the simulated pattern. This was important to prevent expectation biases in her analysis process. Although any individual forecaster may arrive at somewhat different analysis results, we feel that our results characterize the impacts of compromised data from the perspective of the NWS forecaster population as a group, which is ideally represented by Boettcher.

To quantify the impact on forecasters' interpretation of radar data, a five-level scoring scale was developed as shown in Table 2-3. The scale was based on how much distraction the compromised data would cause. A score of 1 indicates fully acceptable data quality with no distractions; a score of 2 indicates acceptable data quality that contains minimal distractions; a score of 3 indicates ambiguous data quality where the impact of the distraction would vary significantly from forecaster to forecaster; a score of 4 indicates unacceptable data quality where the distractions would affect nearly all forecasters; and a score of 5 indicates completely

unacceptable data quality where distractions would significantly impact data interpretation. We decided on using five levels for the scoring system because they can better capture the relationship between elevation sidelobe degradation and data quality impact on forecasters compared to a binary acceptable/unacceptable categorization. At the same time, the five levels are distinct enough that the observed data quality differences can be meaningfully categorized. Examples of simulated data with different scores are shown next.

Table 2-3. Scoring system used to codify impacts on forecasters interpretation of radar data.

Score	Explanation
5	Completely Unacceptable
4	Unacceptable
3	Ambiguous
2	Acceptable
1	Fully Acceptable

We present Case 11 as an example to demonstrate the analysis process used to arrive at the score for each simulated pattern and to illustrate the data quality differences among the scoring levels. Fig. 2-8 shows the reflectivity (top left), storm-relative velocity (top right), spectrum width (bottom left), and correlation coefficient (bottom right) from the KLRX radar at 0.5° elevation at 04:45Z on 22 July 2014. This storm had elevation sidelobe contamination that resulted in a questionable circulation in scans between 04:13Z and 04:40Z, similar to those shown in both the simulated data (right columns of Fig. 2-3) and WSR-88D data (Fig. 2-5). Fig. 2-9 shows reflectivity and storm-relative velocity from simulated data with ascending scores from the top row (score of 1) to the bottom row (score of 5). The simulated patterns for each row from top to

bottom correspond to patterns A, B, D, G, and J. The following analysis description was based on elevations  $0.5^\circ$  through  $5.1^\circ$ , with  $0.5^\circ$  shown in Fig 2-9 for brevity and because the greatest impacts occur on the lowest elevations. Comparing the top row of Fig. 2-9 to Fig. 2-8, we see trivial differences along the eastern storm edge as a result of the simulation process. There are no distractions to forecasters' interpretation of radar data. Therefore, for this case, pattern-A data received a score of 1. In the second row of Fig. 2-9, we can see a slightly increased footprint of the inbound velocity in the circled area compared to the top row (and Fig. 2-8) as a result of increased sidelobe levels. However, this slight increase in footprint is not a major distraction to forecasters' interpretation of radar data; therefore, pattern-B data received a score of 2 in this case. In the third row of Fig. 2-9, we see more inbound velocities in the circled area mixed with some outbound velocities. Reactions to these noisy velocities can vary significantly among forecasters. Based on Boettcher's experience, the number of forecasters that would be distracted by the data presentation is roughly even with the number of forecasters that would not be significantly affected. Therefore, pattern-D data received a score of 3 in this case. The fourth row of Fig. 2-9 shows a further expansion of the footprint of mostly inbound velocity, which is a significant data quality distraction to almost all forecasters. This resulted in pattern-G data receiving a score of 4. In the last row in Fig. 2-9, the footprint of inbound velocity grows further, and there is also an expansion of precipitable values in the inflow region due to sidelobe contamination in the reflectivity image. This extensively compromised data caused the pattern-J data to receive a score of 5 in this case.

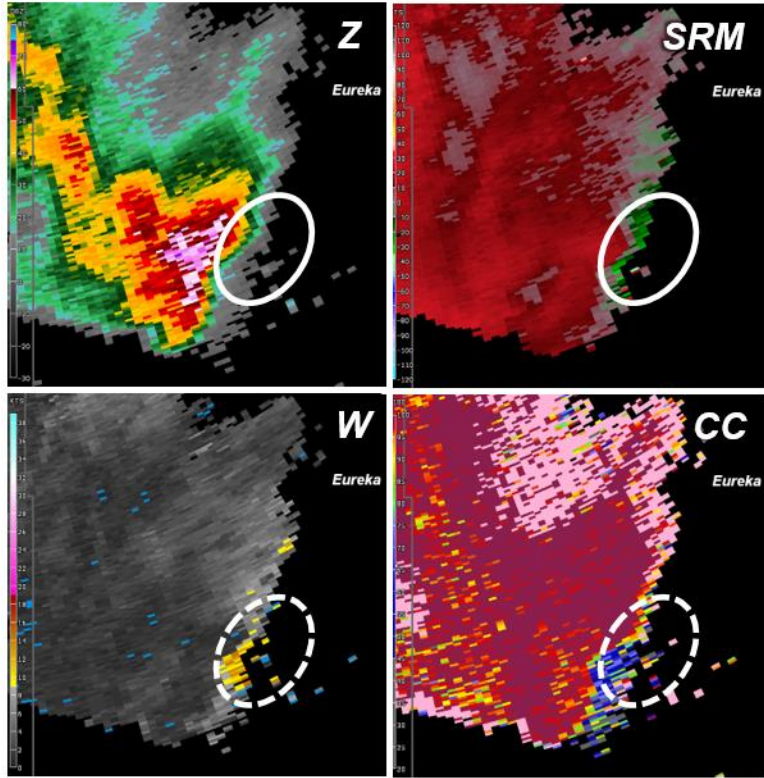


Fig. 2-8. Same as Fig. 5 except for a storm observed by the KLRX radar at 04:45Z 22 July 2014.

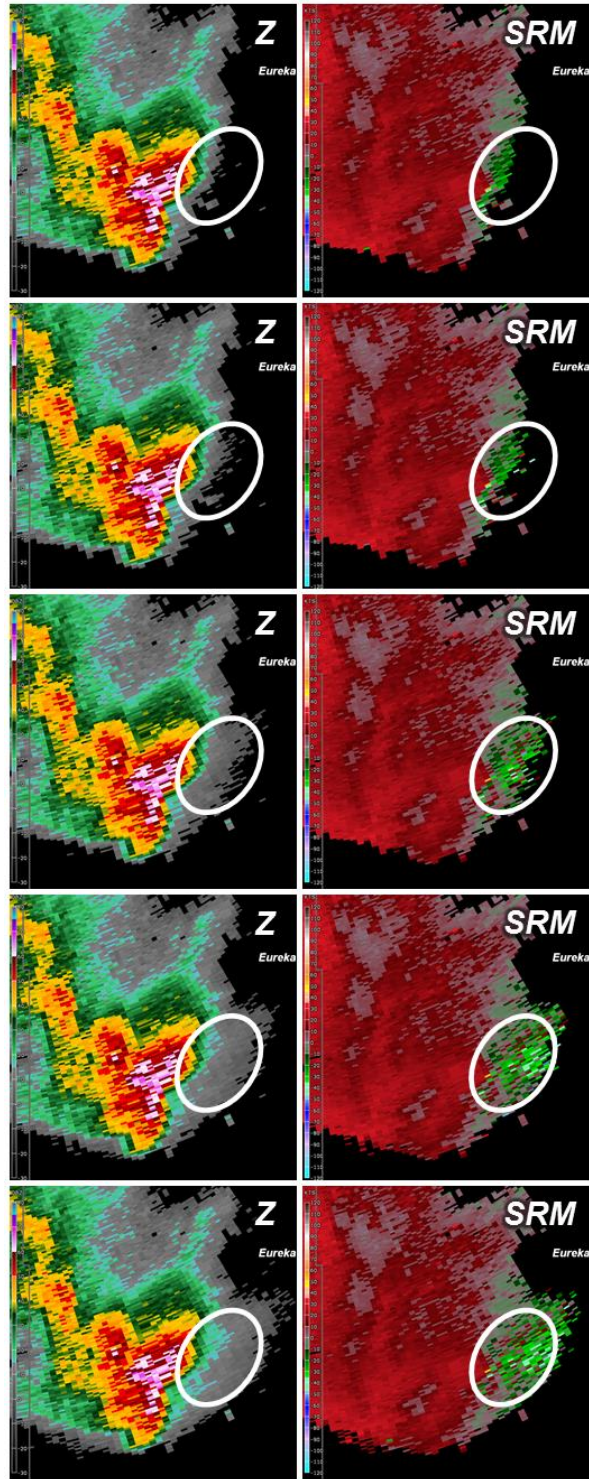


Fig. 2-9. Reflectivity (left column) and storm-relative velocity (right column) of Case 11 at  $0.5^\circ$  elevation with ascending scores from top (score of 1) to bottom (score of 5). The simulated patterns corresponding to the five rows from top to bottom are Patterns A, B, D, G, and J. The data quality impacts caused by increasing sidelobe levels can be clearly seen in the storm-relative velocity field in the circled area.

### 2.2.3. Simulation Results

To better understand the relationship between relative sidelobe degradation and impact on forecasters' interpretation of radar data, we fit a sigmoidal curve to our score data for each of the 13 cases. The sigmoidal curve was chosen because the function asymptotically approaches the maximum (minimum) score as the sidelobe degradation is increased (decreased) to infinity (zero). This captures the fact that once the score reaches 5 (1), continuing to increase (decrease) sidelobe levels will not change the score. The fitted curve has the form

$$f(\Delta\text{ISL}) = 1 + \frac{4}{1 + e^{-k(\Delta\text{ISL} - x_o)}}, \quad (2.1)$$

where  $\Delta\text{ISL}$  is in linear units (middle column of Table 2-1), and  $k$  and  $x_o$  are unknown parameters (to be determined) that control the steepness and the position of the center of the curve. We used a grid search that minimized the mean squared error between the fitted curve and our scoring data to determine the value of  $k$  and  $x_o$  for each case. The top panel of Fig. 2-10 shows an example of a fitted curve for Case 11 (blue line) for which  $k$  is 10 and  $x_o$  is 0.069. The values of  $x_o$  for the fitted curves vary from case to case because, despite our attempts to select comparable cases, the cases we selected have a different amount of tolerance to sidelobe degradation before the impact on forecasters' interpretation of radar data reaches the marginal level. However, this does not prevent us from attempting to quantify the relationship between sidelobe degradation and impact on forecasters' interpretation process since that relationship corresponds to the shape and steepness of the curve. From the 13 cases we simulated, 12 cases have  $k$  between 7 and 37 with an average of 20 and a standard deviation of 8.5. For the outlier (Case 9), the value of  $k$  is 87. The reason for this outlier is that its score was dominated by artifacts caused by azimuthal sidelobe contamination. Many of the cases presented some data quality degradation caused by azimuthal sidelobe contamination as well as elevation sidelobe contamination, but Case 9 was significantly affected

due to much stronger azimuthal reflectivity gradients compared to the others. The bottom panel of Fig. 2-10 shows the fitted curves (gray lines) for the non-outlier cases and a curve (black line) with  $k$  and  $x_o$  equal to the average of the non-outlier cases.

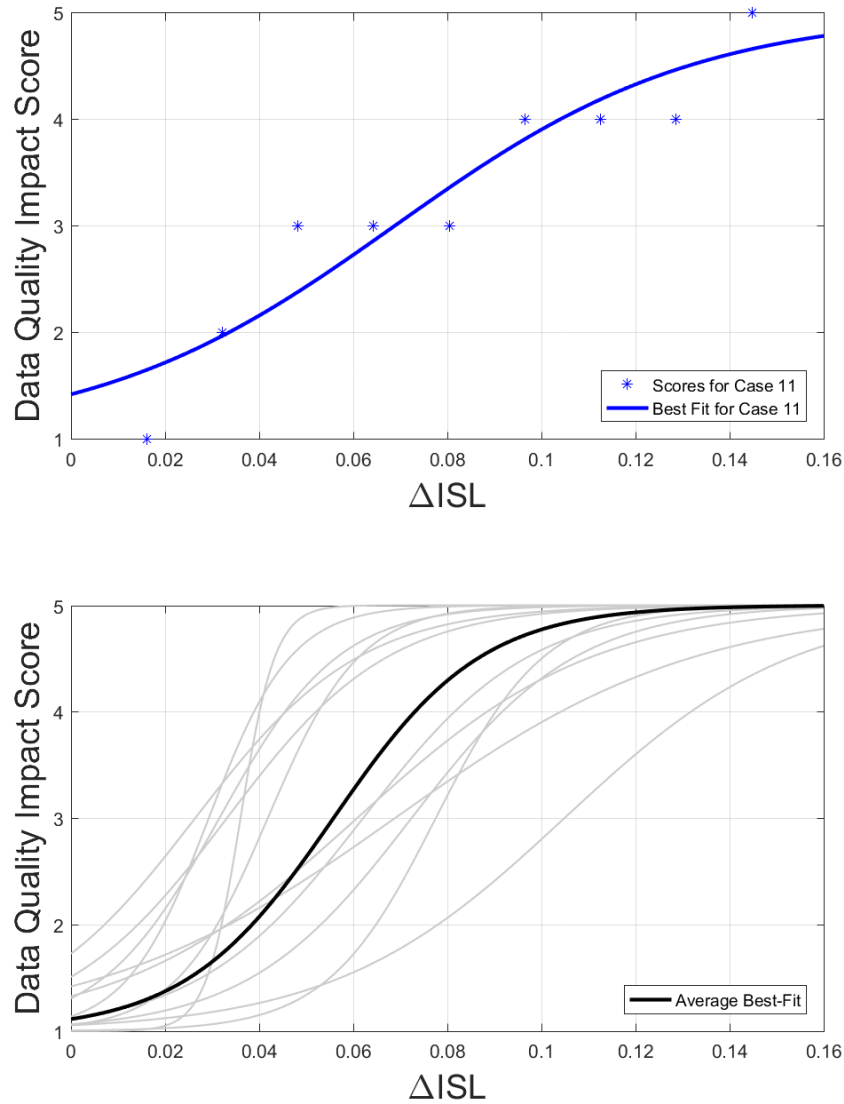


Fig. 2-10. Scores for the simulated patterns (blue stars) and the fitted curve for Case 7 (blue line) are shown in the top panel. The fitted curves for all 12 non-outlier cases and the average best-fit curve (black line) are shown in the bottom panel. The x-axes are  $\Delta ISL$  in linear units (middle column of Table 2-1). Note that the curve fitting minimizes the mean squared error and capture the trend of the scores. The average best-fit curve uses parameters that are the average of all the non-outlier cases.

Based on the average steepness of the remaining 12 cases, we developed the model shown in Fig. 2-11 for the relationship between relative sidelobe degradation with respect to the WSR-88D pattern and impact on forecasters' interpretation of radar data. This model will be referred to as the "impact model" for simplicity. Based on the scoring system defined previously, there are three regions of impact: acceptable, marginal (shaded in yellow), and unacceptable (shaded in red). These regions are separated by the horizontal dashed lines. Within the acceptable region, the model curve falls into two separate subregions: low sensitivity (shaded in green) and high sensitivity (shaded in cyan), separated by the first vertical dashed line. Sensitivity here means how much the impact score changes when the relative sidelobe degradation changes (i.e., the slope of the curve). Lower sensitivity is better than higher sensitivity because the impact on forecasters would be less for a similar amount of sidelobe degradation. The value that separates the two regions is determined by the slope of the curve when it first reaches 25% of the maximum slope. Note that, due to our case selection process, the average best-fit curve (black line) has a score of 1.1 for patterns with zero sidelobe degradation (i.e., the WSR-88D pattern) in Fig. 2-10, which places the WSR-88D in the acceptable with low sensitivity region of the model.

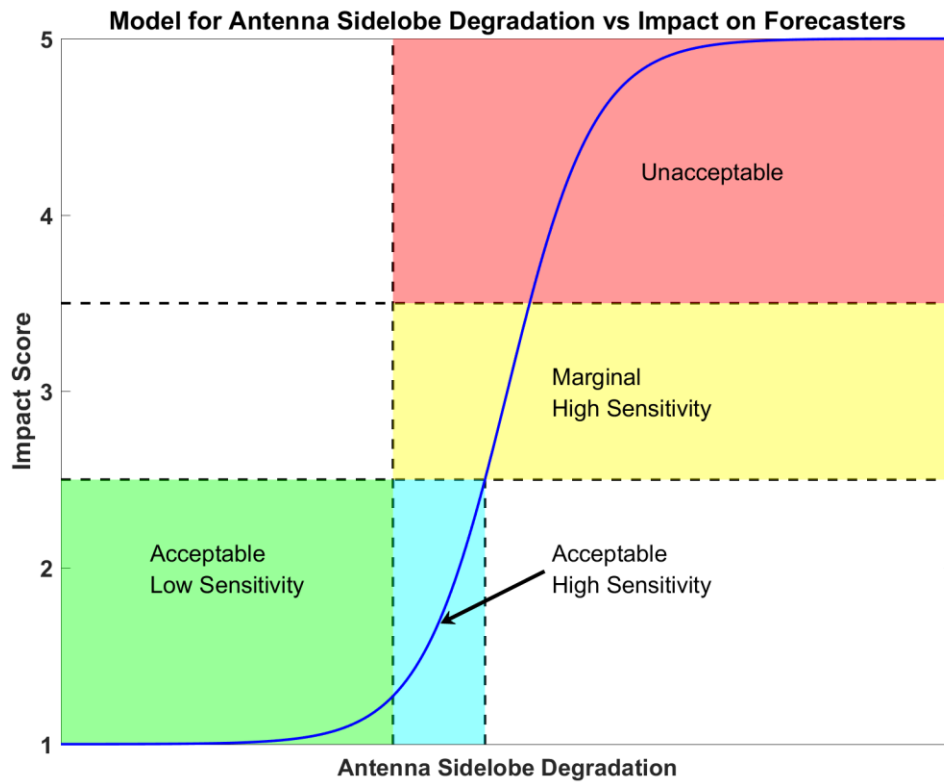


Fig. 2-11. Model for the relationship between relative antenna sidelobe degradation and impact on forecasters. Based on the impact score, there are three regions: acceptable, marginal, and unacceptable. Within the acceptable region, the model curve falls in two separate regions: low sensitivity and high sensitivity. Sensitivity describes how quickly the impact score changes when the relative antenna sidelobe degradation changes.

The impact model is a function of the vertical reflectivity gradients in the storm under analysis. For the cases that we chose, the vertical reflectivity gradients are close to the maximum that the WSR-88D can observe without producing compromised data. We refer to these cases as “upper bound” WSR-88D storms. That is, storms more demanding than the WSR-88D “upper bound” storms would cause compromised data in the WSR-88D. In general, a future radar system could be designed to observe different “upper-bound” storms. That is, a future radar system may be required to produce uncompromised data for storms with different maximum vertical reflectivity gradients, and this “upper-bound” storm would drive the sidelobe requirement. If the “upper-bound” storm is less demanding than the “upper bound” WSR-88D storm, the model curve

must be shifted to the right. That is, for the same sidelobes, the impact score for the new “upper-bound” storm is lower. Conversely, if the “upper-bound” storm is more demanding, the model curve must be shifted to the left. That is, for the same sidelobes, the impact score for the new “upper-bound” storm is higher. Therefore, the impact model could be used by decision makers in two ways. The first use is to estimate the consequences of degradation for a given radar design. In other words, the model can be used to evaluate how much impact would occur if a system’s ISL failed to meet requirements by a certain amount. The second use is to evaluate the robustness of a given design to storms more demanding than the “upper bound” storm. To use the impact model for these applications, we would first need to convert the x-axis into the absolute ISL, which is usually inversely related to system cost. This step could be done by measuring the antenna pattern of the WSR-88D precisely or by constructing an accurate model of the WSR-88D pattern at different sites using available measurements. With this conversion of the x axis, any potential radar design could be placed directly on it using its absolute ISL. Moreover, as we argued above, we also need to shift the model curve on the x axis to match the required “upper bound” storm. This could be accomplished by averaging the scores of WSR-88D data for a large number of storms with these required “upper bound” vertical reflectivity gradients that are particular to each radar design. Then, a sigmoidal curve with the same steepness as the model in Fig. 2-11 can be fit to this average score. Doing these two things would allow decision makers to evaluate the operational impact of potential radar designs depending on where they land on the model curve.

After making the necessary changes described before, different radar designs could be evaluated using the impact model in Fig. 2-11. If a radar design results in an ISL that falls in the marginal or unacceptable region, then the data quality impacts for such a design are unlikely to be tolerable to forecasters. If a radar design results in an ISL that falls in the acceptable region, then

decision makers can use the model to balance trade-offs between system cost and potential operational impacts. Radar designs with ISLs that fall in the acceptable with low sensitivity region can tolerate more degradation and are more robust against worst-case-scenario storms, but they likely have higher system cost. In contrast, radar designs with ISLs that fall in the acceptable with high sensitivity region likely have lower system cost, but any increase in sidelobe levels can quickly lead to rapidly increasing impacts on forecasters. Such systems are also less robust to storms more demanding than the “upper bound” storm. Similar analyses can be performed to determine sidelobe requirements that balance system cost and operational impact on forecasters since each set of sidelobe requirements can be placed on to the impact curve using its ISL. Conversely, once an acceptable ISL is determined (i.e., the x-coordinate of a point on the impact curve), it can be used to define an envelope similar to those in Fig. 2-2 by assuming any realistic pattern structure (e.g., sidelobes that gradually decay away from broadside). Exceptions similar to those in the WSR-88D system specifications can be made for isolated sidelobes caused, for example, by struts. After studying the impacts of changing antenna sidelobe levels on forecasters’ interpretation of radar data, we investigate the impacts of the beam broadening effects of a planar PAR next.

## **2.3. Impact of Beam Broadening for Planar PAR**

### **2.3.1. Simulation Methodology**

To study the data quality impacts of the beam broadening effect of a planar PAR, we need to simulate radar data with varying angular resolution. The current angular resolution requirement specifies that the beamwidth must be less than or equal to  $1^\circ$  for all scanning angles (NOAA/NWS 2015). Fig. 2-12 illustrates the beamwidth variation as a function of scanning angle for one face of a four-phased PAR that meets the current requirement. Such a system will be referred to as a

full-size PAR. In this illustration, the radar is assumed to be scanning in azimuth (represented by the horizontal axis) at a constant elevation angle near  $0^\circ$ , and each beam is represented by a colored ellipse. The major axis of each ellipse represents the azimuthal beamwidth of the antenna pattern when pointing in the direction corresponding to the center of that ellipse. As shown in Fig. 2-12, a full-size PAR will have a beamwidth of  $0.7^\circ$  at broadside (i.e.,  $0^\circ$  on the horizontal axis) and  $1^\circ$  at  $\pm 45^\circ$  away from broadside. Simulating data from a full-size PAR is not possible using the method described in section 2.2.1 because the intrinsic WSR-88D pattern in the input data limits the minimum beamwidth that can be simulated to  $1^\circ$  (see section 2.2.1). One way to address this challenge is to use radar data with angular resolution better than  $0.7^\circ$  as the input to the SPARC simulator. However, this approach would significantly limit the number of weather types and cases that can be simulated. Another approach is to simulate data from a PAR with beamwidth that varies between  $1^\circ$  (at broadside) and  $1.4^\circ$  (at  $\pm 45^\circ$  off broadside). This PAR (referred to as the scaled PAR) does not meet the current angular resolution requirement but meets a scaled angular resolution requirement, where the scaled angular resolution requirement is given by the current requirement multiplied by square root of 2. Fig. 2-13 illustrates the beamwidth variation as a function of scanning angle for the scaled PAR. Using data from a scaled PAR to study the data quality impacts from a full-size PAR is reasonable as long as the data from the scaled PAR is being compared to data from a scaled reference system where the relative differences in data quality are similar to those between data from the full-sized PAR and data from the WSR-88D. Alternatively, radar data from this scaled PAR can be treated as range-shifted data from the full-size PAR. That is, radar data at 100 km for the scaled PAR would be the same as radar data at about 140 km for the full-size PAR. We decided to conduct this study using simulated data for a scaled PAR because it allows us to use WSR-88D archived data as the input to the SPARC simulator.

## The Atmosphere

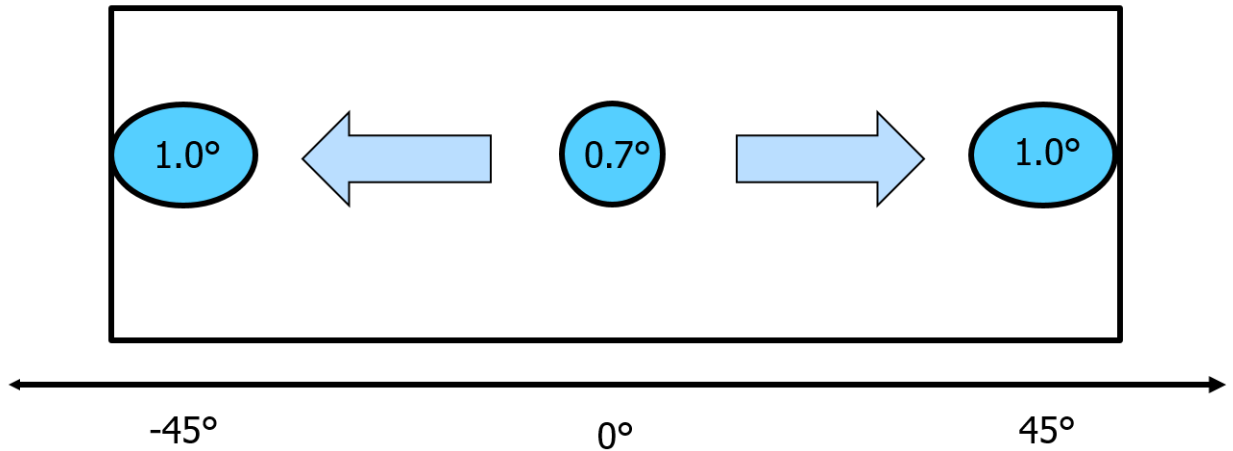


Fig. 2-12. Illustration of the beamwidth variation as a function of scan angle for a full-size PAR. The radar is assumed to be scanning in azimuth at a constant  $0^\circ$  elevation.

## The Atmosphere

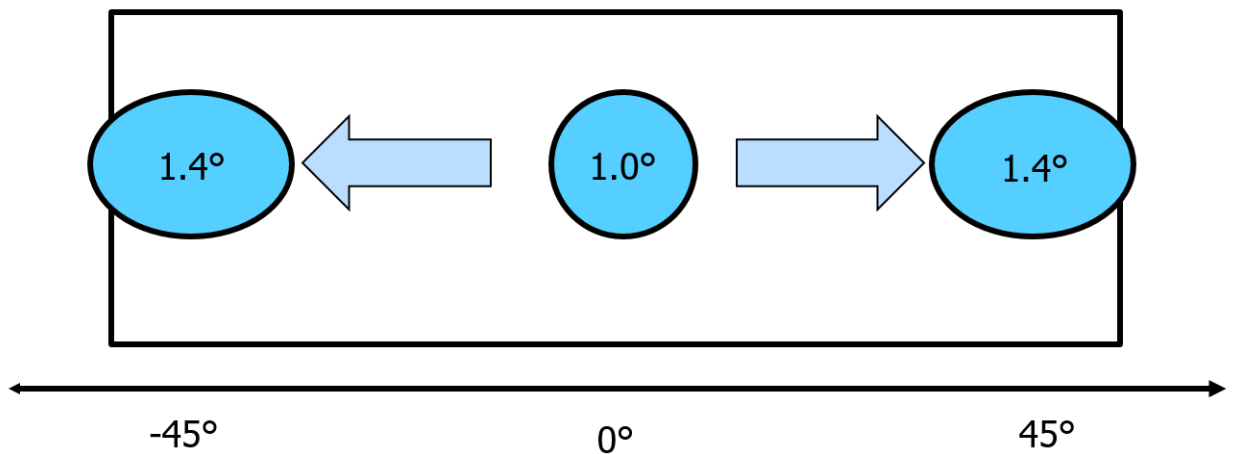


Fig. 2-13. Same as Fig. 2-12 except for a scaled PAR.

To simulate data from the scaled PAR, a similar process to those described in section 2.2.1 is used. Since this study focused on azimuthal beamwidth, scattering centers at one elevation are used for each case. Moreover, the azimuthal extent of the non-zero scattering center weights is significantly reduced for this study compared to the study on impacts from changing sidelobe

levels. For each scan angle, only scattering centers located at  $\pm 0.75^\circ$ ,  $\pm 0.5^\circ$ , and  $\pm 0.25^\circ$  away from the direction of interest received a constant non-zero weight. For each scan angle, the KOUN pattern shown in Fig. 2-2 is convolved with a set of scattering center weights to generate an approximation of the simulated pattern in the azimuth dimension. The magnitude of the scattering center weights is then systematically adjusted until the desired beamwidth is achieved.

To determine the impact of beam broadening effects, it is important to compare simulated PAR data to data with constant angular resolution. The ideal comparison is between data from a full-size PAR and data from a WSR-88D. However, since we can only simulate data from a scaled PAR, we must simulate data from a scaled WSR-88D as well to preserve the relative differences between the two systems being compared. The scaled WSR-88D system has a constant beamwidth of  $1.4^\circ$  and will be referred to as the CB- $1.4^\circ$  system. It is important to note that conclusions from comparing data from a scaled PAR to data from the CB- $1.4^\circ$  system will carry over to comparisons between data from a full-size PAR and data from the WSR-88D. In addition to comparisons between the scaled PAR and the CB- $1.4^\circ$  system, we can also compare the scaled PAR to the WSR-88D (also referred to as the CB- $1.0^\circ$  system). This comparison can demonstrate the impacts to forecasters if the angular resolution requirement were not met by the replacement system in order to reduce system cost.

To isolate the effects of beam broadening, we used the same azimuthal sampling grid when comparing two systems. For comparisons between the scaled PAR and the CB- $1.4^\circ$  system, a uniform sampling grid with an azimuthal sampling interval of  $0.7^\circ$  was used. This mimics super-resolution sampling that is used by the WSR-88D (i.e., 50% overlap between adjacent beams for the CB- $1.4^\circ$  system). For comparisons between the scaled PAR and the CB- $1.0^\circ$  system, a uniform sampling grid with an azimuthal sampling interval of  $0.5^\circ$  was used. Moreover, for each weather

case, the same time-series data for a set of scattering centers with  $0.01^\circ$  azimuthal spacing were used to generate time-series data for each dwell. Using the same realizations and the same digital signal processor eliminated many factors that can contribute to observable differences in the simulated radar data. Additionally, since the beamwidth of the scaled PAR changes as a function of the scanning angle, it is important to simulate scenarios where the weather features of interest are located at different positions with respect to the broadside of the array. For each weather case we used in this study, we simulated three possible positions for the weather features by rotating the scaled PAR in azimuth. For the three simulated weather positions, weather features are located at broadside, at  $22.5^\circ$  away from broadside (referred to as halfway), and at  $45^\circ$  away from broadside (referred to as edge).

### **2.3.2. Case Selection and Data Analysis Process**

The case selection for this study requires a broad spectrum of weather threats with signatures at differing spatial scales. Table 2-4 summarizes the specific cases used, and their types: winter, convective and circulation. The winter events present broad scale but subtle features that are important for the forecasting of precipitation type at the surface, such as a refreezing ring close to the radar as indicated by the arrows in Fig 2-14. The features of interest in convective events are at storm scale, such as bow echoes (in the circled area in Fig. 2-15), an outflow boundary very close to a storm with an intense hail core, or a well-defined interface between the hail core and big drops. The circulation cases are at sub-storm scale, meaning the circulation itself is the feature of interest (indicated by the arrow Fig. 2-16). The presentation of all of these features is the key criteria of the data analysis process when comparing simulated data from different radar systems.

Table 2-4. Selected weather cases to evaluate impacts of variable beamwidth on forecasters' data interpretation process.

Case Number	Date and Radar	Type
1	20:37 Z 02 March 2014, KTLX	Winter
2	12:11 Z 19 November 2014, KBUF	Winter
3	00:01Z 04 January 2015, KENX	Winter
4	22:40Z 04 March 2015, KLVX	Winter
5	23:49Z 03 May 2012, KBGM	Convective
6	23:25Z 10 September 2015, KTWX	Convective
7	20:06Z 30 June 2014, KDVN	Convective
8	11:59Z 27 June 2014, KOAX	Convective
9	03:02Z 29 February 2012, KTWX	Circulation
10	07:09Z 29 February 2012, KSGF	Circulation
11	00:23Z 19 May 2013, KDDC	Circulation
12	22:51Z 27 May 2013, KUEX	Circulation
13	21:19Z 28 May 2013, KTWX	Circulation
14	03:53Z 18 June 2014, KFSD	Circulation
15	01:19Z 11 September 2015, KTWX	Circulation
16	00:28Z 26 May 2016, KTWX	Circulation

The analyses for this study were done by comparing simulated data from the scaled PAR to simulated data from the CB-1.4° or CB-1.0° systems. Because the differences in the data are very subtle, the 5-level distraction-based scoring system like the one used in the elevation sidelobe study cannot be used. Instead, the comparison assessment was mainly based on the representation of the threat for a particular case. That is, we assessed which system produced data with better presentation of the weather threat. If the threat is equally presented by the data from the two systems being compared, we assessed them to be the same. Note that “same” does not imply identical data for each range location. It is possible for pixel-by-pixel differences to exist while the general threat is presented equally. These differences and their relevance are documented in our analysis notes.

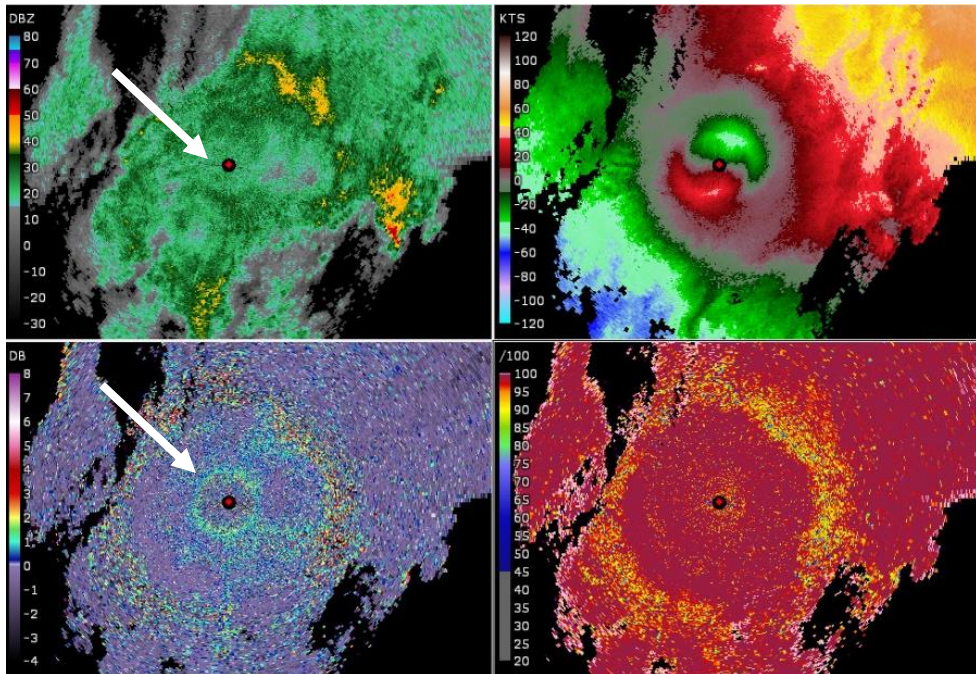


Fig. 2-14. Reflectivity (top left), mean Doppler velocity (top right), differential reflectivity (bottom left) and correlation coefficient (bottom right) from the WSR-88D for Case 1. The weather features of interest are the subtle ring in differential reflectivity and lower reflectivity close to the surface (indicated by the arrows), which indicate a refreezing process and sleet at the surface.

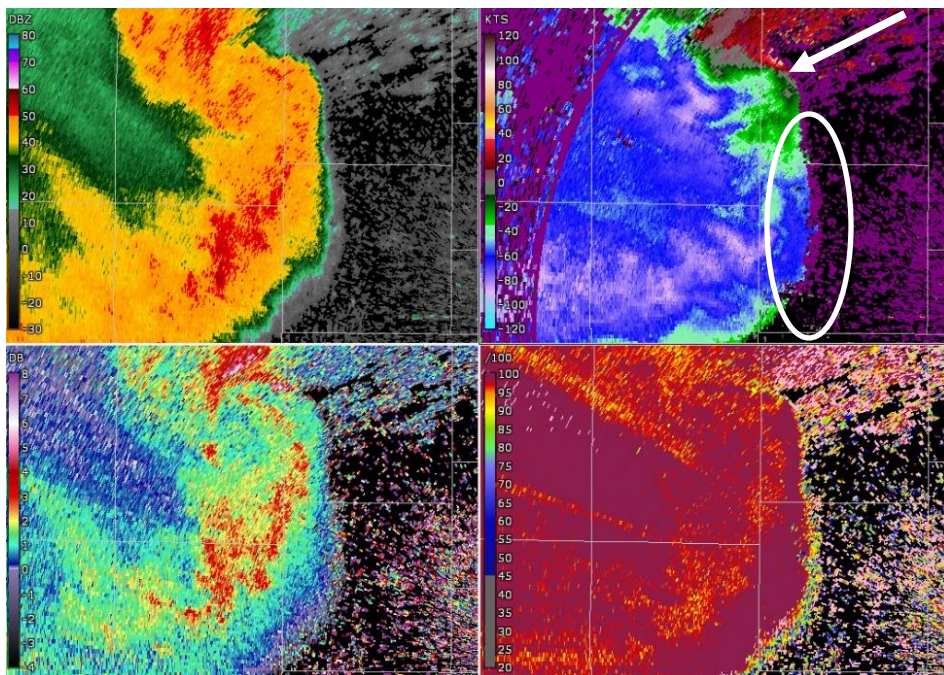


Fig. 2-15. Same as Fig. 2-14 except for Case 7. The weather features of interest are the bow echo with extreme winds just off the surface (circled) and a hint of a small circulation on the northern edge (arrow).

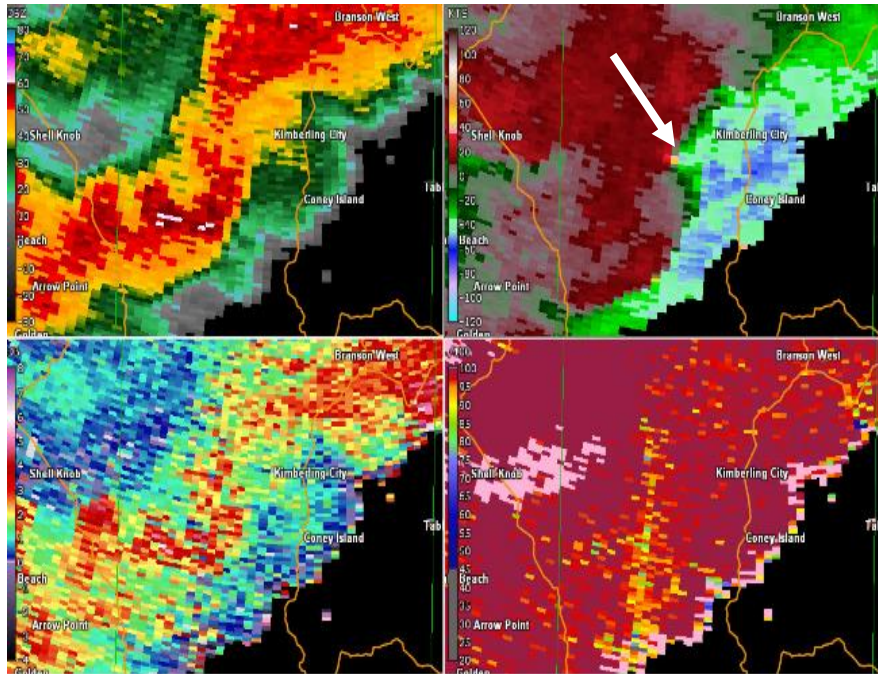


Fig. 2-16. Same as Fig. 2-14 except for Case 10. The weather feature of interest is the small circulation (arrow) along a line of storms that became a damaging nighttime tornado for locations in Missouri, including Branson.

To demonstrate our analysis process for winter cases, we show simulated data for Case 1 in Figs. 2-17 to 2-19. In these figures, the left four panels show simulated data from the CB-1.4° system, and the right four panels show simulated data from the scaled PAR system where the radar is rotated such that the broadside of the array is pointed at 0°, 22.5°, and 45° in azimuth. For this type of winter event, the most important features of interest are the circular ring of slightly increased differential reflectivity and the decreased reflectivity very close to the radar. These features indicate refreezing of the hydrometeors and imply the presence of sleet at the surface. Another feature of interest is the melting layer that can be easily seen in the correlation coefficient field. Comparisons between simulated data from the CB-1.4° system and the scaled PAR system in Figs. 2-17 to 2-19 clearly show that there are no meaningful differences between them. That is, the most important weather features are presented equally well in data from both systems. Therefore, data from the two systems are assessed to be the same for this case. A screenshot of our

analysis notes is shown in Fig. 2-20 where we mention that there are differences at the individual pixel level. However, these differences do not hinder interpretation of the threat (i.e., presence of sleet at the surface). The remaining winter cases were analyzed in a similar way for all comparisons.

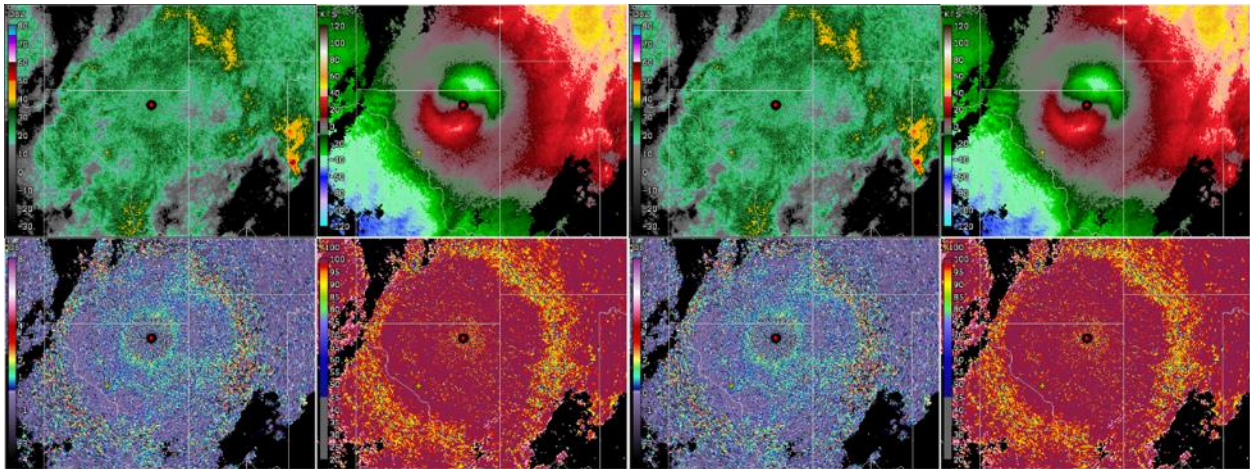


Fig. 2-17. Simulated data for Case 1 from the CB-1.4° system (left four panels) and the scaled PAR system (right four panels) where the broadside of the array is at 0° azimuth.

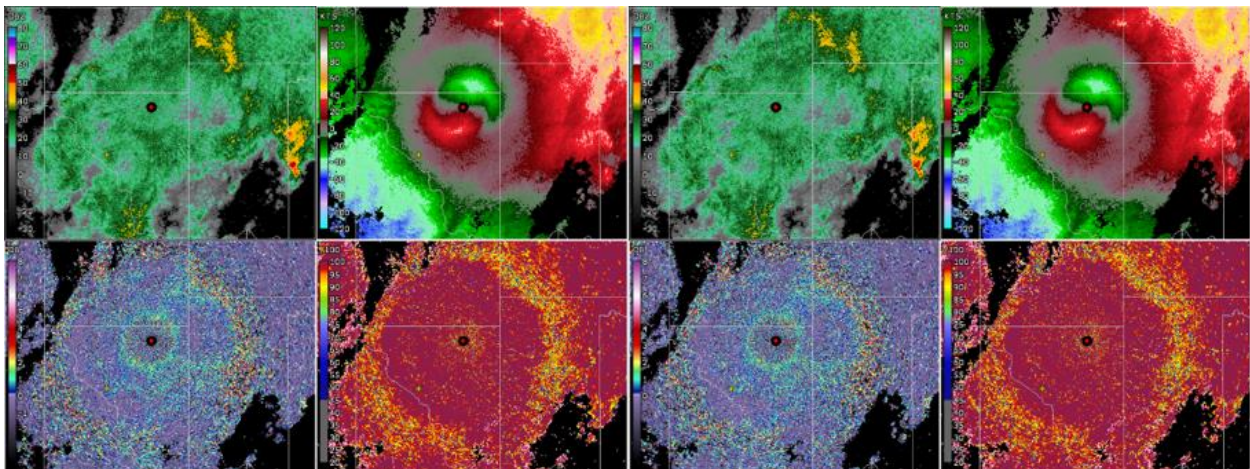


Fig. 2-18. Same as Fig. 2-17 except the broadside of the array is at 22.5° azimuth.

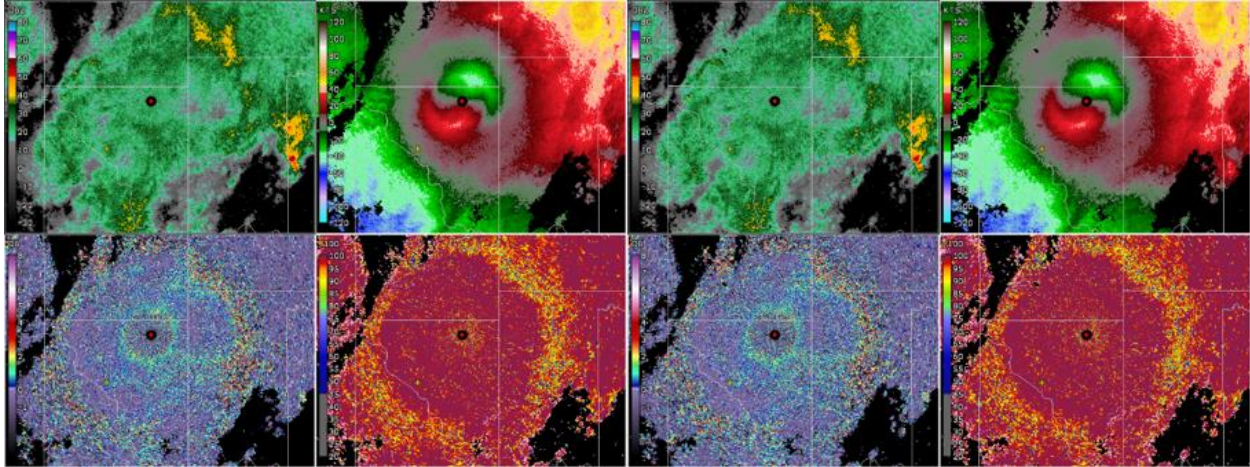


Fig. 2-19. Same as Fig. 2-17 except the broadside of the array is at 45° azimuth.

KTLX March 2, 2014

- Winter storm with near circular shallow melting layer and circular refreezing signature just above the surface
- Key question: do the resolution differences across the PAR antenna affect interpretation?

PAR Antenna Position	Same	Better	Notes/Unexpected Findings
0°	X		Pixel to pixel differences, but no issues with interpretation
22.5°	X		Pixel to pixel differences, but no issues with interpretation
45°	X		Pixel to pixel differences, but no issues with interpretation

Fig. 2-20. Data analysis notes documenting any other differences in the data and their relevance to threat assessment.

The features of interest in the convective cases are different from the winter cases. For Case 5, the feature of interest is the small outflow boundary very close to the edge of a storm with an intense hail core. The feature of interest for Case 6 is the sharp boundary between adjacent areas of hail and big drops that can be seen in differential reflectivity. Cases 7 and 8 are bow echo events where the location of the strongest wind is of interest. To demonstrate our analysis process for

convective cases, Fig. 2-21 shows simulated data for Case 6. The left four panels show simulated data from the CB-1.0° system, and the right four panels show simulated data from the scaled PAR system where the sharp boundary between hail and big drops (i.e., the circled areas in Fig. 2-21) are located 45° away from the broadside of the array. In this scenario, the beamwidth of the scaled PAR system in the direction of the feature of interest is ~1.4°. Because the feature of interest for this case is oriented radially, the difference in beamwidth between the two systems is most likely to cause data quality differences. Comparing the differential reflectivity fields, the boundary between the area along the storm edge containing big drops and the area within the core of the storm containing hail is less distinct in the simulated data from the scaled PAR system. Therefore, we scored data from the CB-1.0° system to be better for this case. Note that although the subtle differences in the data caused us to score the CB-1.0° system as better, there are no artifacts in the data from the scaled PAR system that would negatively impact forecasters' interpretation of the data. That is, the area of big drop and hail core can still be identified in the data from the scaled PAR.

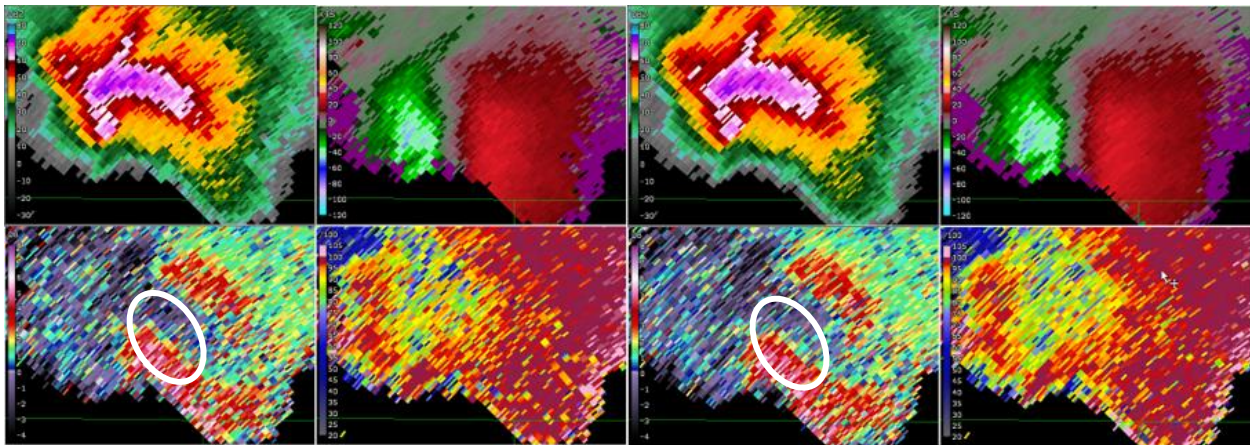


Fig. 2-21. Simulated data for Case 6 from the CB-1.0 ° system (left four panels) and the scaled PAR system (right four panels) where the boundary between hail and big drops is 45° away from array broadside.

For the circulation cases, the feature of interest is the circulation itself. Our analysis focused both on the structural appearance and the rotational velocity estimated by a forecaster from radar measurements of the circulation (this will be referred to simply as radar-measured rotational velocity). To demonstrate our analysis process for circulation cases, Fig. 2-22 shows the comparison between simulated data for Case 16 for the CB-1.4° system and the scaled PAR system where the circulation (i.e., the circled areas in Fig. 2-22) is located 22.5° away from broadside. In this example, we assessed the data from the scaled PAR system to be better because it presented a tighter and stronger circulation. The radar-measured rotational velocities for the CB-1.4° system and the scaled PAR system are 66 kts and 80 kts, respectively. Fig. 2-23 shows the comparison between simulated data for Case 10 between the CB-1.0° system and the scaled PAR system where the circulation (i.e., the circled areas in Fig. 2-23) is located 45° away from array broadside. The circulation in this example is the beginning of a long track tornado where the quality of the initial signature is vital for the recognition of this circulation along the lines of storms. Although the radar-measured rotational velocities are similar, the circulation is tighter and more visually salient in the data from the CB-1.0° system. Therefore, we scored data from the CB-1.0° system as better.

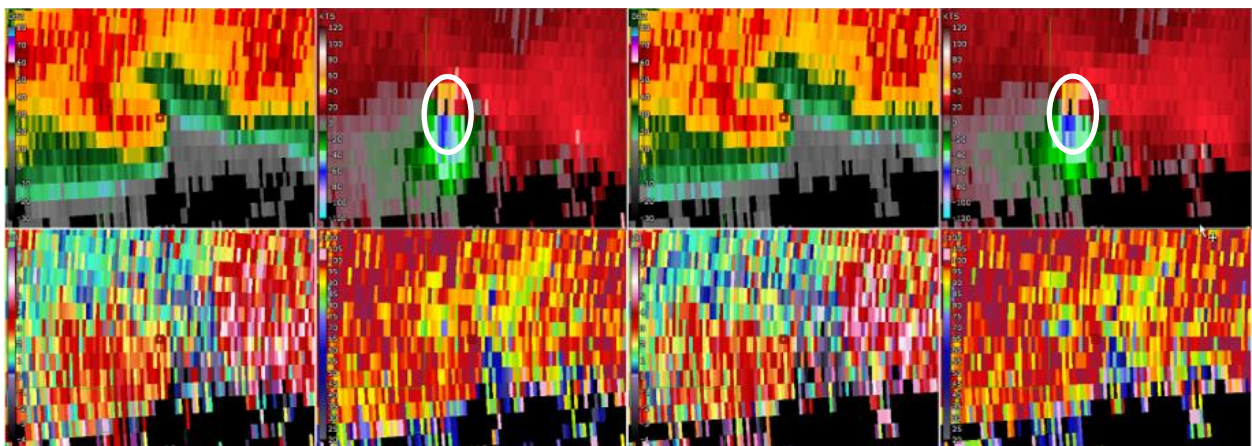


Fig. 2-22. Simulated data for Case 16 from the CB-1.4 ° system (left four panels) and the scaled PAR system (right four panels) where circulation is 22.5° away from array broadside.

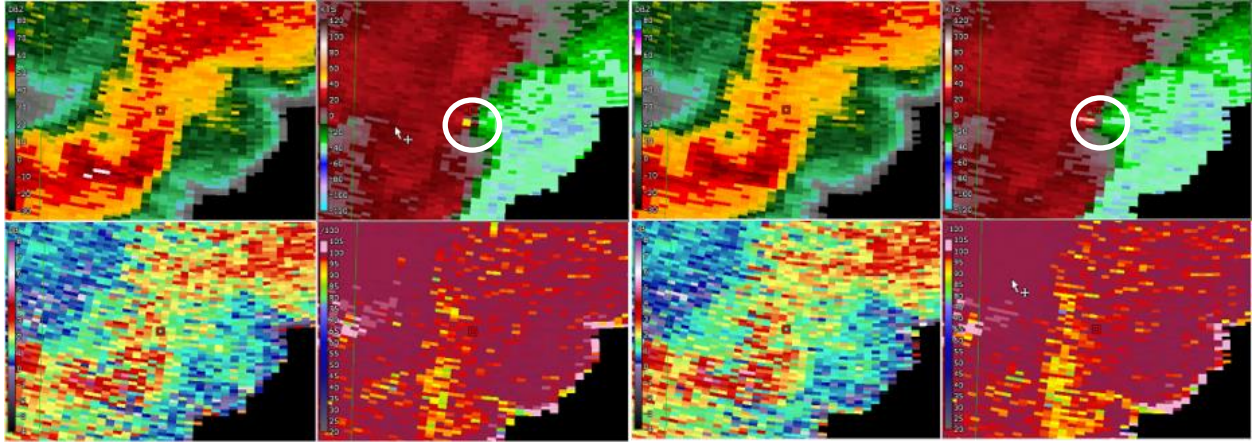


Fig. 2-23. Simulated data for Case 10 from the CB-1.0 ° system (left four panels) and the scaled PAR system (right four panels) where circulation is 45° away from array broadside.

### 2.3.3. Simulation Results

To better understand the impacts of beam broadening effects on forecasters, we calculated the percentage of the cases where one system outperforms the other for each comparison. For each comparison between two simulated systems, 48 sets of data were compared (i.e., 16 cases and three weather feature locations for each case). Fig. 2-24 shows the data comparison results between the scaled PAR and the CB-1.4° system. For non-circulation cases (i.e., cases 1-8 in Table 2-4), data from both systems are judged to have the same quality for all 24 comparisons. For circulation cases (i.e., cases 9-16 in Table 2-4), data from the scaled PAR system have the same quality as data from the CB-1.4° system for 62.5% of the comparisons. For the remaining 37.5% of the comparisons, data from the scaled PAR are better than data from the CB-1.4° system. These results for circulation cases make sense because the beamwidth of the scaled PAR is narrower or equal to that of the CB-1.4° system, and the scaled PAR can better observe the circulation when its location is at broadside or halfway. Overall, the scaled PAR system performs better than the CB-1.4° system in 18.8% of our simulated cases. It is also important to note that data for all simulated cases have acceptable quality. As shown in the previous section, only subtle differences between the data from the scaled PAR and the CB-1.4° cause one to be judged to be better than the other. These

results show that the beam broadening effect does not cause any artifacts in the radar data that can negatively impact forecasters' interpretation. As argued before, these important observations carry over to comparisons between the full-size PAR and the WSR-88D.

The data comparison results between the scaled PAR and the CB-1.0° system are shown in Fig. 2-25. In this comparison, data from the CB-1.0° system has the same quality as the data from the scaled PAR system for 95.8% of the non-circulation cases and 87.5% of the circulation cases. The CB-1.0° system performs better than the scaled PAR for 4.2% of the non-circulation cases and 12.5% of the circulation cases. These results are reasonable because the beamwidth of the CB-1.0° system is narrower or equal to the beamwidth of the scaled PAR system for all the cases. However, note that they perform similarly in 90% of the cases. Fig. 2-26 shows the comparison results grouped by the location of the weather features. When the weather feature is located at broadside or halfway, the two systems perform the same for all cases. The CB-1.0° outperforms the scaled PAR system for 25% of the cases when the weather feature is located at the edge. For a PAR with four stationary faces, these results show that the current beamwidth requirements (i.e., beamwidth  $\leq 1^\circ$  for all scanning angles) must be satisfied to prevent negative impacts on forecasters since the location of the weather feature with respect to array broadside cannot be controlled. However, for a PAR with rotating faces and limited electronic steering in azimuth (i.e., electronically steer the beam to scan only within  $\pm 22.5^\circ$  of the broadside), our results suggest that it may be possible to relax the beamwidth component of the angular resolution requirement to reduce the system cost. That is, a rotating PAR with a beamwidth of  $1^\circ$  at broadside that only electronically steers within  $\pm 22.5^\circ$  can perform similarly to the WSR-88D. Similar to the previous comparison between the scaled PAR and the CB-1.4° system, data for all cases have no artifacts that negatively impact forecasters' interpretation of the data.

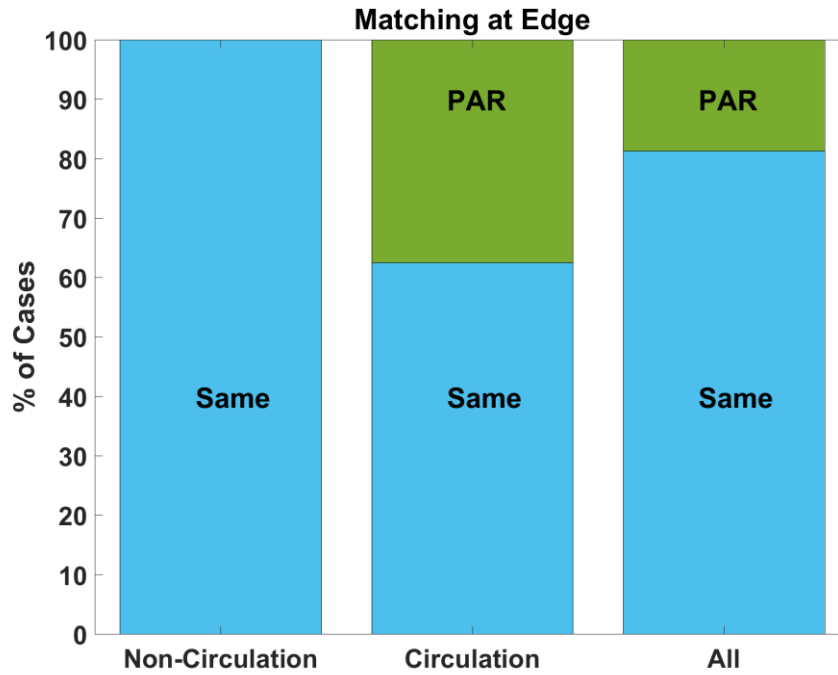


Fig. 2-24. Data comparison results between the scaled PAR and the CB-1.4° system grouped by weather type.

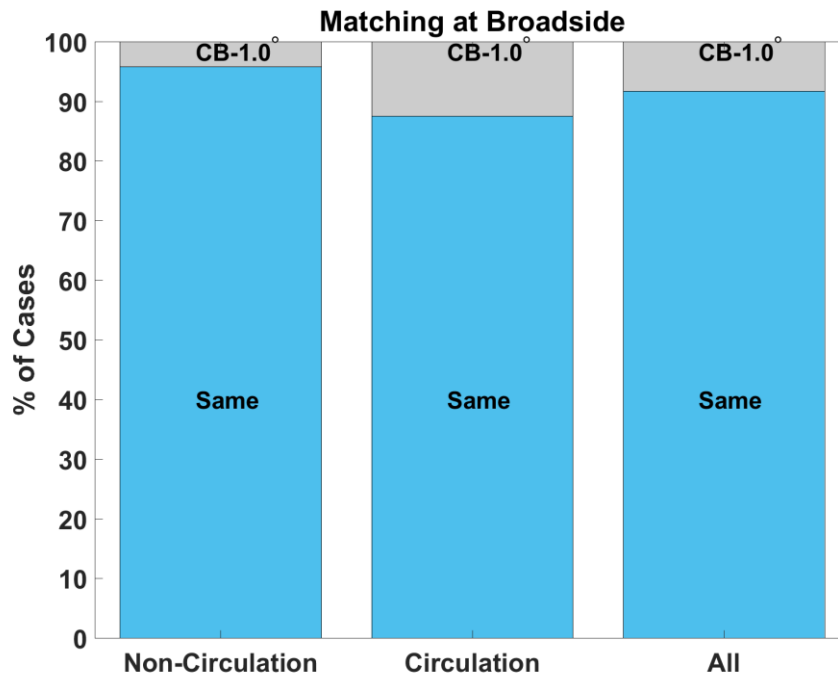


Fig. 2-25. Data comparison results between the scaled PAR and the CB-1.0° system grouped by weather type.

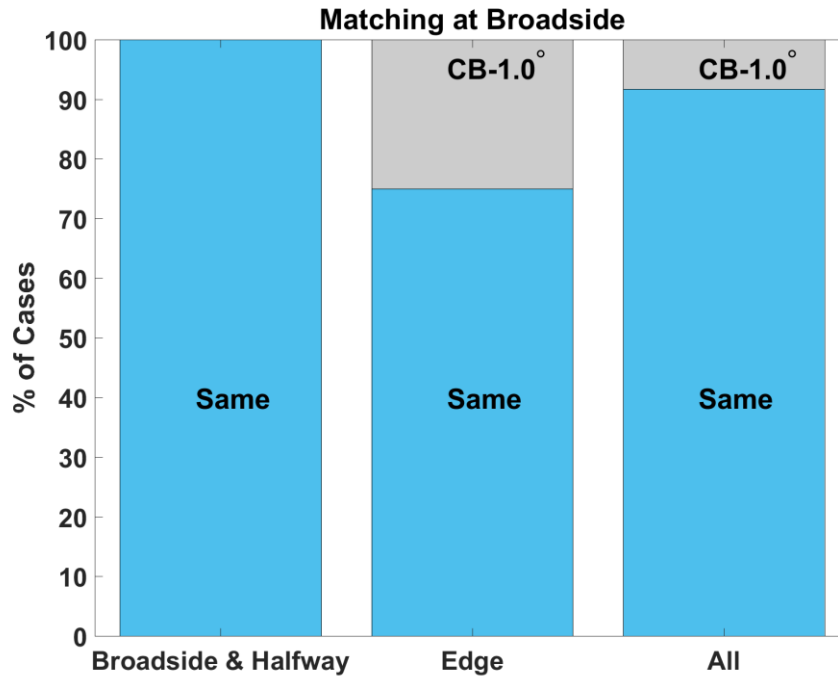


Fig. 2-26. Data comparison results between the scaled PAR and the CB-1.0° system grouped by weather location.

## 2.4. Conclusions

The angular resolution of a radar can be impacted by both the sidelobe levels and the beamwidth of the antenna pattern. To understand the relationship between sidelobe levels and impact on forecasters, we simulated radar data for the same weather event as though it was observed by radar systems with different sidelobe levels. We analyzed and scored the simulated data based on the amount of distractions to forecasters caused by data quality changes. An impact model was constructed using the scores. This model relates changes to sidelobe levels to impacts on NWS forecasters and can be used by decision makers to evaluate future radar designs and proposed sidelobe requirements.

To evaluate the impacts of the beam broadening effect on forecasters, we simulated a scaled PAR with a beamwidth that varies between 1° and 1.4° and two reference systems with a constant beamwidth of 1° and 1.4°, respectively. By simulating different types of weather with weather

features of interest located at different locations with respect to the array, we showed that the beam broadening effect does not cause any artifacts in the data that can negatively impact forecasters' interpretation of radar data. Moreover, for a large majority of non-circulation cases, all three systems perform similarly regardless of their beamwidth. For circulation cases, the scaled PAR performs better than the CB-1.4° system, implying that a full-size PAR could perform better than the WSR-88D assuming other aspects of the radar (e.g., sidelobe levels, sensitivity, etc.) are identical. Lastly, comparisons between the scaled PAR and the CB-1.0° system show that the scaled PAR system is worse only when the weather feature is located at  $\pm 45^\circ$  from the broadside of the array. For a PAR with four stationary faces, these results show that the current beamwidth requirements (i.e., beamwidth  $\leq 1^\circ$  for all scanning angles) must be satisfied to prevent negative impacts on forecasters since the location of the weather feature with respect to array broadside cannot be controlled. However, for a PAR with rotating faces and limited electronic steering in azimuth (i.e., electronically steer the beam to scan only within  $\pm 22.5^\circ$  of the broadside), our results suggest that it may be possible to relax the beamwidth component of the angular resolution requirement to reduce the system cost. That is, a rotating PAR with a beamwidth of  $1^\circ$  at broadside that only electronically steers within  $\pm 22.5^\circ$  can perform similarly to the WSR-88D.

### **3. Impacts of Azimuthal Sampling**

#### **3.1. Introduction**

Accurate representation of the atmosphere in radar data is affected by both the size and the location of the radar resolution volumes. The size of the radar resolution volume is determined by the beamwidth of the antenna pattern in the azimuth and elevation dimension and the width of the range weighting function in the range dimension. The angular location of the radar resolution volumes is determined by the sampling grid in azimuth and elevation. While the elevation sampling grid is set by the volume coverage patterns (VCP), the azimuthal sampling grid is usually determined by an angle table used by the signal processor (Torres and Curtis 2007). To improve radar sampling of the atmosphere, either the beamwidth of the antenna pattern can be reduced or the sampling grid can be modified. For a PAR, decreasing the beamwidth is costly because it involves increasing the antenna size. On the other hand, modifying the sampling grid is less costly. For a traditional dish-antenna radar, the major tradeoff of using a denser sampling grid is increased computational complexity. For a PAR, changing the sampling grid can also increase the volume update-time if more dwells are needed. However, given the flexibility of the PAR to scan electronically, adaptive scanning strategies can be used to reduce the scan time to meet the objective requirement of one-minute-or-less volume update-time. In this study, we assume these practical concerns can be successfully addressed and focus only on the impacts of changing the sampling grid on forecasters' interpretation of the data.

The radar sampling grid in elevation is determined by the VCPs which are designed to balance the volume update time with sufficient sampling in elevation. It is outside the scope of this study to investigate the proper elevation sampling that best samples each type of weather. Instead, we focus on azimuthal sampling. The azimuthal sampling grid is impacted by two factors: the

azimuthal sampling interval, which determines the separation between adjacent radials and the size of each pixel on a plan-position indicator (PPI) plots, and the relative position of the dwells with respect to the weather feature of interest. By changing the azimuthal sampling grid, the same weather feature can potentially be presented differently on a PPI plot, which could impact forecasters' interpretation of the radar data. This is especially relevant for a PAR where it could use an azimuthal sampling grid with non-uniform spacing where the azimuthal sampling interval changes as a function of the scanning angle.

One weather feature where azimuthal sampling could have significant impact is a circulation. Two radar signatures that indicate the presence of a tornado are the tornado signature (TS) and the tornadic vortex signature (TVS). Both signatures are typically recognized in Doppler velocity fields by the presence of extreme inbound and outbound velocities that are separated by approximately one radar beamwidth (e.g., Brown et al. 1978, Brown 1998, Brown et al. 2002, Brown and Wood 2012). The velocities corresponding to the maximum inbound and maximum outbound flow of the circulation can be used by NWS forecasters to estimate the rotational velocity, which is an indicator of circulation strength (Brown et al. 1978, Mitchell et al. 1998). Numerous studies (e.g., Brown et al. 2002, Wood and Brown 1997, Wood et al. 2001) showed that reducing the azimuthal sampling interval can improve the detection of circulations. Therefore, it is important to study the benefits of changing the azimuthal sampling grid and assess the potential impacts on forecasters.

In this study, we first used the SPARC simulator to simulate radar data for the same weather event but using different azimuthal sampling grids. We simulated different types of weather and evaluated the simulated data with different azimuthal sampling grids based on the presentation of the threat. We then investigated the benefits of reducing the azimuthal sampling interval for a

uniform sampling grid on radar observation of circulations. For this part of the study we used a simplified simulator to systematically evaluate the performance of different sampling grids for a large group of circulations. The performance of a sampling grid is evaluated quantitatively by the differences between measured rotational velocity for a sampling grid and the maximum observable rotational velocity. We then corroborated our results with real data. The rest of this section describes the simulation methodology, the case selection process, the data analysis process, and conclusions from our studies on the impact of changing the azimuthal sampling grid.

## **3.2. Azimuthal Sampling for PAR**

### **3.2.1. Simulation Methodology**

To study the impact of azimuthal sampling, we simulated data from the scaled PAR described in section 2.3.1 using three different azimuthal sampling grids. The main sampling grid we want to evaluate for the PAR is a non-uniform sampling grid that is referred to as sine-space sampling. Fig. 3-1 is a simplified illustration of this grid where the azimuthal sampling interval increases from  $0.5^\circ$  between adjacent beams near broadside to  $0.7^\circ$  between beams close to  $\pm 45^\circ$  away from broadside. The azimuthal sampling interval is chosen so that the overlap between adjacent beams (represented by the colored ellipses) is kept constant at 50%. This sampling grid mimics the super-resolution azimuthal sampling grid used by the WSR-88D where the overlap between adjacent beams is also kept constant at 50%. To properly evaluate the impact of using sine-space sampling, we simulated data for the same weather event using two uniform azimuthal sampling grids. The first uniform grid has an azimuthal sampling interval of  $0.5^\circ$  (referred to as  $0.5^\circ$  sampling) and is identical to the sampling grid used by the WSR-88D in super-resolution mode. Since the beamwidth of the scaled PAR varies from  $1^\circ$  to  $1.4^\circ$ ,  $0.5^\circ$  sampling represents a denser sampling grid where beams near broadside are overlapped by 50% and beams away from

broadside are overlapped by more than 50%. Fig. 3-2 illustrates this grid where the increase in overlap can be clearly seen. The second uniform sampling grid has an azimuthal sampling interval of  $0.7^\circ$ . This grid (referred to as  $0.7^\circ$  sampling) represents a coarser sampling grid where beams near broadside are overlapped by less than 50% and beams close to  $\pm 45^\circ$  are overlapped by 50%. Fig. 3-3 illustrates this sampling grid where the coarser spacing of the beams near broadside can be clearly seen. We chose these two uniform grids as references because they represent the extremes of reasonable grids that can be used by a PAR to sample the atmosphere without having large gaps between adjacent beams or excessively large numbers of radials. Similar to the study described in section 2.3, we simulated three possible positions for the weather features for each case by rotating the scaled PAR in azimuth. This ensures that we fully capture the impact of azimuthal sampling regardless of the beamwidth. For each case and each weather feature location, data with different sampling grids are compared pairwise to evaluate the potential impact on forecasters from sampling grid changes.

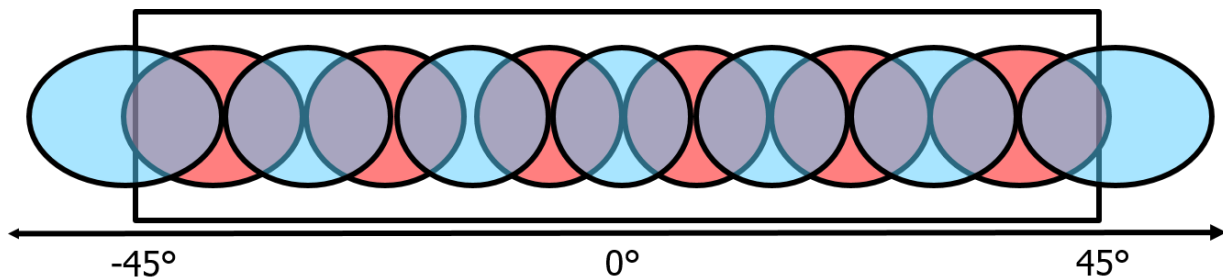


Fig. 3-1. Illustration of sine space sampling where the azimuthal sampling interval increases from  $0.5^\circ$  at broadside to  $0.7^\circ$  at  $\pm 45^\circ$ . For all directions, the overlap between adjacent beams is kept constant at 50%.

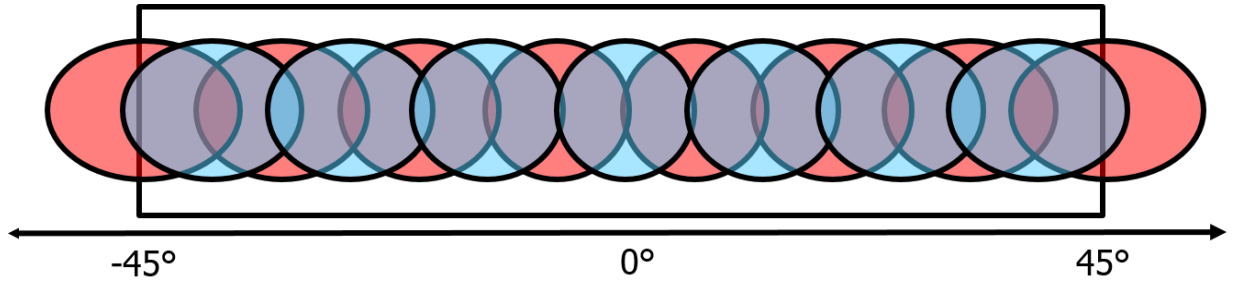


Fig. 3-2. Illustration of  $0.5^\circ$  sampling where the azimuthal sampling interval is kept constant. Note that the overlap between adjacent beams increases from 50% at broadside to 65% at  $\pm 45^\circ$ .

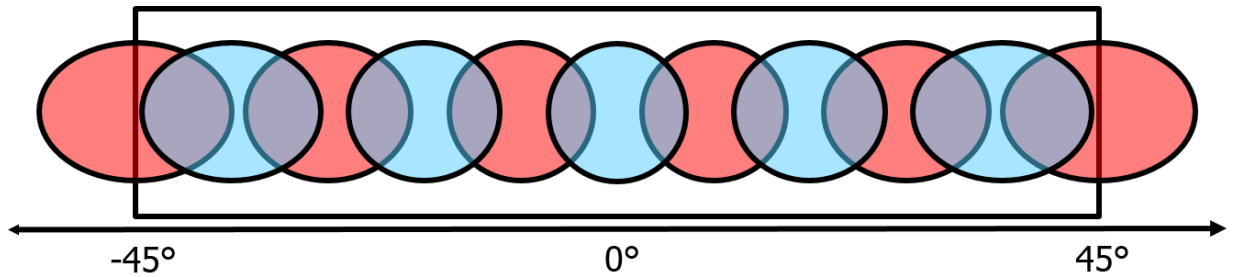


Fig. 3-3. Illustration of  $0.7^\circ$  sampling where the azimuthal sampling interval is kept constant. Note that the overlap between adjacent beams decreases from 50% at  $\pm 45^\circ$  to 30% at broadside.

### 3.2.2. Data Analysis Process

For this study, we simulated data from the scaled PAR for the same weather cases listed in Table 2-4. We performed three comparisons between simulated data for each weather case: between  $0.5^\circ$  sampling and  $0.7^\circ$  sampling, between  $0.5^\circ$  sampling and sine-space sampling, and between  $0.7^\circ$  sampling and sine-space sampling. The comparative analysis process was chosen because the differences in data quality for different sampling grids are subtle. Our criteria for deciding which sampling grid resulted in better data quality are identical to those used in section 2.3. That is, our assessment of the sampling grids are based on which sampling grid resulted in data that better present the weather features. If data with different sampling grids present the weather feature equally, then they are assessed to be the same even if differences at the pixel level exist. Next, we show some examples to demonstrate our analysis process.

The first example we show is a comparison between sine-space sampling and  $0.7^\circ$  sampling for Case 5 in Table 2-4. In this case, the weather feature of interest is the small outflow boundary very close to the storm edge for a storm with an intense hail core. Fig. 3-4 shows reflectivity (left column) and storm-relative velocity (right column) from a scaled PAR system for this storm with sine-space sampling (top row) and  $0.7^\circ$  sampling (bottom row). In this example, the broadside of the scaled PAR is pointed in the direction of the clear-air gap (i.e., the circled area in Fig. 3-4) between the storm edge and the gust front. Because the broadside of the scaled PAR has a beamwidth of  $1.0^\circ$ , the atmosphere is more coarsely sampled when using  $0.7^\circ$  sampling. That is, the overlap between adjacent beams is less than 50% (see Fig. 3-3 near  $0^\circ$ ). This coarse sampling resulted in smoother reflectivity gradients near the edge of the storm and less apparent clear-air gap (i.e., compare the top left and bottom left panels in Fig. 3-4). Because of these subtle differences, we assessed sine space sampling to be better in this case.

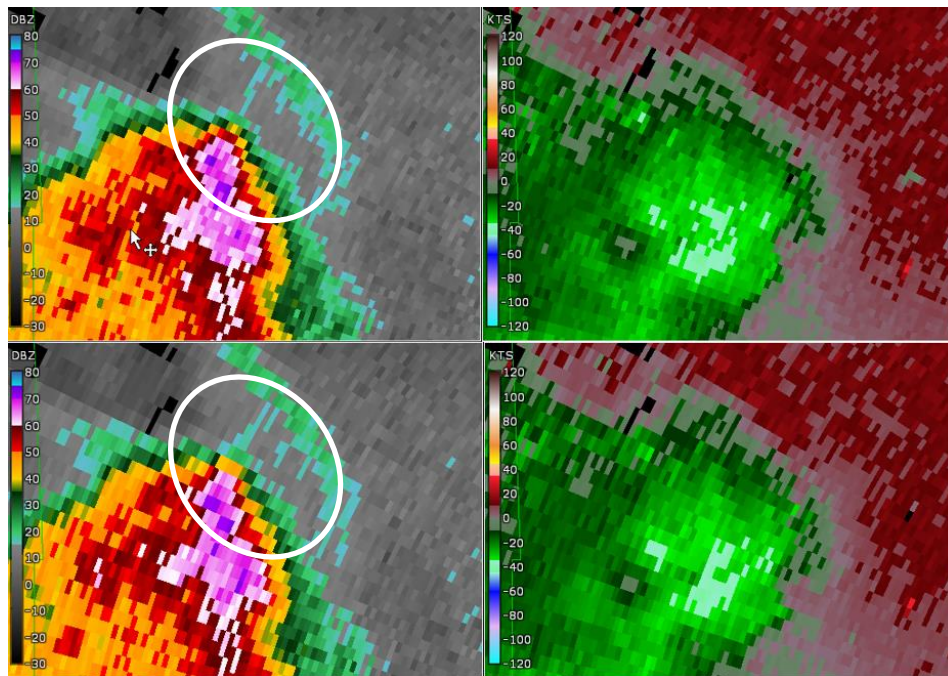


Fig. 3-4. Reflectivity (left column) and storm-relative velocity (right column) for Case 5 with sine-space sampling (top row) and  $0.7^\circ$  sampling (bottom row). The broadside of the PAR is in the direction the clear-air gap between the storm and the gust front in these simulations.

Fig. 3-5 shows the reflectivity (top row) and differential reflectivity (bottom row) between  $0.7^\circ$  sampling (left column) and  $0.5^\circ$  sampling (right column) for Case 6 in Table 2-4. The weather feature of interest in this case is the radially oriented interface between the areas of big drops and hail in differential reflectivity (i.e., the circled area in Fig. 3-5). In this example, the broadside of the scaled PAR is pointed in the direction of the interface. Similar to the previous example, the sampling grid with  $0.7^\circ$  azimuthal sampling interval leads to a coarser sampling of the atmosphere and results in a less sharp and less apparent boundary in differential reflectivity (i.e., compare the bottom left and bottom right panels in Fig. 3-5). Because of these subtle differences, we assess  $0.5^\circ$  sampling to be better in this case.

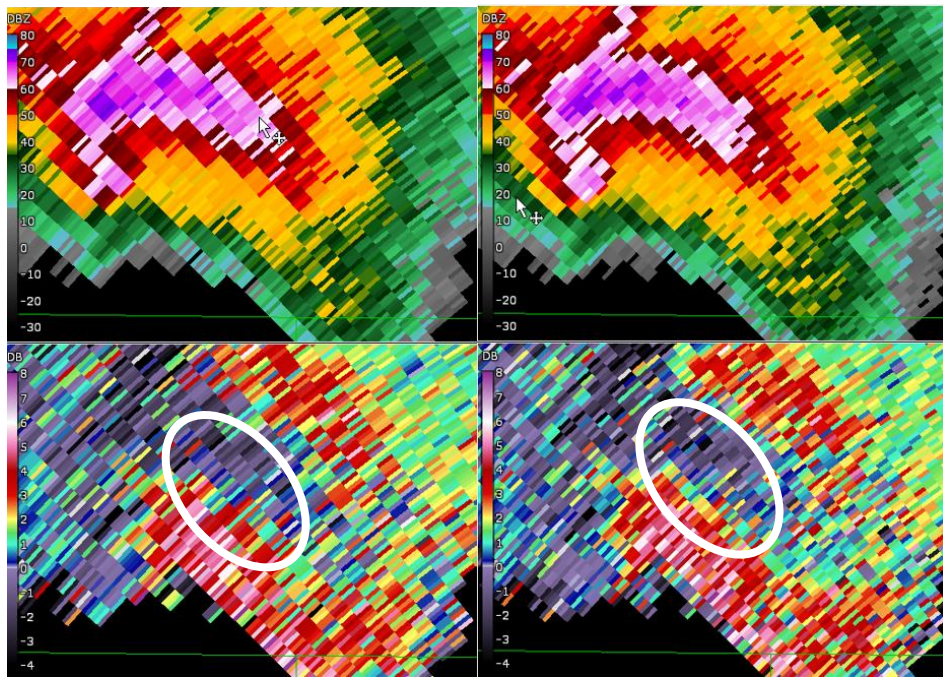


Fig. 3-5. Reflectivity (top row) and differential reflectivity (bottom row) for Case 6 with  $0.7^\circ$  sampling (left column) and  $0.5^\circ$  sampling (right column). The broadside of the PAR is in the direction the interface between areas of big drops and hail.

For the circulation cases, the intensity and saliency of the circulation are used to assess which sampling grid is better. The intensity of the circulation is captured by the peak inbound and outbound velocities. The saliency of the feature depends on the smoothness of the velocity fields

around the circulation and the spatial separation of the peak velocities. For example, a gate-to-gate presentation of the circulation can make it more salient to NWS forecasters. Fig. 3-6 shows the reflectivity (left column) and storm-relative velocity (right column) for Case 10 in Table 2-4 where  $0.5^\circ$  sampling (top row) and  $0.7^\circ$  sampling (bottom row) resulted in different presentations of the circulation (i.e., the circled area in Fig. 3-6). In this example, the scaled PAR is oriented such that its broadside is pointed  $22.5^\circ$  away from the center of the circulation. Comparing the top right and bottom right panels in Fig. 3-6, it is clear that  $0.7^\circ$  sampling resulted in a more salient presentation of the circulation. That is, the feature is more eye-catching and easier to identify. Additionally, it resulted in a higher rotational velocity, which indicates a stronger circulation. Since the saliency of the circulation is particularly important for the initial tornado warning decision, which is often the most challenging and most impacted by the data quality (Andra et al. 2002), we assessed  $0.7^\circ$  sampling to be better in this example.

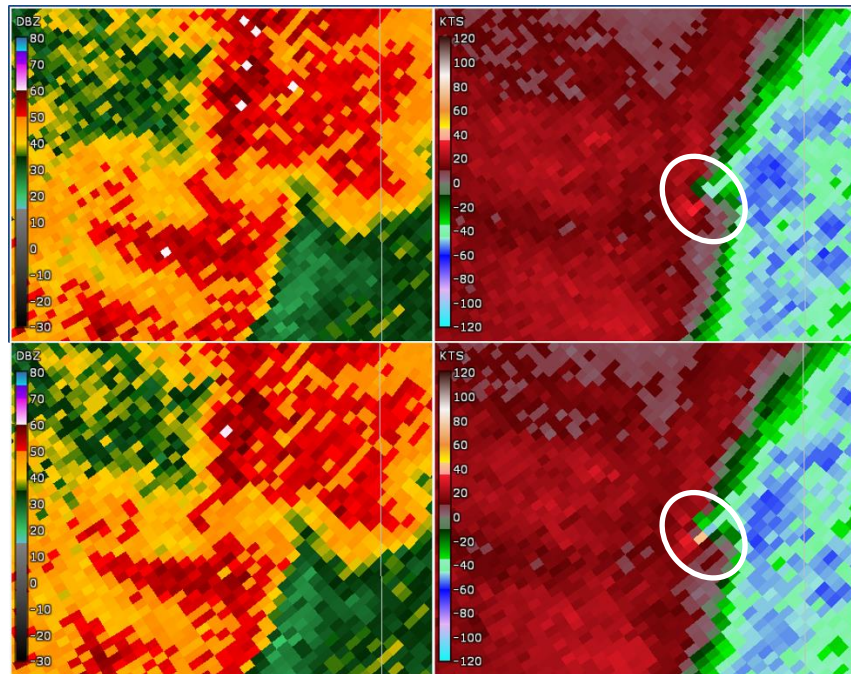


Fig. 3-6. Reflectivity (left column) and storm-relative velocity (right column) for Case 10 with  $0.5^\circ$  sampling (top row) and  $0.7^\circ$  sampling (bottom row). The broadside of the PAR is  $22.5^\circ$  away from the center of the circulation.

### 3.2.3. Simulation Results

To better understand the impacts of changing azimuthal sampling grid on forecasters, we calculated the percentage of the cases where one azimuthal sampling grid outperforms the other for each comparison between two grids. In total, 24 sets of data were compared for non-circulation cases and 24 sets of data were compared for circulation cases. Fig. 3-7 shows the results for the three grid comparisons for non-circulation cases (i.e., cases 1-8 in Table 2-4). Between  $0.5^\circ$  sampling and  $0.7^\circ$  sampling, the performance of  $0.5^\circ$  sampling is better than that of  $0.7^\circ$  sampling in 25% the cases. Between sine-space sampling and  $0.7^\circ$  sampling, the performance of sine-space sampling is better than that of  $0.7^\circ$  sampling in 20.8% of the cases. Between sine-space sampling and  $0.5^\circ$  sampling, the performance of  $0.5^\circ$  sampling is better than that of sine-space sampling in 16.7% of the cases. For the rest of the cases in each comparison, the two sampling grids perform the same. Overall, the denser grid in each comparison is the preferred grid because its performance matches or exceeds the performance of the coarser grid. This is reasonable because denser grids with more radials can be expected to better present the weather features.

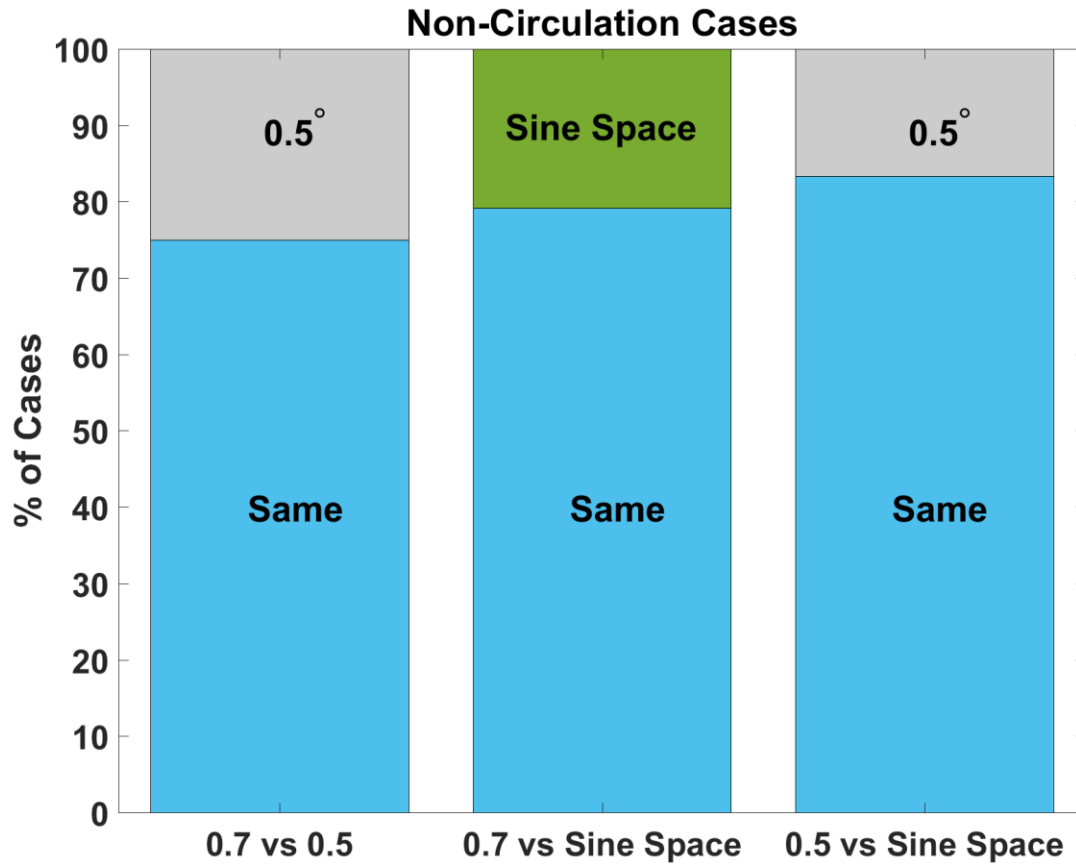


Fig. 3-7. Pair-wise comparison results between the three sampling grids for non-circulation cases.

Fig. 3-8 shows the results for the three comparisons for circulation cases (i.e., cases 9-16 in Table 2-4). Between  $0.5^\circ$  sampling and  $0.7^\circ$  sampling, the performance of  $0.5^\circ$  sampling is better in 70.8% the cases while the performance of  $0.7^\circ$  sampling is better in 29.2% of the cases. Between sine-space sampling and  $0.7^\circ$  sampling, the performance of sine-space sampling is better in 56.3% of the cases, the performance of  $0.7^\circ$  sampling is better in 27.1% of the cases, and their performances are the same in 16.7% of the cases. Between sine-space sampling and  $0.5^\circ$  sampling, the performance of  $0.5^\circ$  sampling is better in 29.2% of the cases, the performance of sine-space sampling is better in 20.8% of the cases, and their performances are the same in 50% of the cases.

These results indicate that there is no one preferred grid for sampling circulations, and the best performing sampling grid is case dependent (this is explored in the next section in more detail).

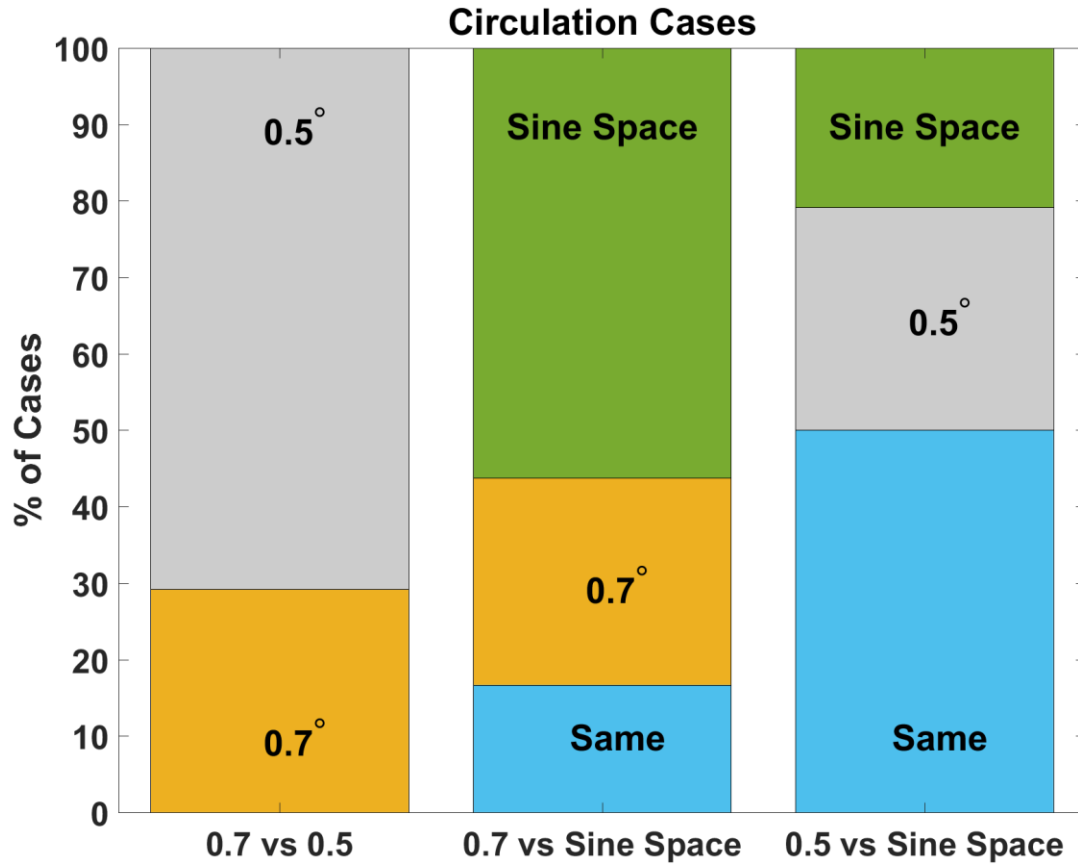


Fig. 3-8. Same as Fig. 3-7 except for circulation cases.

It is important to note that although subtle differences in the data allowed us to determine a better performing azimuthal sampling grid for some of the non-circulation cases, in none of these cases did any of the sampling grids cause distortions or artifacts in the data that could negatively impact forecasters' interpretation of the data or their assessment of the threat. For the circulation cases, we observed differences in the saliency and the radar-measured rotational velocities. These differences could impact tornado warning decisions. In the next section, we further investigate the azimuthal sampling effects on radar observation of circulations.

### 3.3. Azimuthal Sampling of Circulations

#### 3.3.1. Simulation Methodology

Our results in the previous section for circulation cases did not match either our expectations or previous results where reducing the azimuthal sampling interval can improve the detection of circulations. To further investigate the impact of azimuthal sampling on radar observation of circulations, we used a simplified simulator to quantify the performance of different sampling grids for a variety of circulations. This study differs from previous studies (e.g., Brown et al. 2002) by keeping the effective beamwidth constant to isolate the beamwidth effects from azimuthal sampling effects. While not as realistic as their physically based counterparts, simulations based on idealized circulation models have proven to be sufficient to study radar-sampling effects (e.g., Brown et al. 2002, Proud et al. 2009, Wood and Brown 2011, and Brown and Wood 2012).

In our simulations, we use the Rankine (1901) combined vortex model to generate the model velocity profile that cuts through the center of the circulation at a constant range. This model has the form

$$V(\theta) = V_x(R \tan \theta / R_x)^n \quad (3.1)$$

for a circulation at range  $R$  and centered at  $0^\circ$  azimuth, where  $V$  is the radial velocity at range  $R$  and azimuth  $\theta$ ,  $V_x$  is the maximum tangential velocity at core radius  $R_x$ ,  $n = 1$  for  $R \tan \theta \leq R_x$ , and  $n = -0.6$  for  $R \tan \theta > R_x$ . Fig. 3-9 shows an example of the model velocity profile (blue dashed line) as a function of azimuth where  $V_x$  is  $100 \text{ m s}^{-1}$ ,  $R_x$  is 400 m, and the range to the center of the circulation is 80 km. We tested other model velocity profiles as discussed in Wood and Brown (2011), and their results were similar to results from the Rankine model. However, the improvement to  $V_{rot}$  that can be gained via reducing the azimuthal sampling interval was smallest for the Rankine model, which means that the improvements shown in this study should be

conservative. We made three assumptions for the circulation model: 1) it has constant velocity in range; 2) it has constant velocity in elevation; and 3) it has uniform reflectivity everywhere. While somewhat unrealistic, these assumptions allow us to use simpler simulations without loss of generality.

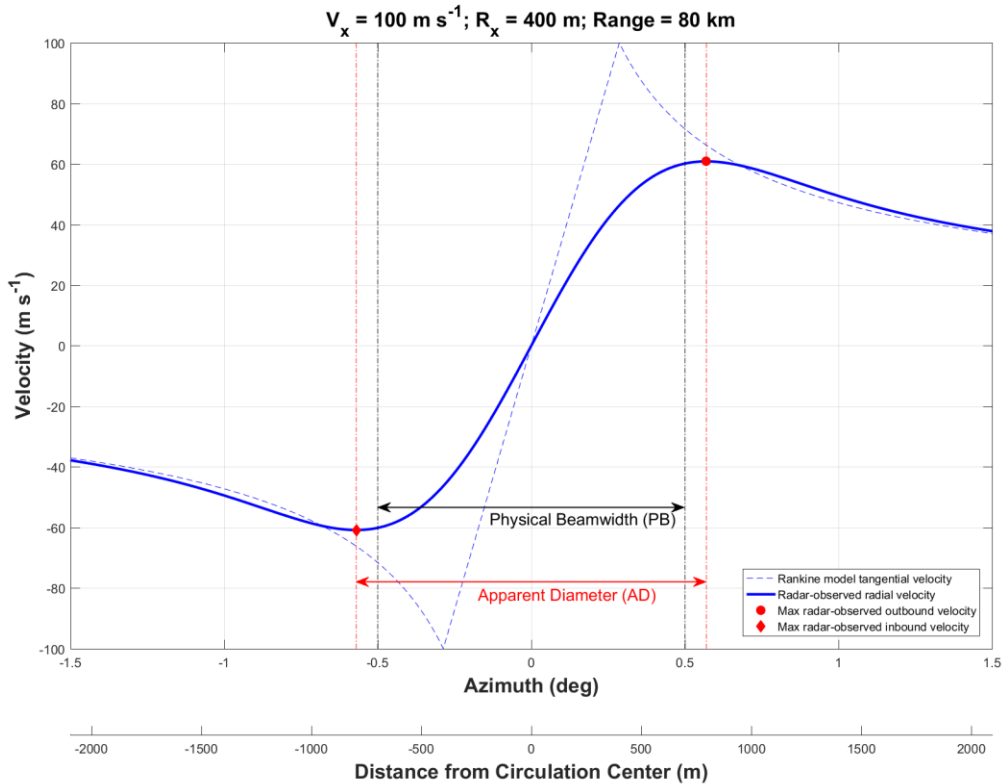


Fig. 3-9. Model (blue dashed line) and radar-observed (blue solid line) velocities (before sampling) as a function of azimuth for a circulation at a range of 80 km with  $100\text{-m s}^{-1}$  peak tangential velocity and 400-m core radius. The radar has a  $1^\circ$  effective beamwidth, which results in a physical beamwidth (PB) of  $\sim 1,396$  m at a range of 80 km. The extrema of the radar-observed velocities (red markers) are used to compute a  $V_{rot}$  of  $60.9\text{ m s}^{-1}$ , and their locations (vertical red dashed lines) are used to determine an apparent diameter (AD) of  $\sim 1,592$  m. The BADR for this circulation is 0.877.

To calculate the radar-observed velocity profile before sampling, a 1-dimensional effective antenna radiation pattern is convolved with the model velocity profile. The effective antenna radiation pattern is assumed to have a Gaussian-shaped main lobe. Similar to previous studies, the

sidelobes of the effective antenna radiation pattern are neglected since they are typically tens of dBs below the main lobe peak. In this study, we use an effective beamwidth of  $1^\circ$  because it approximates that of the Weather Surveillance Radar-1988 Doppler (WSR-88D) when collecting super-resolution data (Torres and Curtis 2007). The radar-observed velocity profile before sampling is shown in Fig. 3-9 with a solid blue line. Note that the maximum (red dot) and minimum (red diamond) of the radar-observed velocity profile have the same magnitude due to the symmetry of both the model and the effective antenna radiation pattern. This magnitude is defined as the maximum observable rotational velocity (denoted as  $V_{rot}^*$ ); that is, it is the maximum  $V_{rot}$  that can be observed by the radar for this circulation among all sampling grids when using a  $1^\circ$  effective beamwidth. Note that  $V_{rot}^*$  is less than  $V_x$  due to the “smoothing effect” of the effective antenna radiation pattern on the model velocity profile. In this case,  $V_{rot}^*$  is  $60.9 \text{ m s}^{-1}$  (recall that  $V_x$  is  $100 \text{ m s}^{-1}$ ). In our simulations, estimation noise is not added to the radar-observed velocities because its effects would be the same for all sampling grids, and we are only interested in assessing relative performance across all sampling grids.

In practice, simulations should take into account all possible combinations of circulation radii and distances from the radar. However, it is possible to reduce the number of circulations that need to be simulated by grouping circulations into families such that, for each member of a family, the impact of azimuthal sampling on the radar-observed strength of circulation is the same. One method to group the circulations into families is to use their beamwidth-to-apparent-diameter ratio (BADR), where the apparent diameter (AD) is defined as the distance between the extrema of the radar-observed velocity profile before sampling. In the example shown in Fig. 3-9, the physical size of the radar resolution volume in the azimuth dimension (herein referred to as the physical beamwidth or PB) at a range of 80 km can be computed to be  $\sim 1,396 \text{ m}$ , and the AD is  $\sim 1,592 \text{ m}$ ,

which results in a BADR of 0.877. Since PB broadens linearly as range increases, circulations that are farther away from the radar must have a larger AD to have the same BADR as circulations that are closer to the radar. For example, circulation A located at 160 km with  $V_x = 100 \text{ m s}^{-1}$  and  $R_x = 400 \text{ m}$  and circulation B located at 20 km with  $V_x = 50 \text{ m s}^{-1}$  and  $R_x = 50 \text{ m}$  have the same BADR of 1. The left panel of Fig. 3-10 shows the radar-observed velocities (before sampling) as a function of azimuth for these two circulations. Note that the extrema (indicated by the dot and diamond markers) of the radar-observed velocity profiles for these two circulations are located at the same azimuths, confirming that the two circulations have the same BADR. The radar-observed velocities before sampling can be expressed as a fraction of  $V_{rot}^*$ . This normalization removes the dependency on  $V_x$  and allows us to quantify the impact of azimuthal sampling for all cases with the same BADR using a single simulation. The normalized radar-observed velocity profiles for circulations A and B are shown in the right panel of Fig. 3-10. Since the two normalized curves are identical, the effects of azimuthal sampling for these two circulations are also identical. This implies that results for one circulation with a particular BADR can be generalized to other circulations with the same BADR.

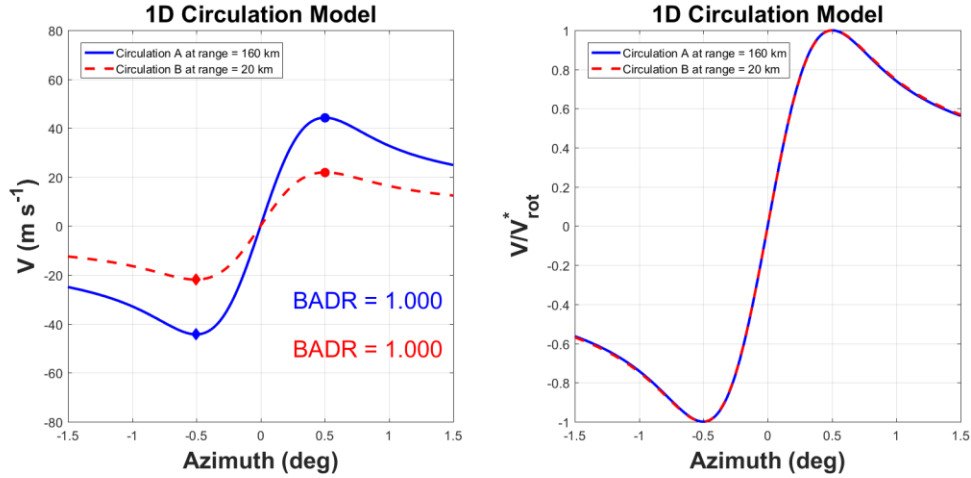


Fig. 3-10. Radar-observed velocities (before sampling) for circulation A (blue line) and B (red dashed line) for the 1-dimensional circulation model (left panel). Circulation A is located at 160 km with  $V_x = 100 \text{ m s}^{-1}$  and  $R_x = 400 \text{ m}$ , and circulation B is located at 20 km with  $V_x = 50 \text{ m s}^{-1}$  and  $R_x = 50 \text{ m}$ . Both circulations have the same BADR of 1, and their normalized radar-observed velocities are identical (right panel).

To evaluate the effects of azimuthal sampling on  $V_{rot}$ , we simulated four azimuthal sampling intervals:  $1.0^\circ$ ,  $0.5^\circ$ ,  $0.25^\circ$ , and  $0.125^\circ$ . For the same relative position, the grids are aligned such that a coarser sampling grid (i.e., one with a larger azimuthal sampling interval) is a subset of a denser one (i.e., one with a smaller azimuthal sampling interval). That is, a denser sampling grid retains all velocity samples from a coarser sampling grid and provides additional velocity samples at the new grid points. This implies that, compared to a coarser sampling grid,  $V_{rot}$  values for a denser sampling grid are always the same or closer to  $V_{rot}^*$ . For each circulation, the boundaries of the sampling grid are defined to ensure that the extrema of the radar-observed velocity profile are well within the sampling grid. Without loss of generality, we place the circulation center at  $0^\circ$  azimuth, and initially place the sampling grids such that the center grid point coincides with the center of the circulation. This position of the sampling grid relative to the center of the circulation is referred to as  $0^\circ$  sampling-grid relative position. In general, the sampling-grid relative position is defined as the minimum distance between the center of the

circulation (i.e.,  $0^\circ$  in our case) and the closest sampling-grid point. To study the effects of different sampling-grid relative positions, the grids are shifted by an azimuth offset varying from  $-0.5^\circ$  to  $0.5^\circ$  in  $0.005^\circ$  increments. These offsets span the full range of relative positions for the coarsest sampling grid with a  $1.0^\circ$  azimuthal sampling interval but result in multiple instances of the same sampling-grid relative position for the denser sampling grids (e.g., for a sampling grid with a  $0.25^\circ$  azimuthal sampling interval, azimuth offsets of  $0^\circ$ ,  $\pm 0.25^\circ$ , and  $\pm 0.5^\circ$  result in the same sampling-grid relative position of  $0^\circ$ ). In other words, the sampling-grid relative position, and consequently  $V_{rot}$ , are periodic functions of azimuth offset with period given by the azimuthal sampling interval. However, we apply the same azimuth offsets to all sampling grids (i.e., covering more than one period for the denser grids) to facilitate performance comparisons among different grids.

### 3.3.2. Simulation Results

Fig. 3-11 shows an example for circulations with a BADR of 0.833. The normalized radar-observed velocity profile (solid black line) and velocity samples corresponding to sampling grids with  $0.5^\circ$  (top panel) and  $0.25^\circ$  (bottom panel) azimuthal sampling intervals are shown. When the sampling-grid relative position is  $0^\circ$  (blue dots), reducing the azimuthal sampling interval from  $0.5^\circ$  to  $0.25^\circ$  does not change  $V_{rot}$ . Both sampling grids produce a normalized  $V_{rot}$  of 0.978. However, when the sampling-grid relative position is  $0.125^\circ$  (red diamonds), the grid with  $0.25^\circ$  azimuthal sampling interval produces a normalized  $V_{rot}$  of 0.999 while the grid with a  $0.5^\circ$  azimuthal sampling interval produces a normalized  $V_{rot}$  of 0.951. Note that for both relative positions, the grid with a  $0.25^\circ$  azimuthal sampling interval produces normalized values of  $V_{rot}$  that are the same or higher than those produced by a grid with a  $0.5^\circ$  azimuthal sampling interval, as expected. This example shows that a change in the relative position of the sampling grid may result in a higher normalized  $V_{rot}$  for a denser grid and a lower normalized  $V_{rot}$  for a coarser grid.

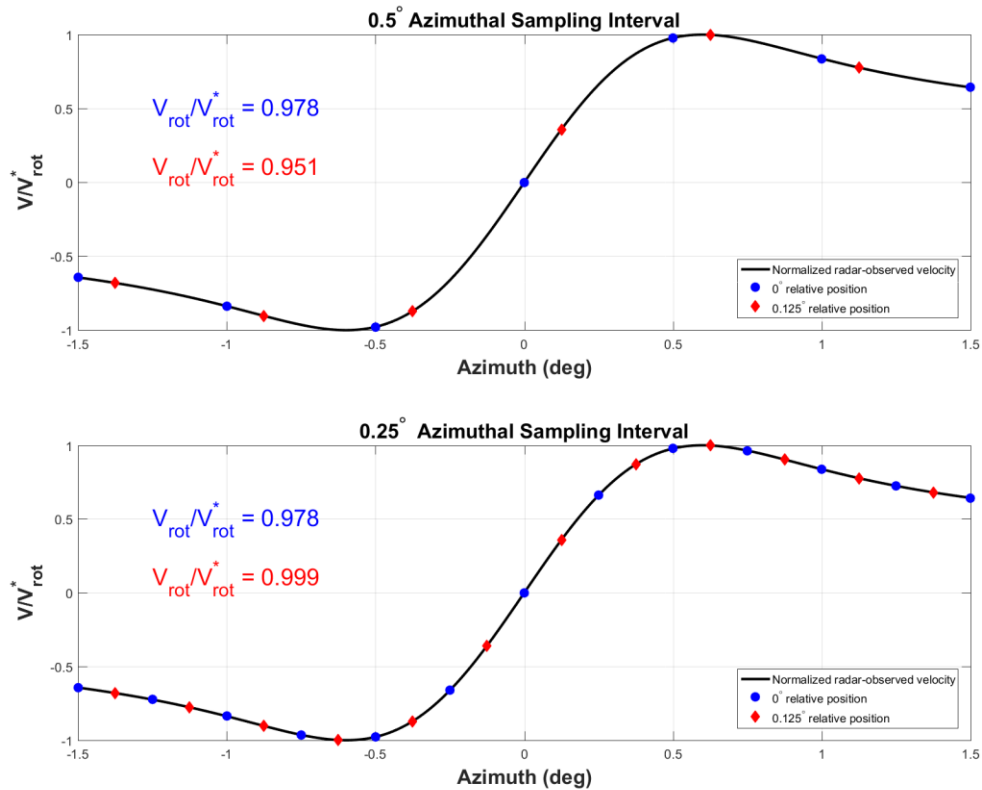


Fig. 3-11. Normalized radar-observed velocities before sampling (solid black lines) and velocity samples for grids with 0.5° (top panel) and 0.25° (bottom panel) azimuthal sampling intervals for a circulation with a BADR of 0.833. Velocity samples for 0° (blue dots) and 0.125° (red diamonds) relative positions are shown for both azimuthal sampling intervals.

For each BADR, there is a relationship between the relative position of the sampling grid and the normalized  $V_{rot}$ ; Fig. 3-12 shows an example of such a relationship for circulations with a BADR of 0.654. The normalized  $V_{rot}$  for grids with 1.0° (black line), 0.5° (blue line), 0.25° (red line), and 0.125° (green line) azimuthal sampling intervals are plotted for different azimuth offsets. As described before, the curves are periodic with period given by the azimuthal sampling interval. Fig. 3-12 also clearly shows that, for a given relative position, reducing the azimuthal sampling interval results in the same or higher normalized  $V_{rot}$ . The amount of improvement is largest when

the azimuthal sampling interval is reduced from  $1.0^\circ$  to  $0.5^\circ$ , and it gets progressively smaller as the azimuthal sampling interval is further reduced.

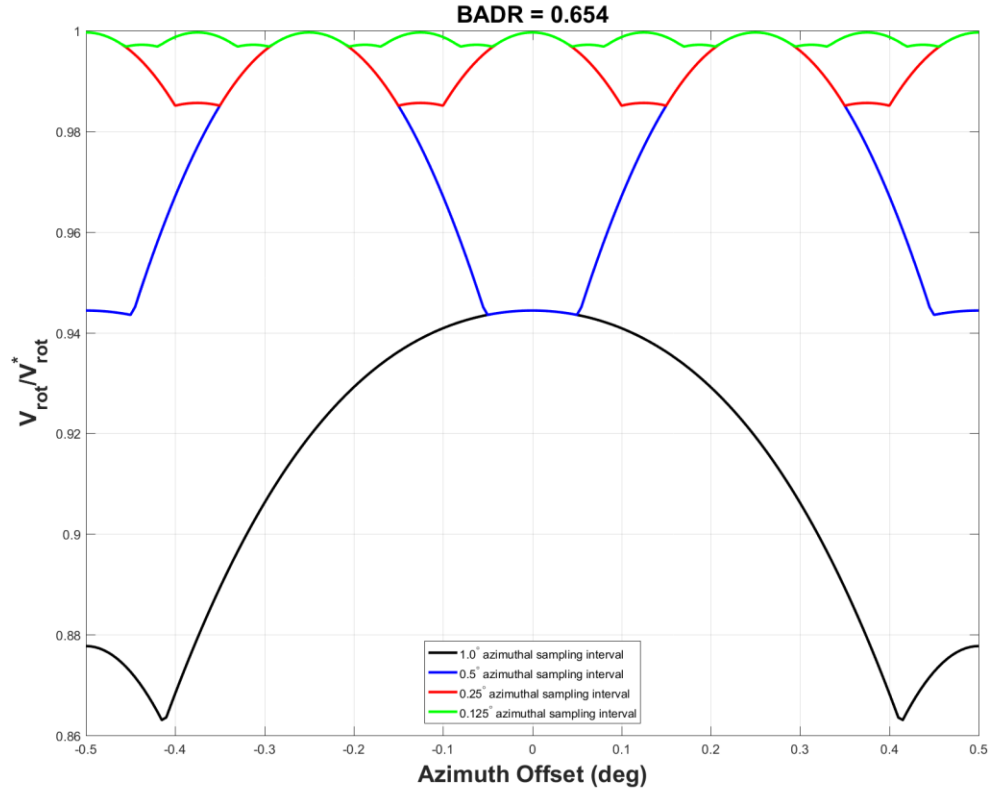


Fig. 3-12. Normalized  $V_{rot}$  as a function of sampling-grid azimuth offset for circulations with a BADR of 0.654. The different curves correspond to sampling grids with azimuthal sampling intervals of  $1.0^\circ$  (black),  $0.5^\circ$  (blue),  $0.25^\circ$  (red), and  $0.125^\circ$  (green).

Because in practice we do not know the sampling-grid relative position, it makes sense to measure the performance of different sampling grids independent of azimuth offset. For this purpose, we characterize the performance of each sampling grid for a given BADR using the best and worst  $V_{rot}$  among all possible relative positions (i.e., the maxima and the minima of curves like the ones in Fig. 3-12). Better performing sampling grids are those for which the worst  $V_{rot}$  is closer to  $V_{rot}^*$  thus reducing underestimation of radar-observed  $V_{rot}$ . From Fig. 3-12, it is clear that reducing the azimuthal sampling interval can improve the worst  $V_{rot}$  (i.e., the minima of each curve

increase as the azimuthal sampling interval decreases). Also, the difference between the best and worst  $V_{rot}$  decreases for the smaller azimuthal sampling intervals, which means that the sampling-grid relative position has less impact on measuring  $V_{rot}$ . In turn, this should help to improve the interpretation of radar data because any short-term variations in observed circulation strength can be mostly attributed to storm evolution and not to radar sampling.

The example shown in Fig. 3-12 demonstrates the advantages of reducing the azimuthal sampling interval for a single BADR. To generalize our results, we conducted a similar analysis for BADRs varying from 0.1 to 1.06. This interval covers a range including large circulations close to the radar (e.g.,  $R_x = 400$  m and range of 4.6 km) to small circulations far from the radar (e.g.,  $R_x = 50$  m and range of 114.6 km). Fig. 3-13 shows the best  $V_{rot}$  (solid lines) and worst  $V_{rot}$  (dashed lines) for different azimuthal sampling intervals as a function of BADR. It can be seen from this figure that the best  $V_{rot}$  (solid line) equals  $V_{rot}^*$  for only a few combinations of azimuthal sampling interval and BADR. In all other cases, even the best  $V_{rot}$  is underestimated regardless of the sampling-grid relative position. However, for all BADRs, the best and worst  $V_{rot}$  values get closer to  $V_{rot}^*$  as the azimuthal sampling interval is reduced. For grids with azimuthal sampling intervals of  $1.0^\circ$ ,  $0.5^\circ$ ,  $0.25^\circ$ , and  $0.125^\circ$ , the best normalized  $V_{rot}$  values are greater than or equal to 0.917, 0.971, 0.991, and 0.997, respectively, and the worst normalized  $V_{rot}$  values are greater than or equal to 0.699, 0.854, 0.956, and 0.990, respectively. This confirms that, for all BADRs, the underestimation of radar-observed  $V_{rot}$  is reduced for the finer sampling grids.

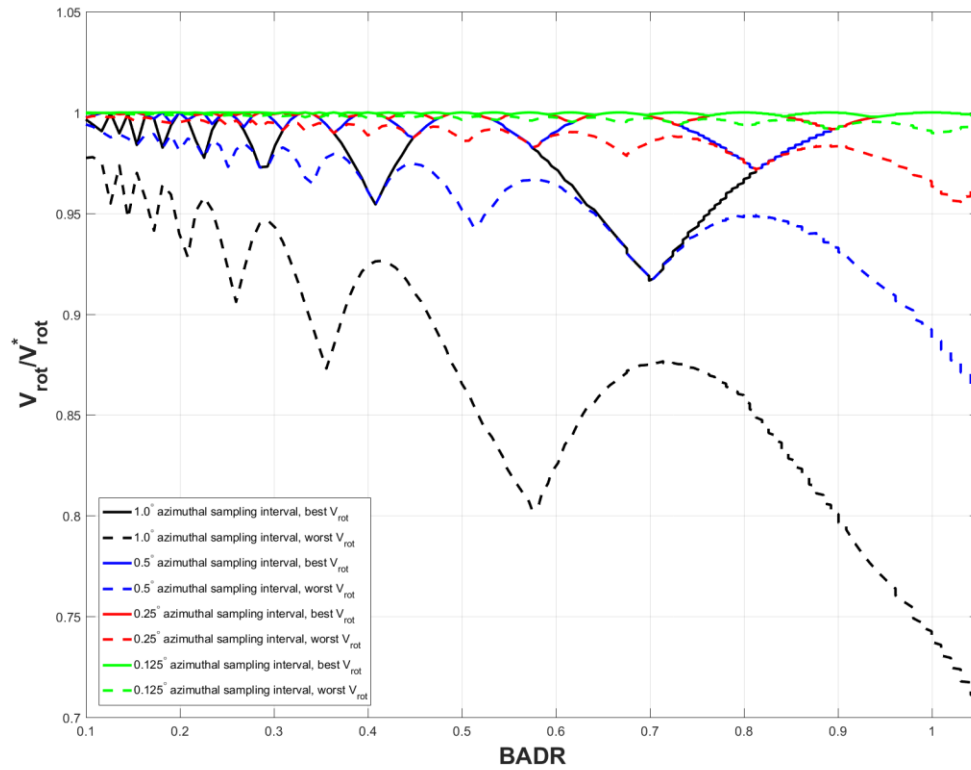


Fig. 3-13. The best (solid lines) and worst (dashed lines)  $V_{rot}$  for each sampling grid among all possible relative positions for different BADRs. The different curves correspond to sampling grids with azimuthal sampling intervals of  $1.0^\circ$  (black),  $0.5^\circ$  (blue),  $0.25^\circ$  (red), and  $0.125^\circ$  (green).

Fig. 3-13 also shows that, for all BADRs, the differences between the best and worst  $V_{rot}$  for each sampling grid are also reduced when the azimuthal sampling interval is reduced. Among the simulated BADRs, the maximum difference between the best and worst normalized  $V_{rot}$  for grids with azimuthal sampling intervals of  $1.0^\circ$ ,  $0.5^\circ$ ,  $0.25^\circ$ , and  $0.125^\circ$  are 0.298, 0.143, 0.044, and 0.010, respectively. This confirms that reducing the azimuthal sampling interval results in more consistent radar-observed  $V_{rot}$  values that are independent of sampling-grid relative positions for all BADRs. Thus, for all circulations, the impact of sampling-grid relative position is reduced when using denser sampling grids. However, the improvements get progressively smaller as the azimuthal sampling interval decreases. That is, reducing the azimuthal sampling interval from  $1.0^\circ$

to  $0.5^\circ$  has the largest improvement while reducing the azimuthal sampling interval from  $0.25^\circ$  to  $0.125^\circ$  has the smallest improvement. A previous study by Melnikov et al. (2015) proposed to use the densest sampling grid possible for the WSR-88D to improve radar observation of circulations. Our results show that the majority of the benefits of decreasing the azimuthal sampling interval are realized for azimuthal sampling intervals on the order of  $0.125^\circ$ . Note that for the sampling grids in our simulations, the computational complexity is doubled as the azimuthal sampling interval is halved (i.e., estimates must be produced for twice the number of sampling grid points). In practice, any increase in computational complexity must be considered when choosing the appropriate sampling grid.

### 3.3.3. Real Data

In this section, we corroborate our simulation results using real data. To mimic our simulation experiments, we processed time-series (I/Q) data for two cases to produce velocity fields corresponding to different sampling grids. For each sampling grid, we measured the radar-observed  $V_{rot}$  and produced a plot similar to Fig. 3-12. These data were collected using constant elevation scans where each transmit pulse corresponds to a different azimuth angle, and the azimuth difference between consecutive pulses is given by the product of the antenna rotation rate and the PRT. To generate velocity fields, dwells were formed by taking the returns from the same number of transmit pulses ( $M$ ) centered in azimuth about each sampling grid point. This process is illustrated in Fig. 3-14 for  $M = 20$  and 3 sampling grids. In this figure, each box on the top axis (labeled as pulses) represents the received I/Q data for all range cells corresponding to a single transmitted pulse. Grids A and B have a  $1.0^\circ$  azimuthal sampling interval while Grid C has a  $0.5^\circ$  azimuthal sampling interval. The grid points are indicated by the colored dots, and the I/Q data used to form the corresponding dwells are indicated by the line segments with matching colors.

Note that because  $M$  is kept constant for all sampling grids, adjacent dwells are increasingly overlapped as the sampling grid gets finer (e.g., compare Grid A to Grid C in Fig. 3-14). All dwells were processed using the same data window to maintain a constant effective beamwidth of  $\sim 1.0^\circ$ ; this also ensures that the standard deviation of velocity estimates is consistent across different sampling grids. Velocities for each range cell were estimated using the conventional pulse-pair estimator and were manually dealiased and converted to storm-relative velocity to facilitate the measurement of  $V_{rot}$ . The dealiasing process consists of three basic steps. First, we identified the general area of the circulation by examining the reflectivity and velocity fields. Next, within this general area, we determined the approximate center of the circulation by looking for the largest azimuthal shear at constant range, which can be over 2 or 3 range cells depending on the BADR and the sampling grid. Finally, the velocities of neighboring range cells were dealiased using knowledge of the expected wind direction (inbound or outbound) from non-aliased velocities in range gates farther away from the center of the circulation. To introduce the effects of different sampling-grid relative positions, this process was repeated as each sampling grid was progressively shifted in azimuth from  $-0.5^\circ$  to  $0.5^\circ$  in  $0.02^\circ$  increments. In the examples shown in Fig. 3-14, Grid A has a  $0^\circ$  azimuth shift, Grid B has a  $0.5^\circ$  azimuth shift, and Grid C has a  $0^\circ$  azimuth shift (as explained in the previous section, this shift is equivalent to a  $-0.5^\circ$  or  $0.5^\circ$  azimuth shift for this azimuthal sampling interval).

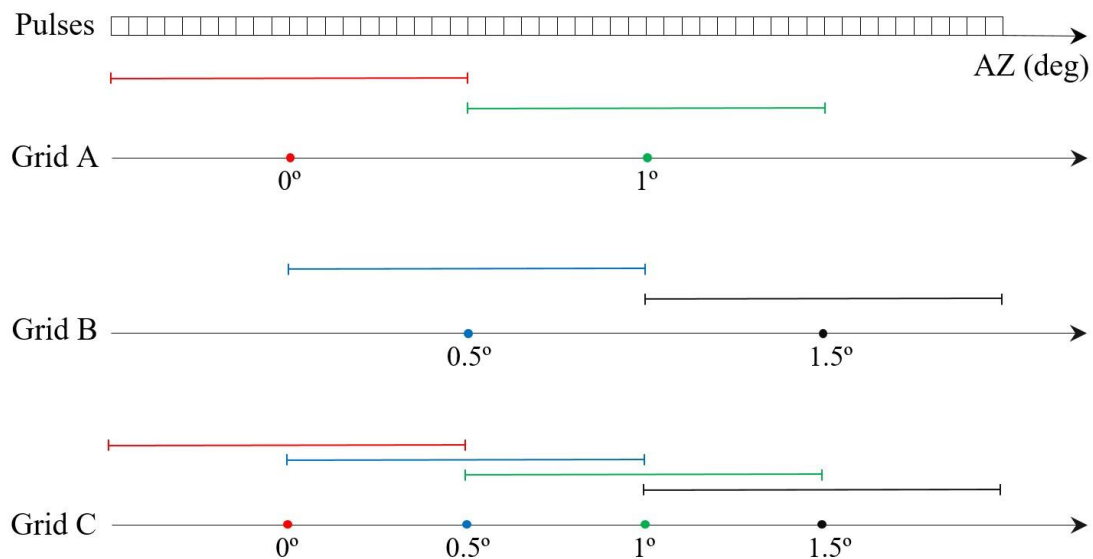


Fig. 3-14. Illustration of how dwells were formed for different sampling grids. The received I/Q data for all range cells corresponding to a single transmitted pulse are represented by the boxes in the top axis. The grid points are indicated by the colored dots, and the group of pulses used to form the dwell corresponding to a grid point is indicated by the line segment with matching color.

The first case we used to corroborate our simulation results is a circulation observed by the KCRI radar located in Norman, OK on 19 May 2013 at 22:04Z. At the time of observation, the circulation was located at  $31.5^\circ$  in azimuth and 42 km in range. Fig. 3-15 shows the storm-relative velocity (SRM) fields of the circulation at  $0.5^\circ$  elevation corresponding to grids with  $0^\circ$  azimuth shift and azimuthal sampling intervals of  $1.0^\circ$  (top left panel),  $0.5^\circ$  (top right panel),  $0.25^\circ$  (bottom left panel), and  $0.125^\circ$  (bottom right panel). The location and magnitude of the maximum inbound and outbound velocities used to calculate  $V_{rot}$  are indicated by the arrows in each panel. The grid with a  $1.0^\circ$  azimuthal sampling interval produced the lowest  $V_{rot}$  of  $27.0 \text{ m s}^{-1}$ , while the grids with  $0.5^\circ$ ,  $0.25^\circ$ , and  $0.125^\circ$  azimuthal sampling intervals produced higher values of  $V_{rot}$  of  $44.45 \text{ m s}^{-1}$ ,  $50.25 \text{ m s}^{-1}$ , and  $50.25 \text{ m s}^{-1}$ , respectively. Note that, in this case, reducing the azimuthal sampling interval from  $0.25^\circ$  to  $0.125^\circ$  does not result in higher  $V_{rot}$ . This example corroborates our

simulation findings: reducing the azimuthal sampling interval can result in the same or higher  $V_{rot}$ , and the improvements get progressively smaller as the azimuthal sampling interval decreases.

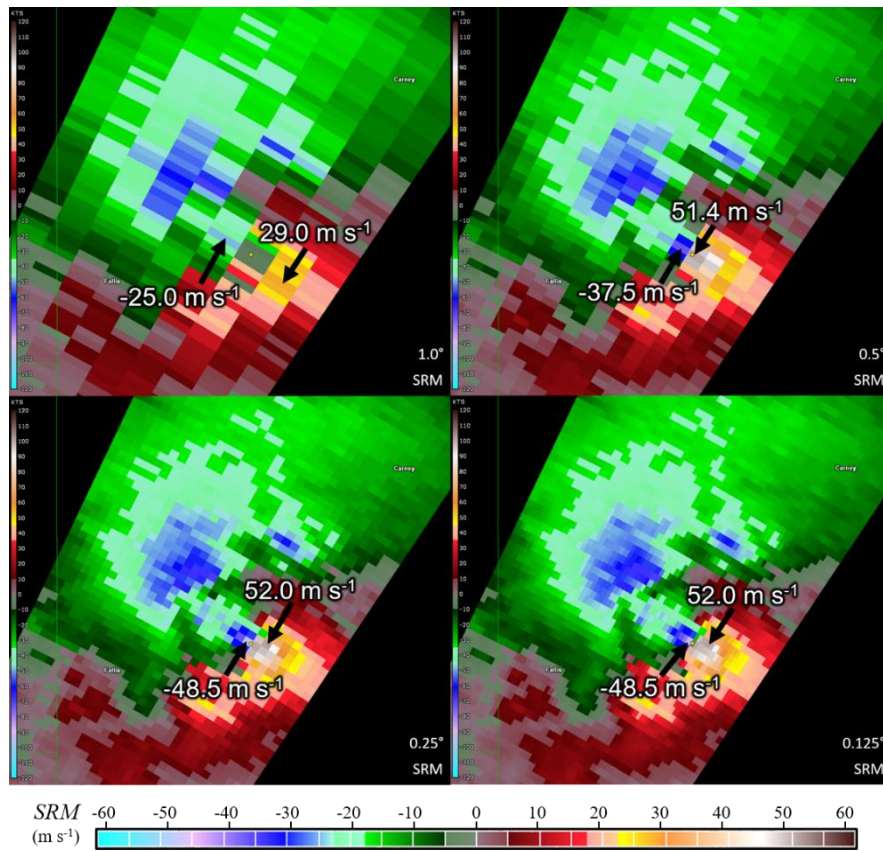


Fig. 3-15. Storm-relative velocity (SRM) fields at  $0.5^\circ$  elevation for a circulation located at  $31.5^\circ$  in azimuth and 42 km in range observed by the KCRI radar on 19 May 2013 at 22:04Z. The same time-series data were processed to generate fields corresponding to four sampling grids with  $0^\circ$  azimuth shift and azimuthal sampling intervals of  $1.0^\circ$  (top left),  $0.5^\circ$  (top right),  $0.25^\circ$  (bottom left), and  $0.125^\circ$  (bottom right). The location and magnitude of the maximum inbound and outbound velocities used to calculate  $V_{rot}$  are shown by the arrows.

Fig. 3-16 shows the SRM fields at  $0.5^\circ$  elevation for sampling grids shifted by  $0^\circ$  (left column),  $0.16^\circ$  (middle column), and  $0.28^\circ$  (right column), and Table 3-1 contains the values of  $V_{rot}$  for each case. As expected, the relative position of the grid affects  $V_{rot}$  (i.e., the values of  $V_{rot}$  vary within each row of Table 3-1). However, the variability reduces as the azimuthal sampling interval gets smaller (i.e., the values of  $V_{rot}$  within each row of Table 3-1 are more consistent as we move from top to bottom). Moreover, for each azimuth shift, denser grids resulted in the same

or higher  $V_{rot}$  when compared to coarser grids (i.e.,  $V_{rot}$  is the same or increases as we go down each column of Table 3-1). These results also corroborate our observations from Fig. 3-12.

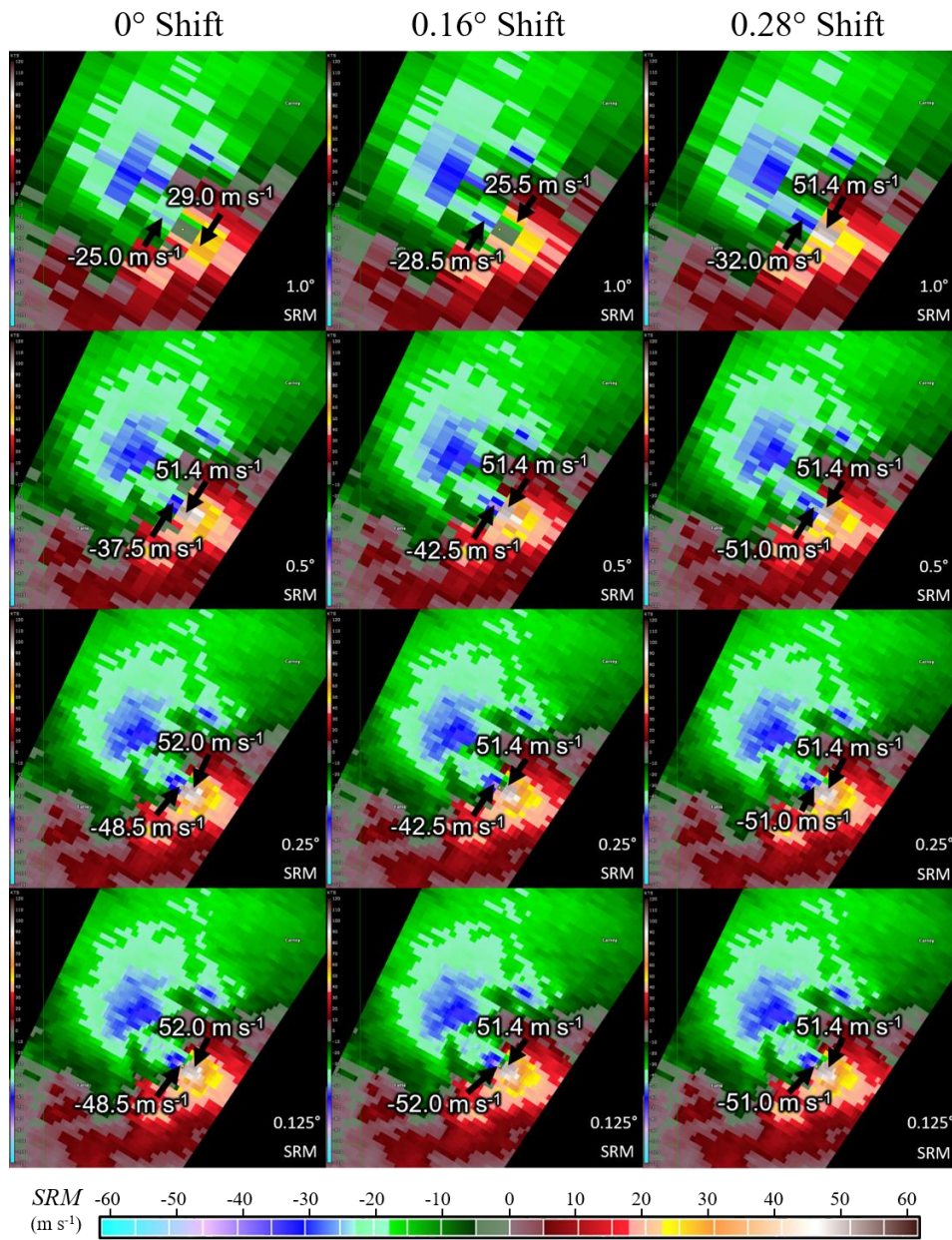


Fig. 3-16. Same as Fig. 3-15 except for sampling grids shifted by 0° (left column), 0.16° (middle column), and 0.28° (right column). The values of  $V_{rot}$  for each case are listed in Table 3-1.

Table 3-1. Computed  $V_{rot}$  for each case in Fig. 3-16.

Azimuthal Sampling Interval	0° Shift	0.16° Shift	0.28° Shift
1.0°	27.0 m s <sup>-1</sup>	27.0 m s <sup>-1</sup>	41.7 m s <sup>-1</sup>
0.5°	44.45 m s <sup>-1</sup>	46.95 m s <sup>-1</sup>	51.2 m s <sup>-1</sup>
0.25°	50.25 m s <sup>-1</sup>	46.95 m s <sup>-1</sup>	51.2 m s <sup>-1</sup>
0.125°	50.25 m s <sup>-1</sup>	51.7 m s <sup>-1</sup>	51.2 m s <sup>-1</sup>

Fig. 3-17 summarizes the results for all sampling grids applied to this case. Similar to what is presented in Fig. 3-12 using simulations,  $V_{rot}$  was computed from velocity fields obtained from the real data and plotted as a function of azimuth shift for grids with different azimuthal sampling intervals. Whereas the manual dealiasing process used so far is quite realistic, it may not be perfect, especially for large BADRs. That is, for weaker or more distant circulations, identifying the approximate location of the center of the circulation can be challenging, and this could lead to velocity dealiasing errors. In turn, any dealiasing errors could result in underestimation of  $V_{rot}$ , especially for the coarser grids. Ideally, we would want to reduce velocity-dealiasing errors to compare the coarser grids to the denser ones in a fair manner. This is also important when comparing the real-data results with those in Fig. 3-12 because the simulations did not include aliasing effects. For this analysis, we used the velocity field corresponding to the 0.125° azimuthal sampling interval with the same azimuth shift to inform the dealiasing of coarser-grid velocity fields. Note, however, that this process is not realistic because, in practice, velocity fields on multiple sampling grids are not available. As a consequence of reducing velocity dealiasing errors, the values of  $V_{rot}$  for grids with a 1.0° azimuthal sampling interval are now higher than those listed in Table 3-1. The curves in Fig. 3-17 broadly agree with the simulation results in Fig. 3-12. That is, reducing the azimuthal sampling interval results in the same or higher  $V_{rot}$  for the same

sampling-grid relative position and in improved consistency when considering all relative positions.

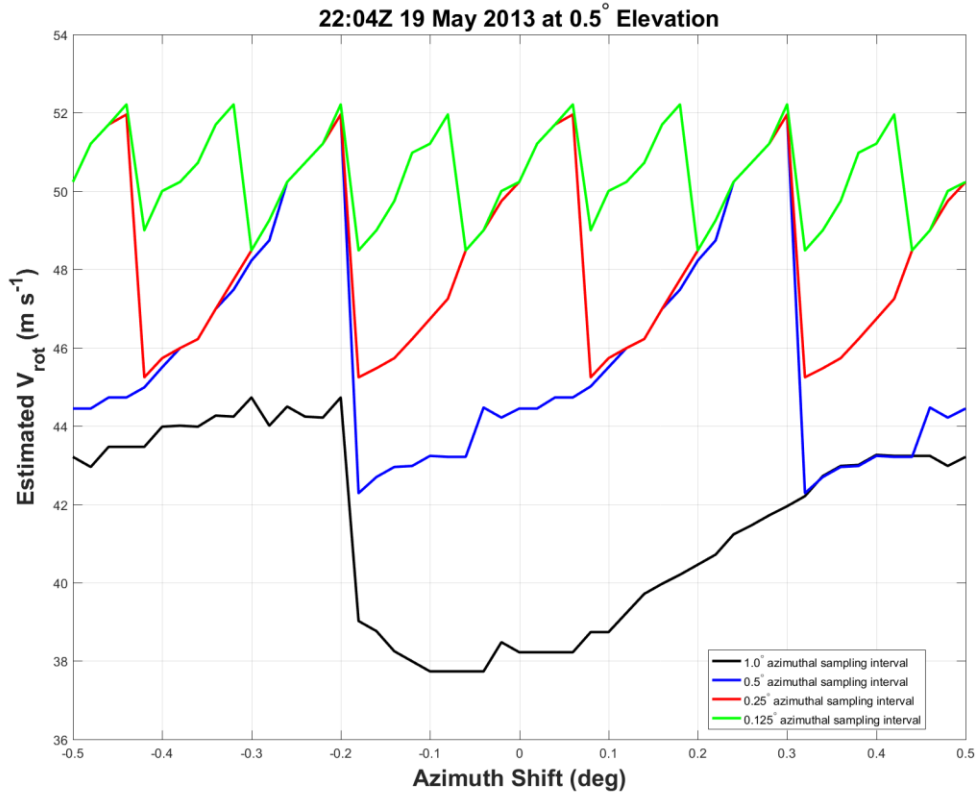


Fig. 3-17.  $V_{rot}$  as a function of azimuth shift for different sampling grids for the circulation observed on 19 May 2013 at 22:04Z. The different curves correspond to sampling grids with azimuthal sampling intervals of 1.0° (black), 0.5° (blue), 0.25° (red), and 0.125° (green).

While there is broad agreement between the results from simulations and real data, there are also some noticeable differences. One obvious difference is that the real-data curves shown in Fig. 3-17 are not symmetrical about 0° azimuth shift because this shift does not correspond to 0° relative position as was the case with the simulations. Additionally, the curves are not symmetrical about their maxima; this could be caused by errors in the estimated storm motion or asymmetry in the circulation itself. Also note that, in the real data, improvement from coarser to denser grids does not follow the same pattern. While the best  $V_{rot}$  values for sampling grids with 0.5°, 0.25°, 0.125°

and  $0.125^\circ$  azimuthal sampling intervals are about the same, the worst  $V_{rot}$  values do not improve at the same pace as seen with simulations. For example, the minima of the red curve are closer to the minima of the blue curve whereas simulations showed the opposite (i.e., the minima of the red curve were closer to the minima of the green curve). This discrepancy could be caused by statistical errors of velocity estimates. Nevertheless, none of these differences observed in the real-data results change the main conclusion derived from simulation results: reducing the azimuthal sampling interval improves the accuracy of radar-observed circulation strength.

The second case we used to corroborate our simulation results is a circulation observed by the KOUN radar located in Norman, OK on 9 May 2016 at 21:05Z. At the time of observation, the circulation was located at  $171^\circ$  in azimuth and 46.6 km in range. The same analyses were performed for this case as in the previous case, and the results are shown in Fig. 3-18. Compared to the previous case, the circulation in this case has a larger BADR. Because of this, identifying the approximate circulation center to perform accurate velocity dealiasing and then compute  $V_{rot}$  is more challenging. Despite the curves exhibiting noisier behavior compared to those in Fig. 3-17, grids with smaller azimuthal sampling interval still result in the same or higher  $V_{rot}$  for a given relative position and in improved consistency when considering all relative positions.

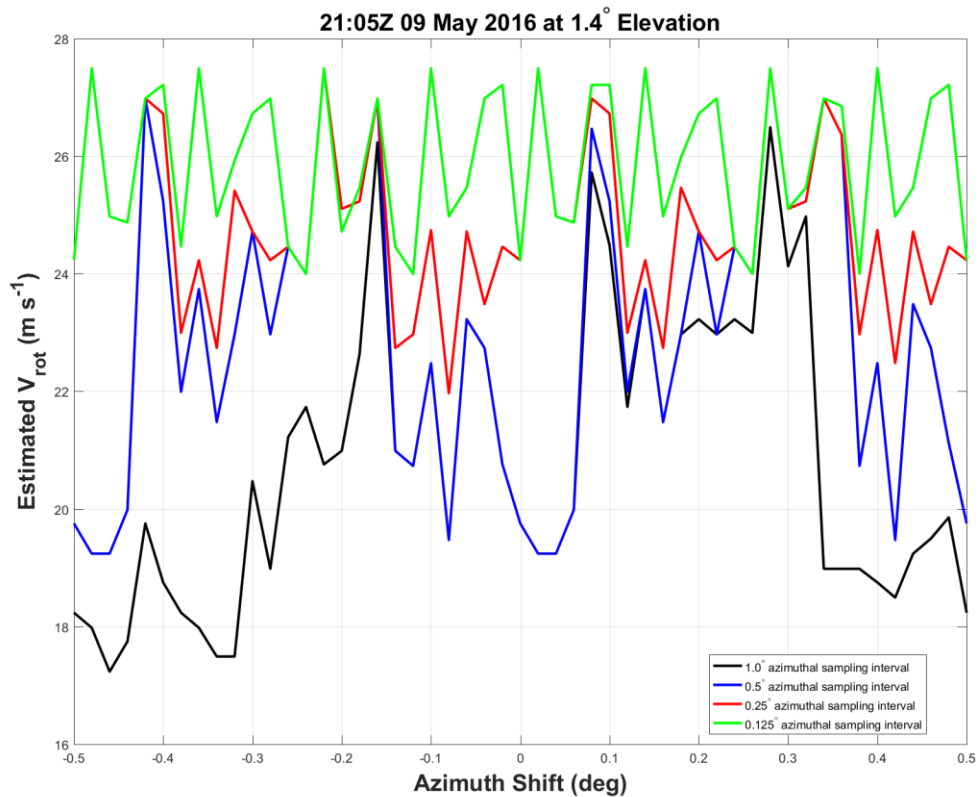


Fig. 3-18. Same as Fig. 3-17 except for the circulation observed on 9 May 2016 21:05Z.

### 3.4. Conclusions

In this section, we investigated the potential impacts of changing the azimuthal sampling grid on forecasters. We compared simulated data from the scaled PAR for the same weather event collected with three different azimuthal sampling intervals. For non-circulation cases, we found that a denser sampling grid is always preferred. For circulation cases, the preferred sampling grid is case dependent. In all the cases analyzed, using sine-space sampling does not cause any artifacts in the radar data that can negatively impact forecasters' data interpretation and threat assessment.

To further study the azimuthal sampling effects on radar observations of circulations, we used a simplified model to quantify the performance of different sampling grids. Our simulation

results showed that decreasing the azimuthal sampling interval leads to a reduction in the underestimation of the  $V_{rot}$  for all BADRs. Our simulations also showed that, for all BADRs, grids with a  $0.125^\circ$  ( $0.25^\circ$ ) azimuthal sampling interval result in radar-observed circulation strengths that are within 99% (95%) of their theoretical maxima. Moreover, decreasing the azimuthal sampling interval also reduces the impacts of azimuthal sampling for all BADRs. That is, the difference between the best and the worst radar-observed circulation strengths among all sampling-grid relative positions decreases as the azimuthal sampling interval gets smaller. To corroborate our simulation results, we processed time-series data for two circulations and produced velocity fields corresponding to different sampling grids. The variation of  $V_{rot}$  as a function of azimuth shift for different sampling grids showed the same features as the simulation results. That is, higher and more consistent radar-observed circulation strengths were measured when using sampling grids with smaller azimuthal sampling interval. Results from simulations and real data also showed that the improvements get progressively smaller as the azimuthal sampling interval decreases, which implies that the majority of the benefits can be realized without using the finest possible sampling grid.

## **4. Impact of Sensitivity**

### **4.1 Introduction**

Weather radars not only need to detect strong echoes corresponding to precipitation, they must also be able to detect weak echoes that have meteorological significance. Sensitivity is the parameter that describes the minimum detectable signal of the radar. For the polarimetric WSR-88D, the sensitivity specification requires the radar to produce a signal-to-noise ratio (SNR) of at least 0 dB for a -8.5 dBZ target at 50 km while operating in simultaneous transmission mode. If the antenna pattern and the range weighting function are kept constant, the radar sensitivity is directly proportional to the total transmitted power and inversely proportional to the system noise power. That is, increasing the radar transmit power or decreasing the system noise power can increase the sensitivity. Sensitivity is a cost driver for most radar systems. In the context of a PAR, increasing the total transmit power requires either using more powerful amplifiers for each radiating element or utilizing pulse compression techniques. While the first option could increase system cost due to the price of the electronic components, the second option could increase the system cost by using more bandwidth in the spectrum. Pulse compression also has other disadvantages (e.g., range sidelobes and blind ranges) that need to be mitigated for weather radar applications. Decreasing the system noise power could also increase system cost because it would require more expensive low-noise electronic components in the receive chain. Therefore, it is important for decision makers to understand the operational impacts on forecasters when the sensitivity of the radar is changed so they can balance system performance and cost.

In this study, we use the SPARC simulator to simulate data of the same weather event as observed by weather radars with progressively decreased sensitivity. The simulated data are evaluated and scored using a scoring system similar to the system described in section 2.2.2.

However, the main criteria used for analysis in this study are the erosions of the storm area and weather features of interest. We then fit curves to our scoring results using a process similar to that described in section 2.2.3. The average best-fit curve can be used by decision makers to evaluate the operational impact on possible future radar designs by comparing their sensitivity to the sensitivity of the WSR-88D.

## **4.2 Simulation Methodology**

The SPARC simulator is well suited to study the impact on forecasters of changing sensitivity. As described in section 2.2.1, the simulator ingests archived WSR-88D data and simulates time-series data for scattering centers that can be weighted and summed to generate time-series data at a desired azimuth, elevation, and range. The sensitivity of the WSR-88D sets a lower bound on the sensitivity of the radar system we can simulate because all signals with SNR below the censoring thresholds for the WSR-88D are lost in the archived data. Therefore, we can only simulate radar systems with sensitivity worse than the WSR-88D. This is accomplished by first simulating time-series data that correspond the WSR-88D radar by setting the scattering center weights to be a delta function. That is, a weight of 1 for the scattering center with the same azimuth, elevation, and range as the desired range cell and 0 for all other scattering centers. This ensures that the antenna pattern and range weighting function of the simulated radar systems are identical to that of the WSR-88D. We then add simulated white-noise time-series data to the weather time-series data to simulate radar data for systems with decreased sensitivity. The noise power is progressively increased to simulate data with SNR losses ranging from 0 to 20 dB in 2 dB increments. Note that the same weather time-series data for each case are used throughout this process to ensure that observed differences in data quality are caused by the loss of sensitivity and are not caused by random fluctuations between different realizations of the weather time-series data. Since all other

parameters (e.g., antenna pattern, range weighting function, transmitted power, pulse length, etc.) of the simulated radar systems are identical, the simulated SNR loss has a one-to-one relationship to sensitivity loss. That is, a simulated 2 dB SNR loss corresponds to a radar system with sensitivity that is 2 dB lower than that of the WSR-88D.

### **4.3 Case Selection and Data Analysis Processes**

Sensitivity of the radar impacts observations of weather features where the backscattered signal power is low compared to the system noise power. The backscattered signal power depends mainly on the transmitted power, on the radar wavelength, and on the location, type, number, and size of hydrometeors. It also depends on the targets present along the radar beam; these can attenuate and even completely extinguish the transmitted waves. For the WSR-88D, a few situations can be identified that typically result in weak radar returns and are therefore impacted the most by a potential sensitivity loss. For winter weather events, the size (also referred to as footprint) of each storm on the PPI plot is usually directly impacted by sensitivity loss. In convective events, the key impacts of sensitivity loss are the detections of outflow boundaries and potential circulations associated with low-precipitation supercells. In low-precipitation supercells, distinguishing a tornado debris signature from clear air returns in the inflow region can become more challenging as sensitivity decreases. The cases used in this study are listed in Table 4-1, where Case 1 and 7 are convective events and the other cases are winter events. Because sensitivity loss is progressive, a 5-level scoring system is used to quantify the impact on forecasters. However, the criteria used in this scoring system are different from the scoring system described in section 2.2.2. While sensitivity loss is unlikely to generate distractions that require forecasters to expend additional cognitive resources to diagnose, it does lead to the loss of weak echoes, which may erode the presentation of important weather features. In the scoring system we used for this study, a score

of 1 indicates fully acceptable data quality with no or trivial data loss; a score of 2 indicates acceptable data quality with minimal data loss; a score of 3 indicates ambiguous data quality where data loss has marginal impact on the presentation of significant features; a score of 4 indicates unacceptable data quality where data loss partially erodes the presentation of important weather features; and a score of 5 indicates completely unacceptable data quality where data loss significantly erodes the presentation of important weather features.

Table 4-1. Selected weather cases to evaluate impacts of degraded sensitivity on forecasters' data interpretation process.

Case Number	Date and Radar
1	18:33Z 22 July 2017, KLWX
2	22:40Z 04 March 2015, KLVX
3	20:39Z 18 November 2014, KBUF (4.57 $\mu$ s pulse)
4	12:11Z 19 November 2014, KBUF (1.57 $\mu$ s pulse)
5	11:08Z 04 January 2017, KGRR
6	03:29Z 22 January 2015, KAMA
7	22:19Z 23 May 2015, KTLX
8	14:57Z 25 December KGYX

To demonstrate our scoring system and analysis process, Fig 4-1 to 4-5 show simulated data for Case 6 in Table 4-1. This case is a heavy snow event where the snow rate is about 10 cm per hour at the surface for the chosen time step. The key weather features are the ring of slightly higher differential reflectivity and slightly lower correlation coefficient aloft (indicated by the arrows in Fig. 4-1). These features are associated with the dendritic growth layer and indicate that heavy snow will continue at the surface. As the sensitivity decreases, the footprint of the storm also decreases, eventually eroding the key weather features. Fig. 4-1 shows reflectivity (top right), Doppler velocity (top right), differential reflectivity (bottom left), and correlation coefficient (bottom right) from simulated data with no sensitivity loss (the same sensitivity as the WSR-88D), where the data quality matches that of the WSR-88D. Since there is no loss of data, these data are

scored as a 1. Fig. 4-2 shows simulated data with a 4-dB sensitivity loss. Compared to Fig. 4-1, there is slight loss of data around the edges of the storm. However, this slight decrease in footprint does not impact the key weather features at all. Therefore, these data are scored as a 2. Fig. 4-3 shows simulated data with a 10-dB sensitivity loss. In this case, the differential reflectivity layers above the dendritic growth layer begin to erode. Additionally, part of the correlation coefficient layer above the dendritic growth layer is eroded. Therefore, these data are scored as a 3. Fig 4-4 shows simulated data with a 14-dB sensitivity loss. Here, parts of the differential reflectivity layer and the correlation coefficient layer above the dendritic growth layer are eroded. Since these data contain major data losses, they are scored as a 4. Finally, Fig. 4-5 shows simulated data with a 20-dB sensitivity loss, where part of the dendritic growth layer is eroded. Since data loss of the key weather feature occurred, these data are scored as a 5.

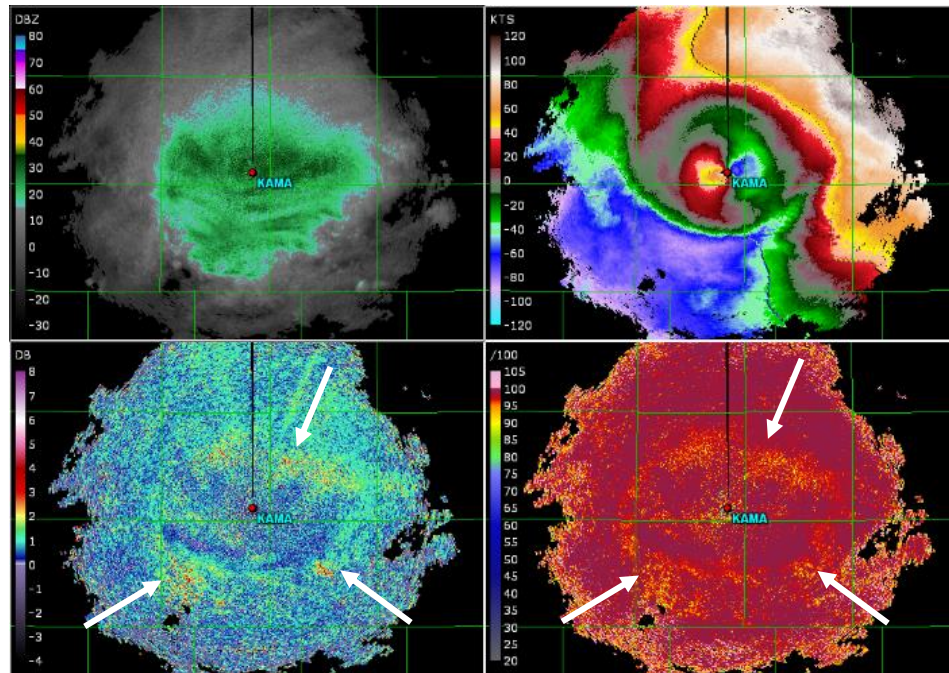


Fig. 4-1. Reflectivity (top left), Doppler velocity (top right), differential reflectivity (bottom left), and correlation coefficient (bottom right) for Case 6. These data have no sensitivity loss and are scored as a 1.

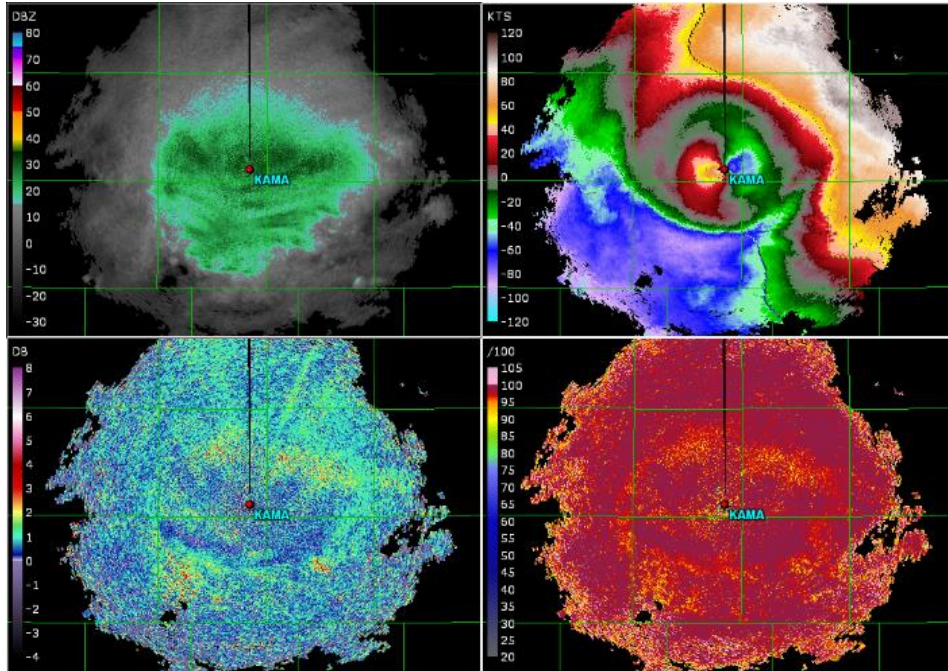


Fig. 4-2. Same as Fig. 4-1 except with a 4-dB sensitivity loss and are scored as a 2.

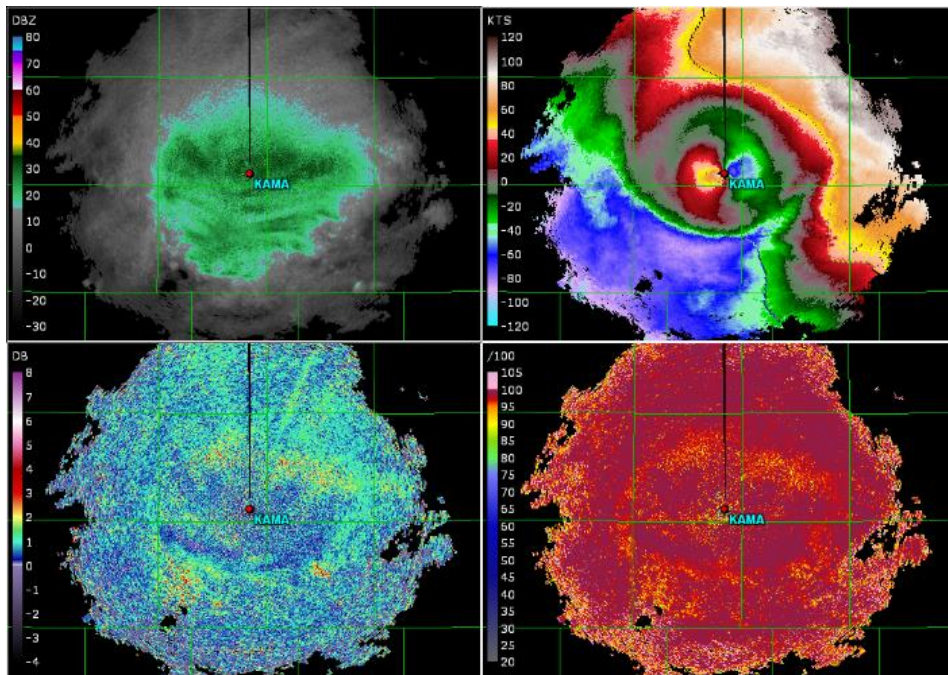


Fig. 4-3. Same as Fig. 4-1 except with a 10-dB sensitivity loss and are scored as a 3.

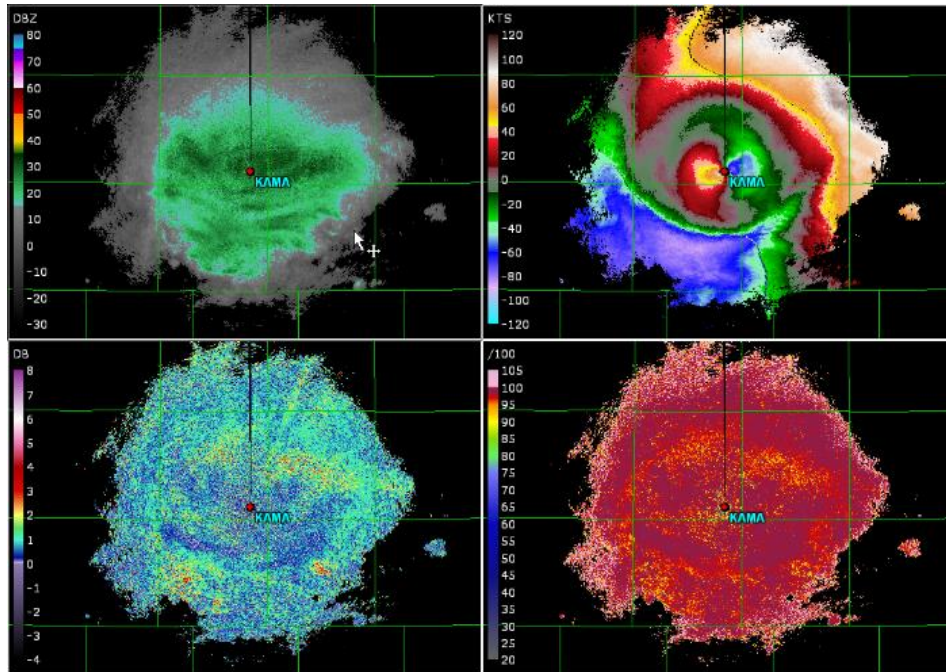


Fig. 4-4. Same as Fig. 4-1 except with a 14-dB sensitivity loss and are scored as a 4.

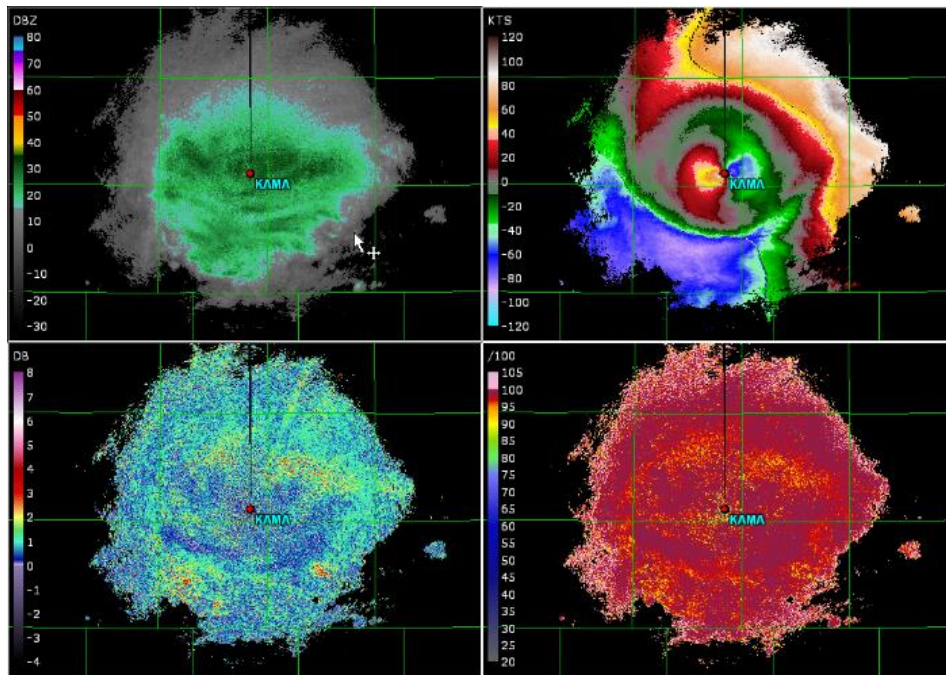


Fig. 4-5. Same as Fig. 4-1 except with a 20-dB sensitivity loss and are scored as a 5.

Figs. 4-6 to 4-10 show progressive sensitivity loss for Case 1, which contains a thunderstorm complex with a gust front producing damaging winds at the surface. The key feature for this case is the gust front itself and the velocity data in the clear air between the storm and the

gust front (circled in Fig. 4-6). Another decision driver is the increasing noisiness and number of invalid correlation coefficient estimates. Similar to Figs. 4-1 to 4-5, these simulated data exhibit 2 dB, 6 dB, 10 dB, 14 dB, and 20 dB of sensitivity loss and are scored as 1 through 5, respectively. While the gust front itself is preserved in reflectivity, the progressive loss of velocity data in the clear air gap can be clearly seen. Similarly, there are progressively more invalid correlation coefficients to the northeast of the radar.

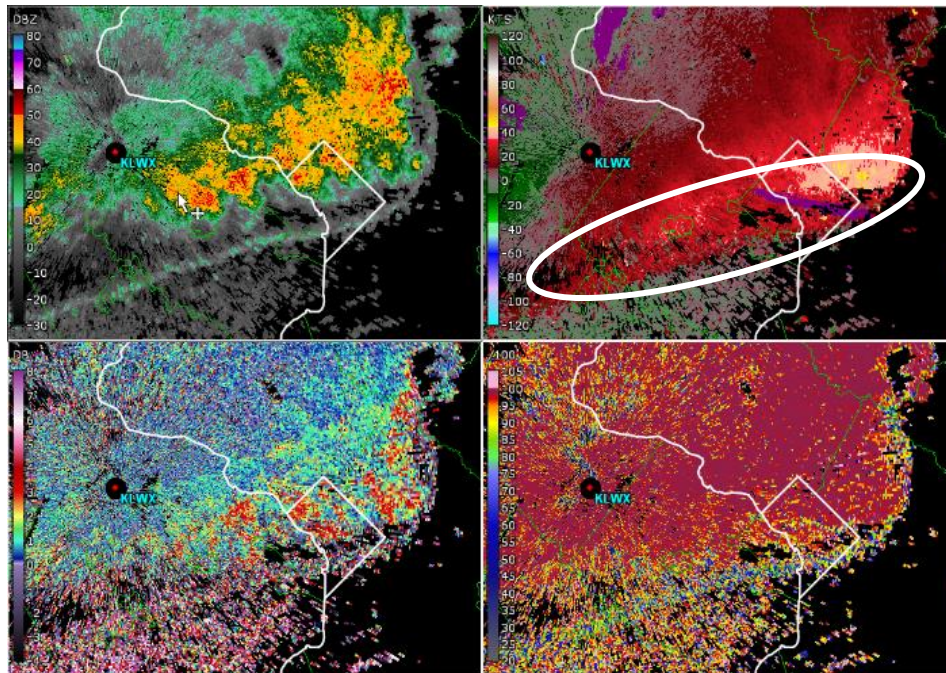


Fig. 4-6. Reflectivity (top left), Doppler velocity (top right), differential reflectivity (bottom left), and correlation coefficient (bottom right) for Case 1. These data have a 2-dB sensitivity loss and are scored as a 1.

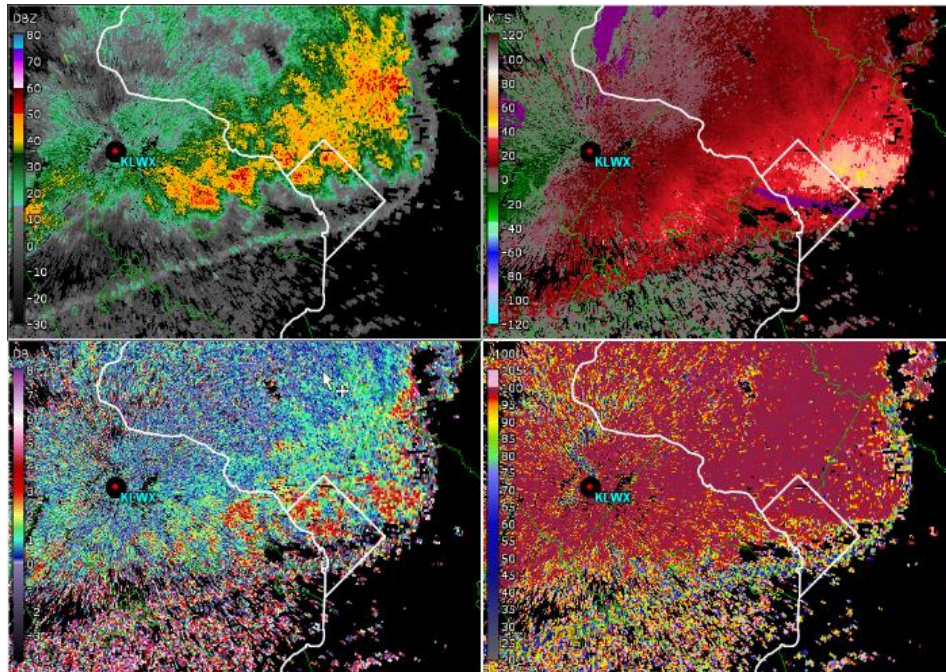


Fig. 4-7. Same as Fig. 4-6 except with a 6-dB sensitivity loss and are scored as a 2.

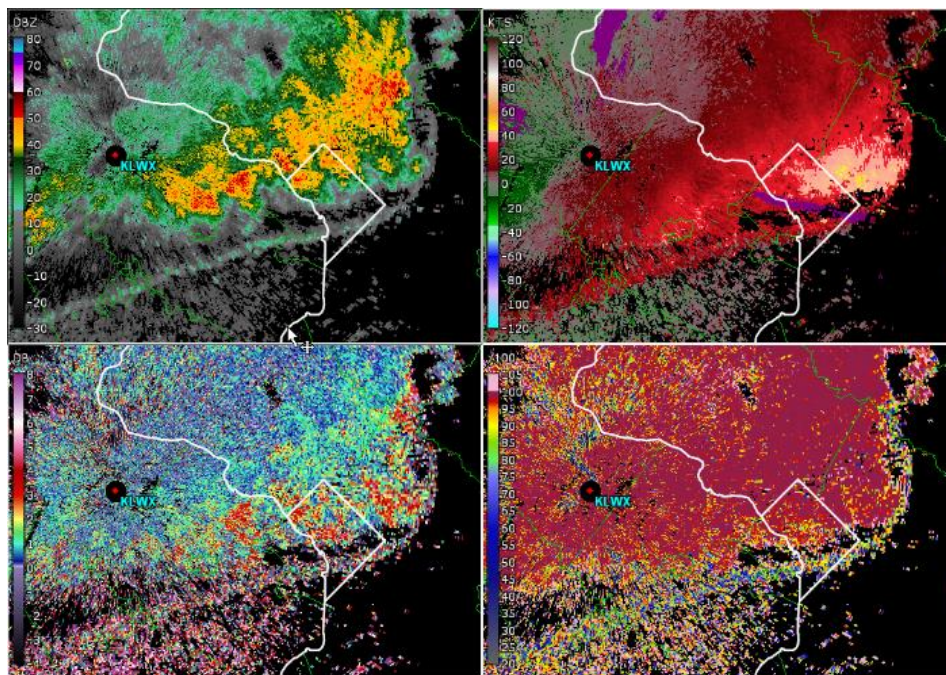


Fig. 4-8. Same as Fig. 4-6 except with a 10-dB sensitivity loss and are scored as a 3.

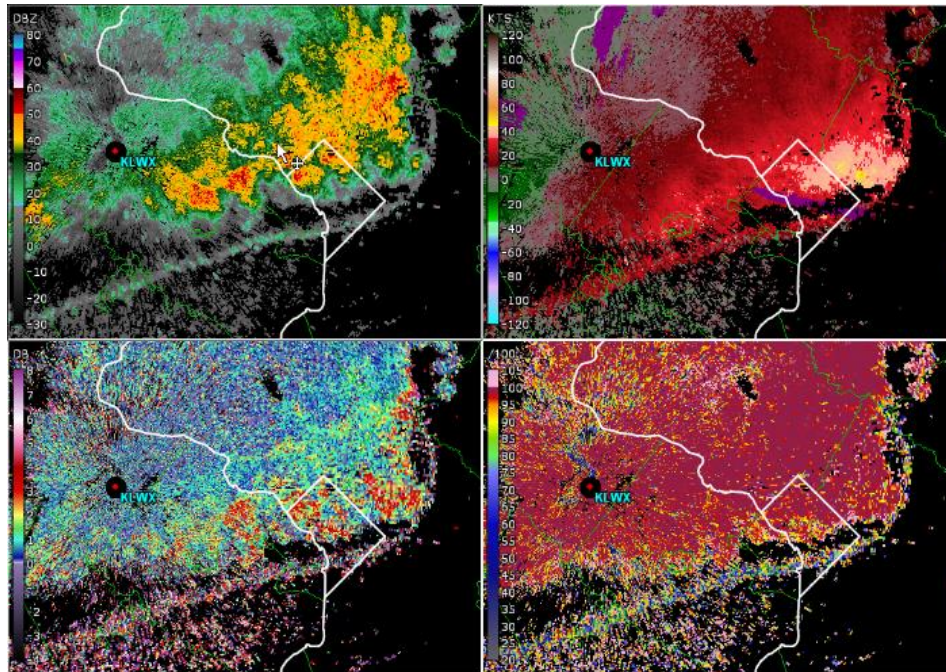


Fig. 4-9. Same as Fig. 4-6 except with a 14-dB sensitivity loss and are scored as a 4.

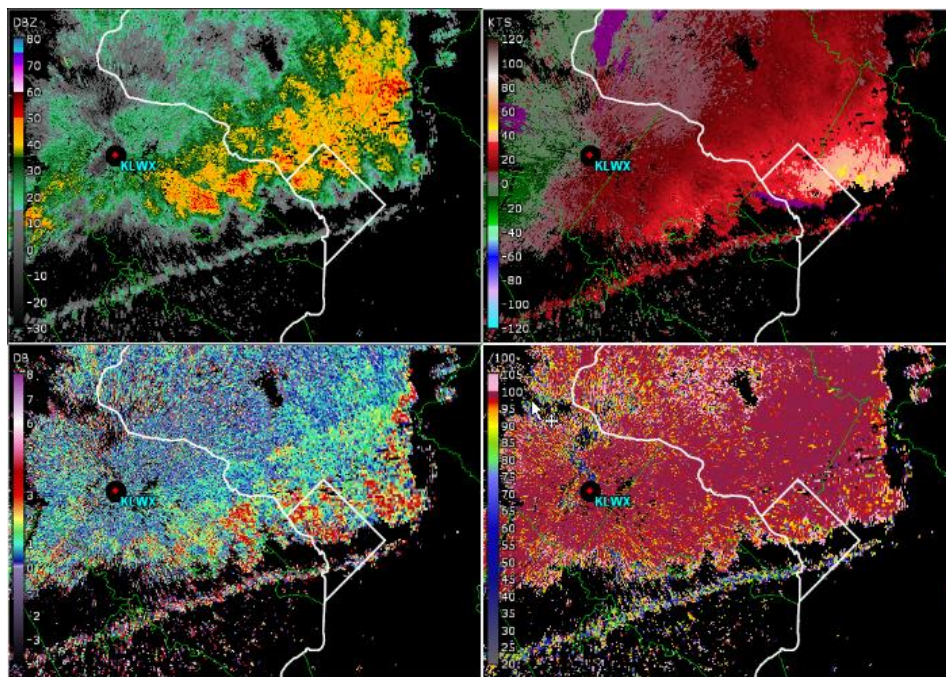


Fig. 4-10. Same as Fig. 4-6 except with a 20-dB sensitivity loss and are scored as a 5.

#### 4.4. Simulation Results

To better understand the relationship between sensitivity loss and its impacts on forecasters' interpretation of radar data, we fit a sigmoidal curve to our score data for each of the 8 cases. The

sigmoidal curve was chosen because the function asymptotically approaches the maximum (minimum) score as the sidelobe degradation is increased (decreased) to infinity (zero). This captures the fact that once the score reaches 5 (1), continuing to increase (decrease) sensitivity will not change the score. The fitted curve has the form

$$f(\text{SNR}_{\text{loss}}) = 1 + \frac{4}{1 + e^{-k(\text{SNR}_{\text{loss}} - x_o)}}, \quad (4.1)$$

where SNR loss is in dB units, and  $k$  and  $x_o$  are unknown parameters (to be determined) that control the steepness and the position of the center of the curve. We used a grid search that minimized the mean squared error between the fitted curve and our scoring data to determine the value of  $k$  and  $x_o$  for each case. The top panel of Fig. 4-11 shows the fitted curve for Case 2 (blue line) as a function of SNR loss where a 0-dB SNR loss (no loss) corresponds to a system with the same sensitivity as the WSR-88D. In this example, the value of  $k$  is 0.44 and the value of  $x_o$  is 8 dB. For the cases we selected, the average value of  $x_o$  is 7 dB with a standard deviation of 1.68 dB. The value of  $k$  varies between 0.26 and 0.44 with an average of 0.34 and a standard deviation of 0.059. The bottom panel of Fig. 4-11 shows the fitted curves (gray lines) for all cases and an additional curve (black line) with  $k$  and  $x_o$  equal to the average value of all cases.

While the average best-fit curve in Fig. 4-11 only represents a very limited number of cases, the data simulation and analysis processes described above could be extended in the future to include more and a much wider variety of cases. With enough cases, a curve similar to that in Fig. 4-11 could be used by decision makers to evaluate any future radar designs by comparing its sensitivity to that of the WSR-88D. For example, using the preliminary results of this study, a proposed radar system with sensitivity that is 4 dB lower than the WSR-88D would produce data that have an impact score of 2, indicating that it would be acceptable but with minimal distractions. On the other hand, a proposed system with sensitivity that is 10 dB lower than that of the WSR-

88D would have a score of 4 and would need to be rejected because data quality losses can significantly impact forecasters.

As mentioned before, this study is a first step in describing the relationship between sensitivity loss and impact on forecasters; the impact curve should be refined by simulating and analyzing more cases. Moreover, our current simulations cannot show the benefits of having sensitivity better than that of the WSR-88D, which should also be quantified in a future study.

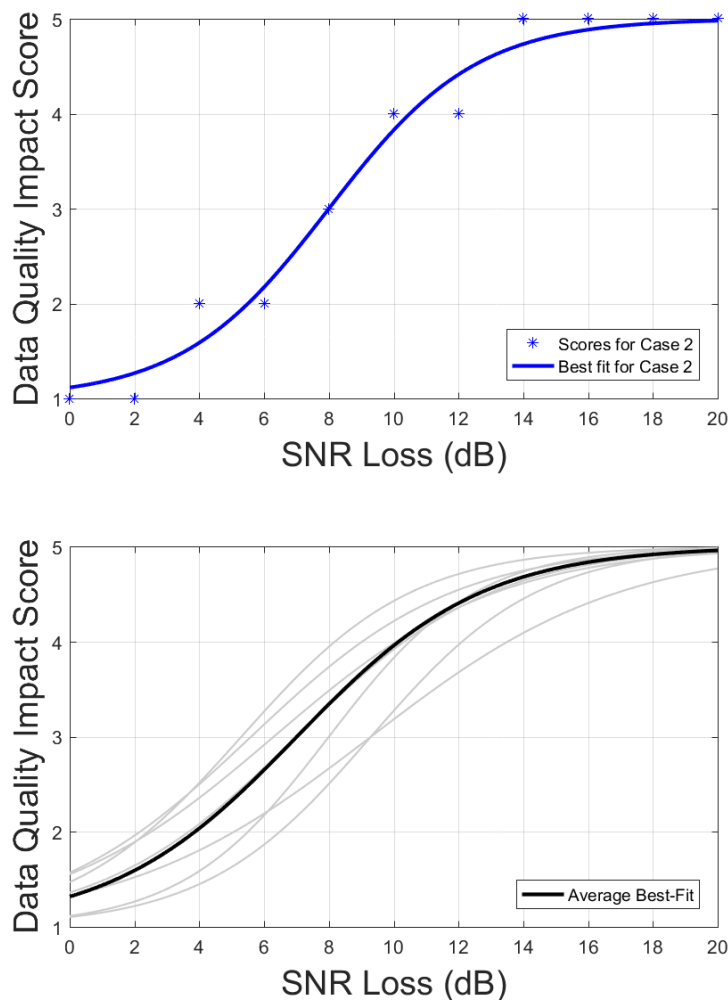


Fig. 4-11. Scores for the simulated patterns (blue stars) and the fitted Best-Fit for Case 2 (blue line) are shown in the top panel. The fitted curves for all cases and the average best-fit curve (black line) are shown in the bottom panel. The x-axes are SNR loss in dB units. Note that the curve

fitting minimizes the mean squared error and captures the trend of the scores. The average best-fit curve uses parameters that are the average of all cases.

#### **4.5. Conclusions**

In this study, we focused on the impact of sensitivity changes on forecasters. We simulated data for the same weather event as collected by radar systems with progressively lower sensitivity by adding white noise to simulated weather data while keeping all other radar characteristics constant. For each case, we varied the sensitivity of the simulated radar system from matching that of the WSR-88D to 20 dB lower. The simulated data were analyzed and scored, where the scoring system was based on the amount of erosion of the footprint of the storm and key weather features. Using the scores, we fit sigmoidal curves for each weather case and developed an average best-fit that captures the relationship between sensitivity loss and impact on forecasters. An extension of this approach to include a larger number of cases and enough diversity of events can be used to generate a more robust impact curve. This impact curve can be used by decision makers to evaluate future radar designs by directly comparing the sensitivity of the proposed system to the sensitivity of the WSR-88D.

## **5. Project Conclusions**

The next generation of weather radar for the NWS is likely to require tradeoffs between system performance and cost. One aspect of the radar performance in these tradeoffs is the radar data quality. Any changes to data quality can impact the decisions and products generated by consumers of radar data. Therefore, it is important to understand the relationship between changes to data quality and impacts on the users. This work is a first step to develop a methodology that connects data quality changes to impact on forecasters, who use radar data as a primary source of information in warning decisions. We simulated and analyzed data with different spatial resolution, azimuthal sampling, and/or sensitivity to characterize the relationship between data quality changes and their impacts on forecasters' interpretation of the radar data. It is important to note that our results should not be interpreted as providing recommendations for changing technical requirements for the replacement system. This is because our study was limited in scope and only focused on one part of the overall impacts caused by data quality changes: forecaster interpretation of base data. A more comprehensive study that includes many more cases, involves a diverse group of forecasters, and includes data quality impacts on algorithms is needed to provide more valid recommendations for changing any technical requirements. Instead, our results can be used as a proof of concept for the methodology. Eventually, the results obtained from an extension of such an approach can be used by decision makers to evaluate the possible operational impacts of any proposed radar design, which is an important component of the evaluation of tradeoffs between system performance and cost.

## 6. References

- Andra, D. L., E. M. Quetone, and W. F. Bunting, 2002: Warning Decision Making: The Relative Roles of Conceptual Models, Technology, Strategy, and Forecaster Expertise on 3 May 1999. *Wea. Forecasting*, **17**, 559-566.
- Brown, R. A., L. R. Lemon, and D. W. Burgess, 1978: Tornado detection by pulsed Doppler radar. *Mon. Wea. Rev.*, **106**, 29-38.
- Brown, R. A., 1998: Nomogram for aiding the interpretation of tornadic vortex signatures measured by Doppler radar. *Wea. Forecasting*, **13**, 505-512.
- Brown, R. A., V. T. Wood, and D. Sirmans, 2002: Improved tornado detection using simulated and actual WSR-88D data with enhanced resolution. *J. Atmos. Oceanic Technol.*, **19**, 1759-1771.
- Brown, R. A., and V. T. Wood, 2012: The tornadic vortex signature: an update. *Wea. Forecasting*, **27**, 525-530.
- Doviak, R. and D. S. Zrnić, 1998: WSR-88D Radar for Research and Enhancement of Operations: Polarimetric Upgrades to Improve Rainfall Measurements. NOAA/NSSL Report, 110 pp, [https://nssl.noaa.gov/publications/wsr88d\\_reports/](https://nssl.noaa.gov/publications/wsr88d_reports/).
- Doviak, R. and D. S. Zrnić, 2006: Doppler Radar and Weather Observations, Dover Publications, Inc., 562 pp.

- Doviak, R., 2017: A Memorandum on Comparisons of Weather and Aircraft Surveillance Radar Requirements to Determine Key Features for a 10-cm MPAR and SENSr. NOAA/NSSL Report, 41pp, [https://nssl.noaa.gov/publications/mpar\\_reports/](https://nssl.noaa.gov/publications/mpar_reports/).
- Galati, G. and G. Pavan, 1995: Computer simulation of weather radar signals. *Simul. Pract. Theory*, **3**, 17-44.
- Lei, L., G. Zhang, R. Doviak, and S. Karimkashi, 2015: Comparison of theoretical biases in estimating polarimetric properties of precipitation with weather radar using parabolic reflector, or planar and cylindrical arrays. *IEEE Trans. Geosci. Remote Sens.*, **54**, 431-451.
- Melnikov, V., D. S. Zrnić, and D. W. Burgess, 2015: Oversampling in azimuth to improve detection of vortices. *37<sup>th</sup> Conf. on Radar Meteor.*, Norman, OK, Amer. Meteor. Soc., 13B.2. [Available online at <https://ams.confex.com/ams/37RADAR/webprogram/Paper274550.html>]
- Mitchell, E. D., S. V. Vasiloff, G. J. Stumpf, A. Witt, M. D. Eilts, J. T. Johnson, and K. W. Thomas, 1998: The National Severe Storms Laboratory tornado detection algorithm. *Wea. Forecasting*, **13**, 352-366.
- NOAA/NWS, 2015: Radar Functional Requirements, NOAA/NWS Internal Rep., 58pp. [Online] Available: [https://www.roc.noaa.gov/WSR88D/PublicDocs/NOAA\\_Radar\\_Functional\\_Requirements\\_Final\\_Sept%202015.pdf](https://www.roc.noaa.gov/WSR88D/PublicDocs/NOAA_Radar_Functional_Requirements_Final_Sept%202015.pdf)
- NOAA/NWS, 2018, National Weather Service Instructions 10-511, Accessed 16 April 2019, <https://www.nws.noaa.gov/directives/sym/pd01005011curr.pdf>.

- Proud, J. L., K. K. Droegemeier, V. T. Wood, and R. A. Brown, 2009: Sampling strategies for tornado and mesocyclone detection using dynamically adaptive Doppler radars: A simulation study. *J. Atmos. Oceanic Technol.*, **26**, 492-507.
- Schvartzman, D and C. D. Curtis, 2019: Signal Processing and Radar Characteristic (SPARC) simulator: a flexible dual-polarization weather-radar signal simulation framework based on preexisting radar-variable data. *IEEE Journal of Selected Topics in Applied Earth Observations and Remote Sensing*, **12**, 135-150.
- Spectrum Efficient National Surveillance Radar (SENSR) Preliminary Performance Requirements. Jun. 29, 2018. [Online]. Available: <https://faaco.faa.gov/index.cfm/attachment/download/73825>.
- Torres, S., and C. Curtis, 2007: Initial implementation of super-resolution data on the NEXRAD network. *23<sup>rd</sup> Int. Conf. on Interactive Information and Processing Systems for Meteorology, Oceanography, and Hydrology*, San Antonio, TX, Amer. Meteor. Soc., 5B.10. [Available online at [https://ams.confex.com/ams/87ANNUAL/techprogram/paper\\_116240.htm](https://ams.confex.com/ams/87ANNUAL/techprogram/paper_116240.htm).]
- Wood, V. T., and R. A. Brown, 1997: Effects of radar sampling on single-Doppler velocity signatures of mesocyclones and tornados. *Wea. Forecasting*, **12**, 928-938.
- Wood, V. T., R. A. Brown, and D. Sirmans, 2001: Technique for improving detection of WSR-88D mesocyclone signatures by increasing angular sampling. *Wea. Forecasting*, **16**, 177-184.
- Wood, V. T., and R. A. Brown, 2011: Simulated tornadic vortex signatures of tornado-like vortices having one- and two-celled structures. *J. Appl. Meteor. Climatol.*, **50**, 2338-2342.

Zrnić, D. S., 1975: Simulation of weatherlike Doppler spectra and signals. *J. Appl. Meteor.*, 14, 619-620.

## Appendix A: Summary of Cases in Table 2-2

For the study on the impacts of changing sidelobe levels, we simulated and analyzed the 13 cases listed in Table 2-2. For each case, we simulated 10 antenna patterns with progressively higher sidelobe levels. Each simulation involved simulating and analyzing data at eight different elevations between  $0.5^\circ$  and  $5.1^\circ$ . Overall, radar data (i.e., three spectral moments and three polarimetric variables) for 1040 PPIs were simulated and analyzed during this study. Since it is not possible to include the entirety of our simulated data in this report, we simply show PPI plots of the WSR-88D data for the cases in Table 2-2 to demonstrate the range of cases from different parts of the country that were used in this study. All PPIs are at  $0.5^\circ$  elevation unless noted otherwise. Since this portion of the study focused on elevation sidelobe contaminations, we also include range-height indicator (RHI) plots to show the vertical reflectivity gradient for each case.

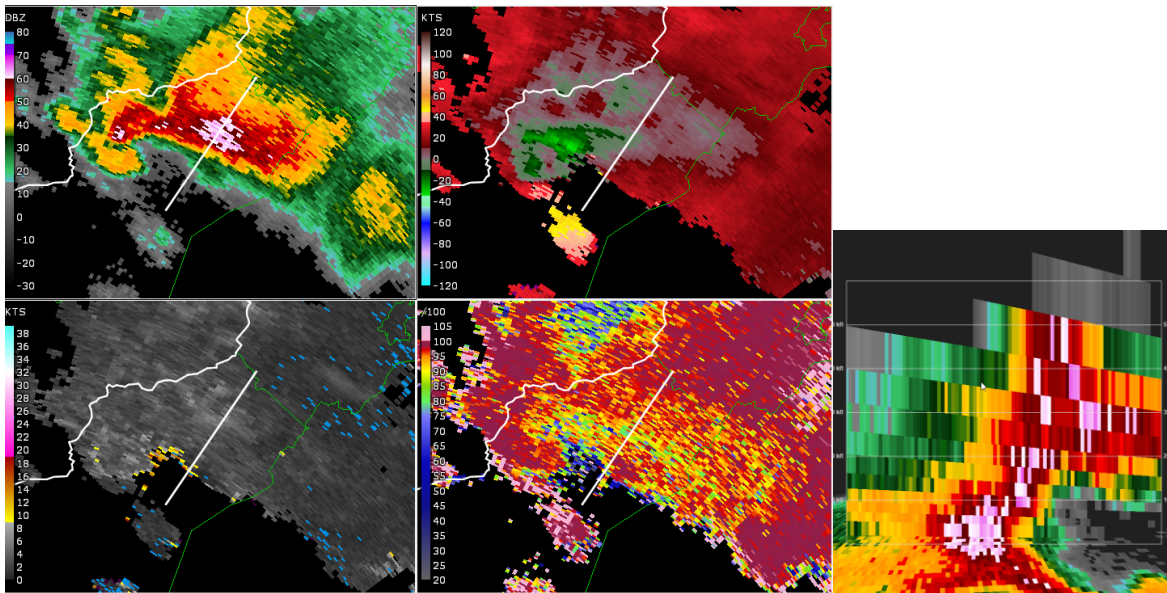


Fig. A-1. Reflectivity (top left), storm-relative velocity (top center), spectrum width (bottom left), and correlation coefficient (bottom center) for KMRX Morristown, TN July 27, 2014 20:55Z. The RHI plot (right) is along the cut indicated by the white line.

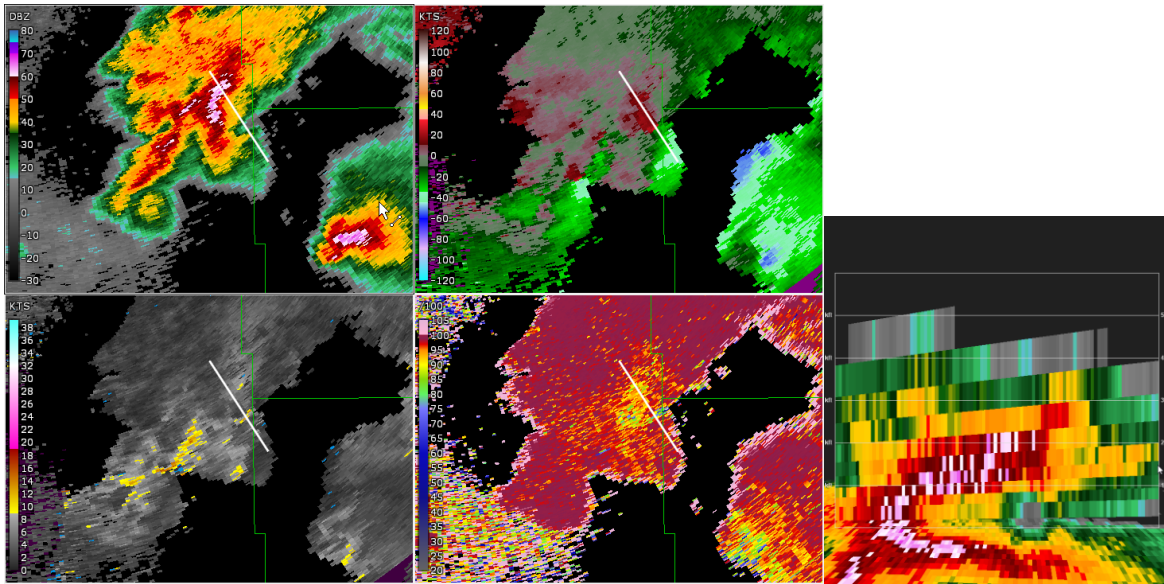


Fig. A-2. Same as Fig. A-1 except for KUDX Rapid City, SD June 14, 2014 03:47Z.

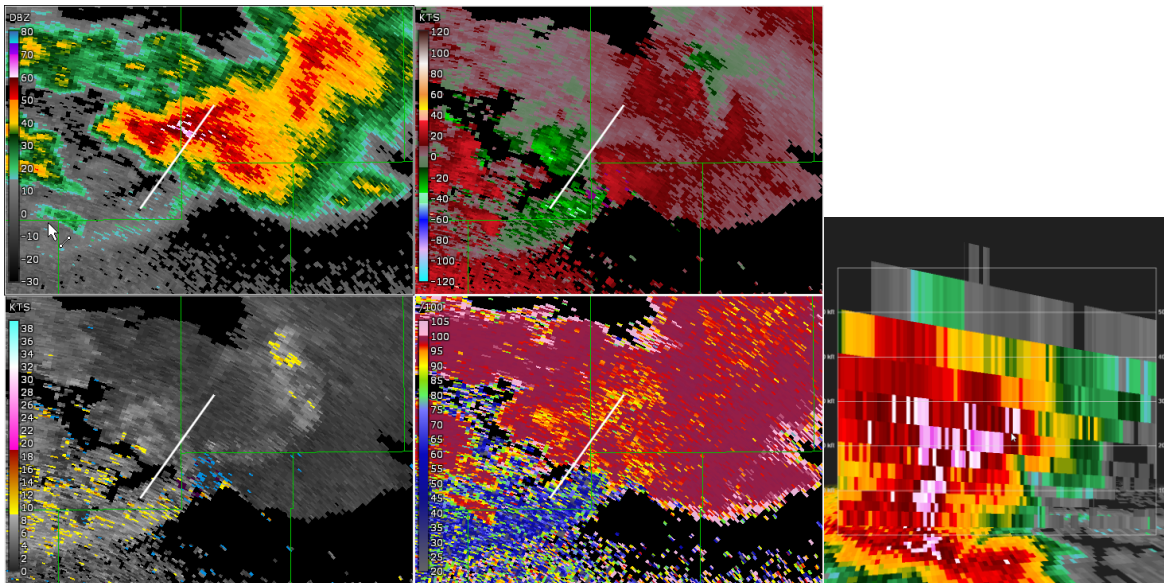


Fig. A-3. Same as Fig. A-1 except for KTWX Topeka, KS September 18, 2015 01:20Z.

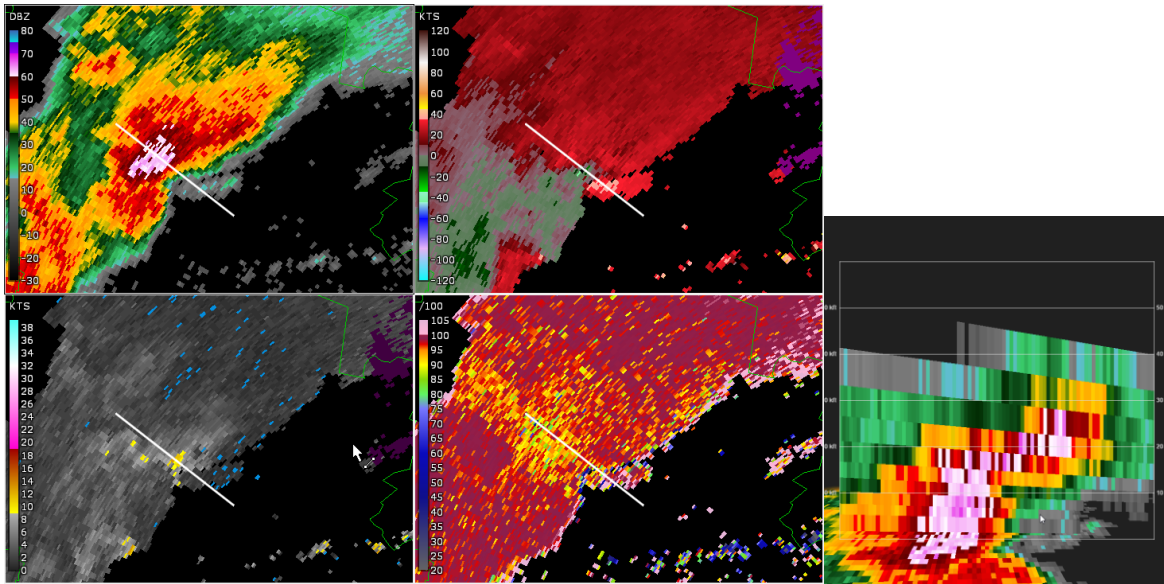


Fig. A-4. Same as Fig. A-1 except for KBOX Boston, MA August 4, 2015 19:05Z

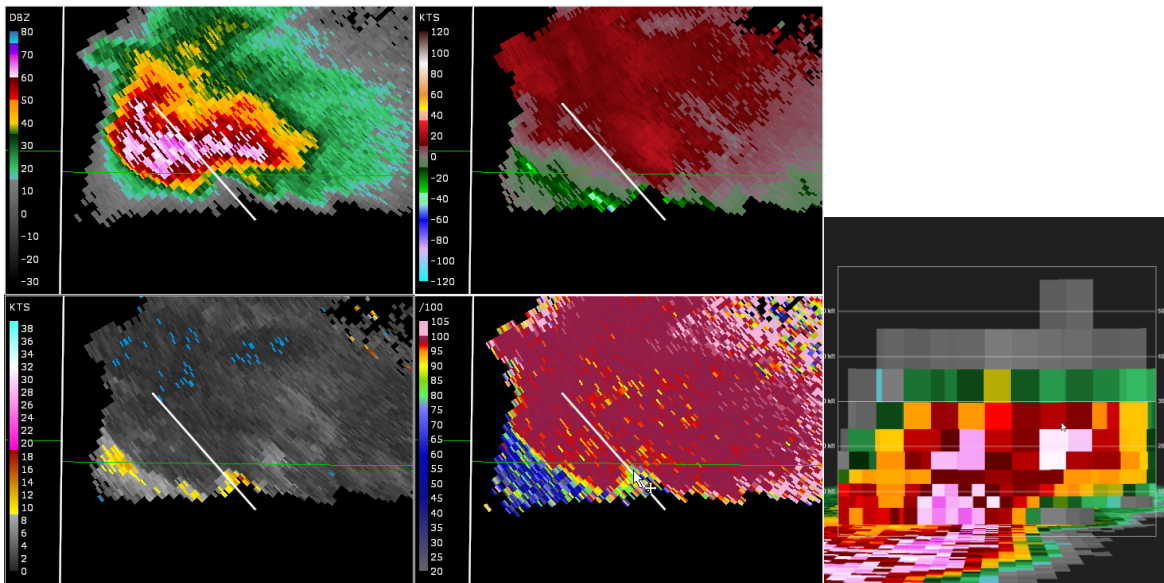


Fig. A-5. Same as Fig. A-1 except for KUDX Rapid City, SD June 21, 2015 00:11Z.

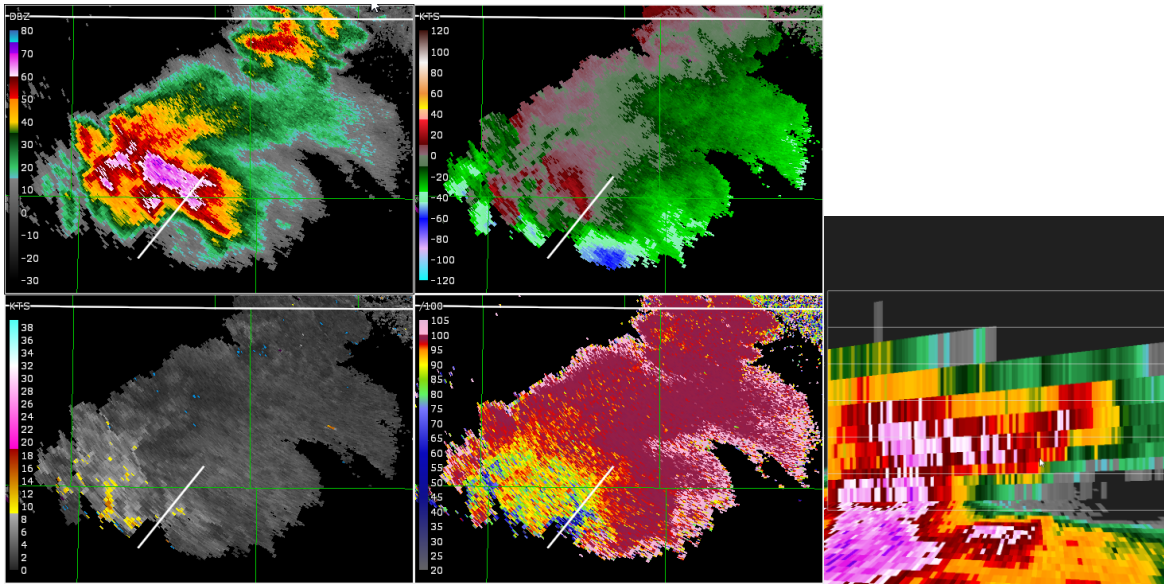


Fig. A-6. Same as Fig. A-1 except for KUEX Hastings, NE September 10, 2015 22:03Z.

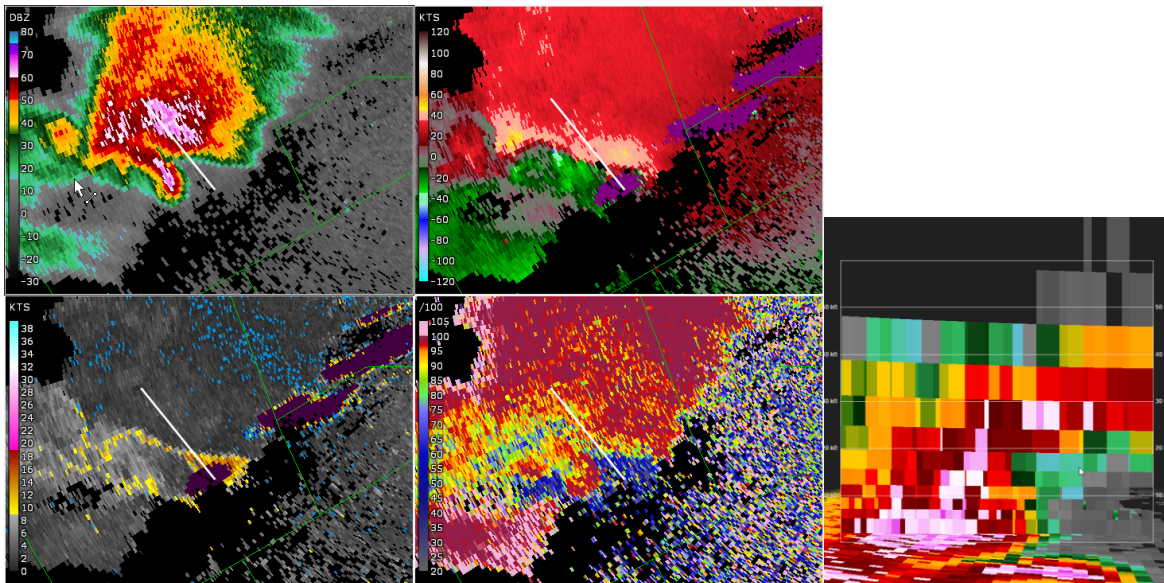


Fig. A-7. Same as Fig. A-1 except for KFWS Fort Worth, TX April 26, 2015 23:43Z.

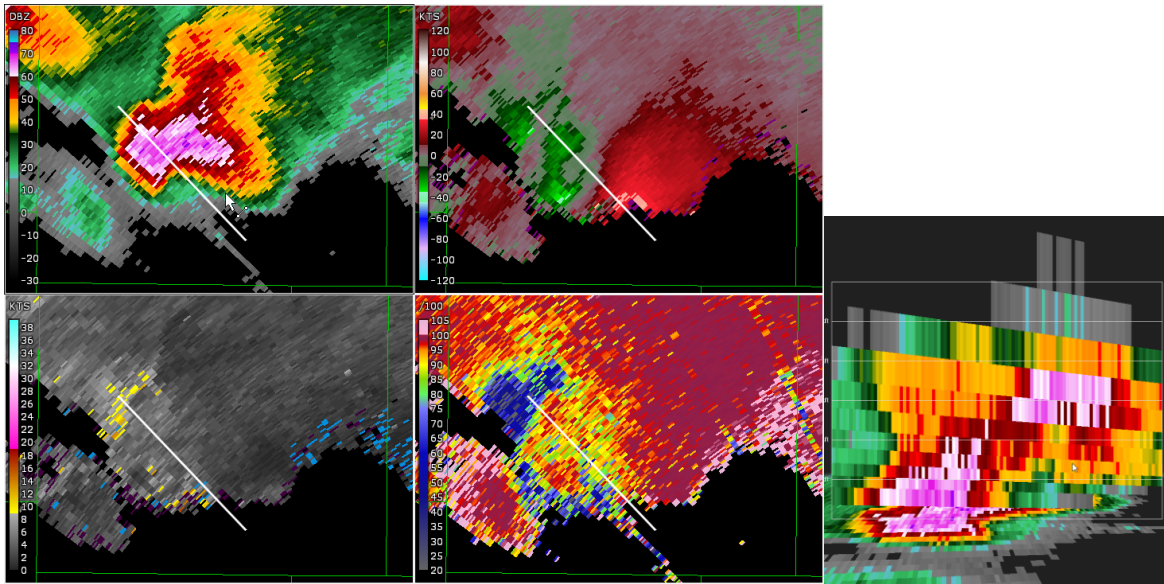


Fig. A-8. Same as Fig. A-1 except for KTWX Topeka, KS September 10, 2015.

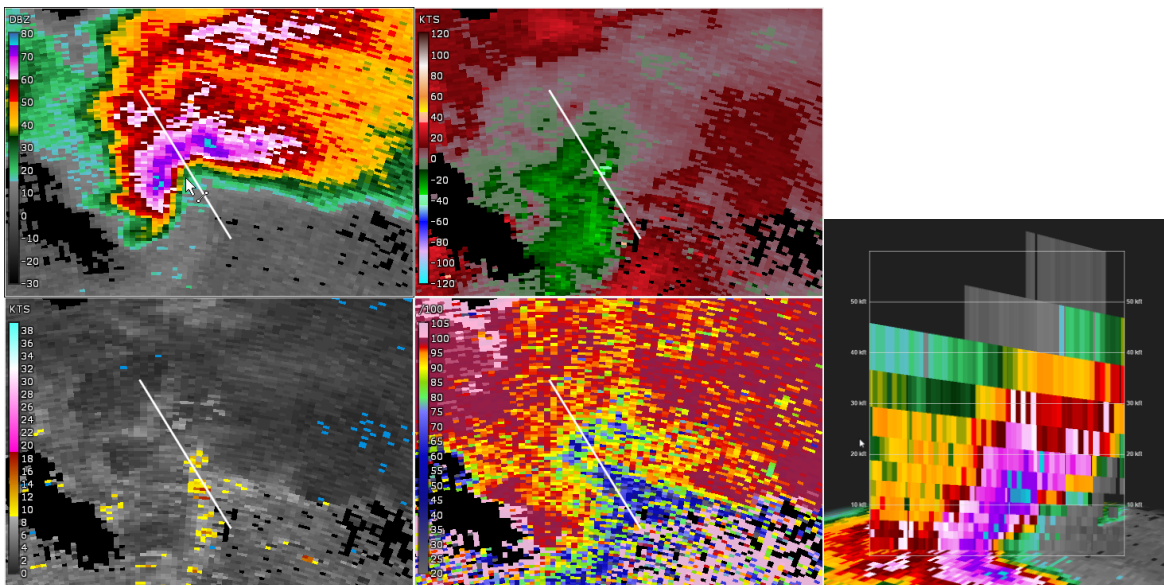


Fig. A-9. Same as Fig. A-1 except for KDYX Dyess AFB, TX April 2, 2014 00:50Z. This case is an outlier for our study because there is extensive azimuthal sidelobe contamination for multiple elevations.

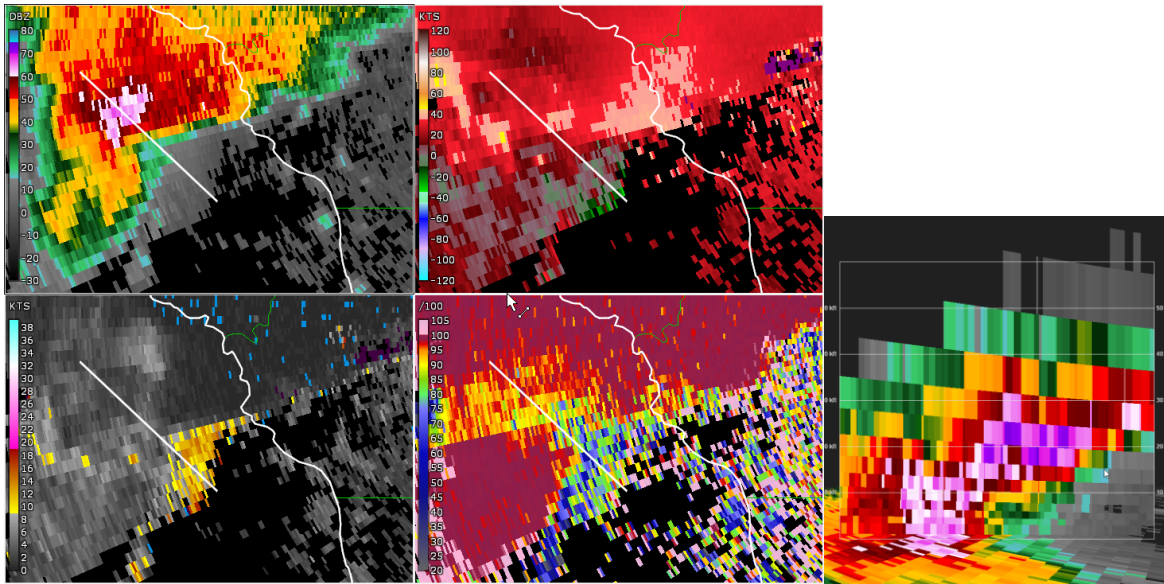


Fig. A-10. Same as Fig. A-1 except for KDFX Laughlin AFB, TX May 25, 2014 22:58Z.

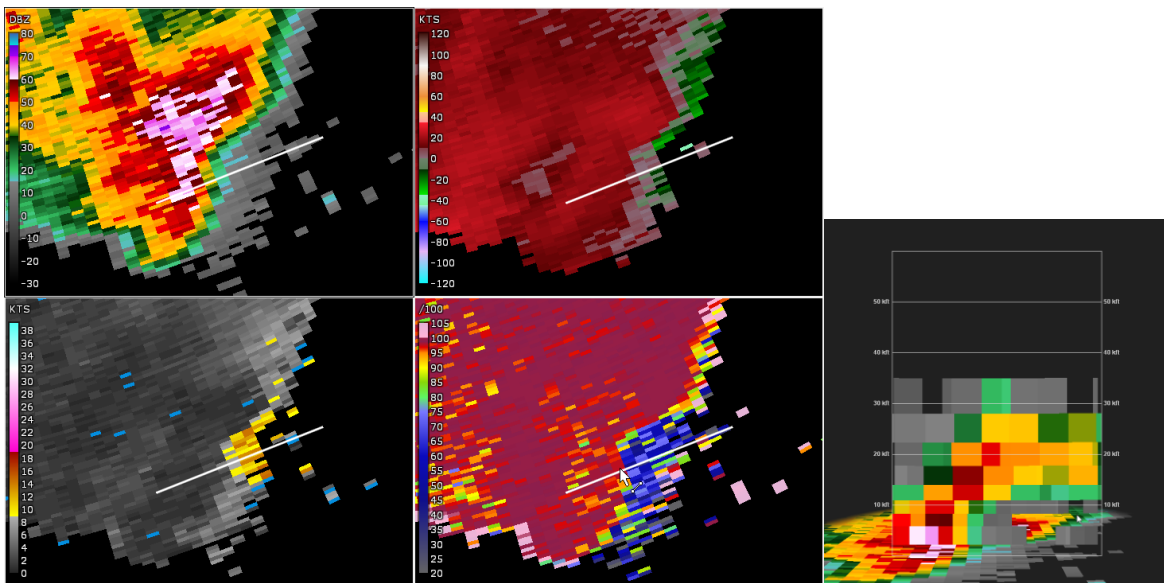


Fig. A-11. Same as Fig. A-1 except for KLRX Elko, NV July 22, 2014 04:45Z.

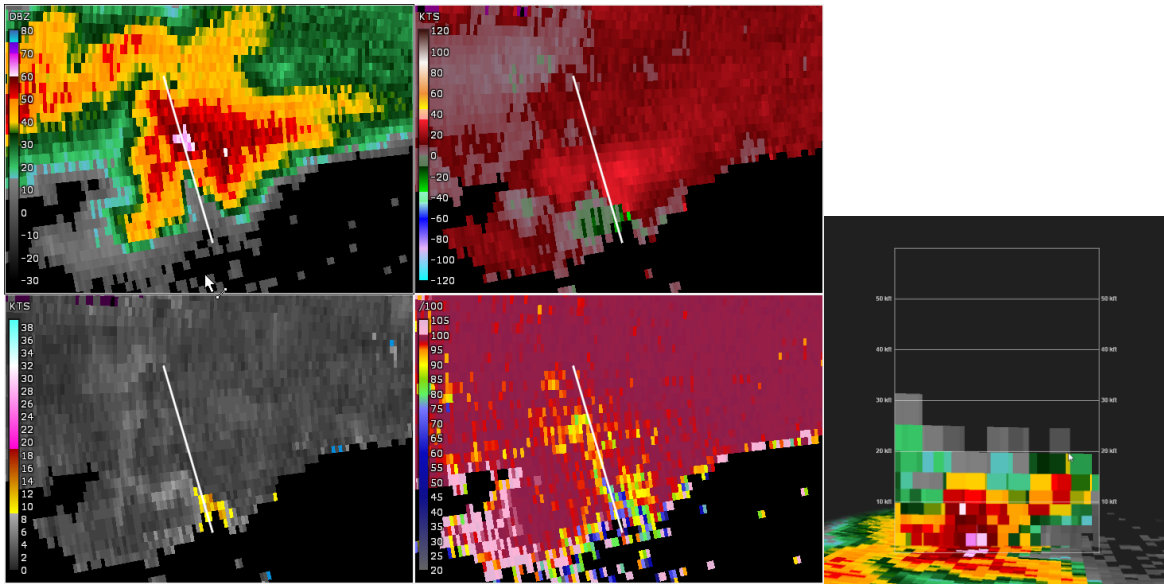


Fig. A-12. Same as Fig. A-1 except for KGLD Goodland, KS May 23, 2015 00:39Z

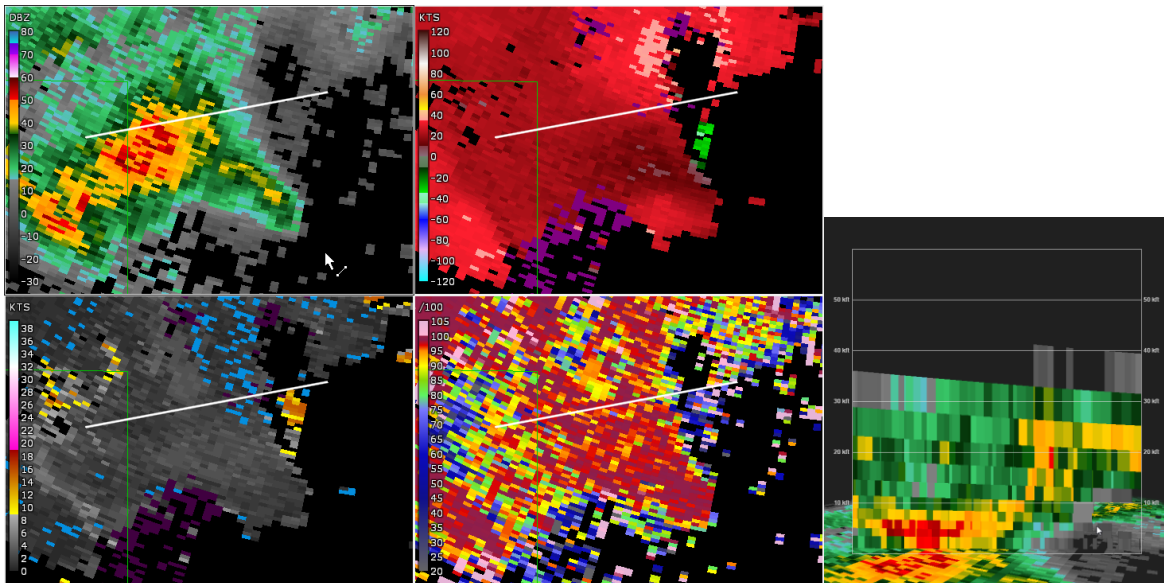


Fig. A-13. Same as Fig. A-1 except for KAFX Pocatello, ID June 1, 2015 21:12Z.

## **Appendix B: Summary of Cases in Table 2-4**

The cases listed in Table 2-4 were used to study the impacts of the beam broadening effect and changing the azimuthal sampling grid. For this study, we simulated data from three radar system (i.e., the scaled PAR, the CB-1.4° system, and the CB-1.0° system). Because the beamwidth of the scaled PAR varies as a function of scan angle, we simulated three array orientations for each weather case to better capture the impact of beam broadening for all scan angles. In total, data for 144 PPIs were simulated and analyzed in this part of the study.

For the study on the impacts of changing the azimuthal sampling grid, we simulated data from the scaled PAR using three different azimuthal sampling grids. For the same reason explained before, we simulated three array orientations for each weather case to better capture the full impact of changing the azimuthal sampling grid. In total, data for 144 PPIs were simulated and analyzed for this part of the study. In this appendix, we show the WSR-88D data for each case listed in Table 2-4 to demonstrate the variety in type and location for the cases we used. All PPIs are from 0.5° elevation unless noted otherwise.

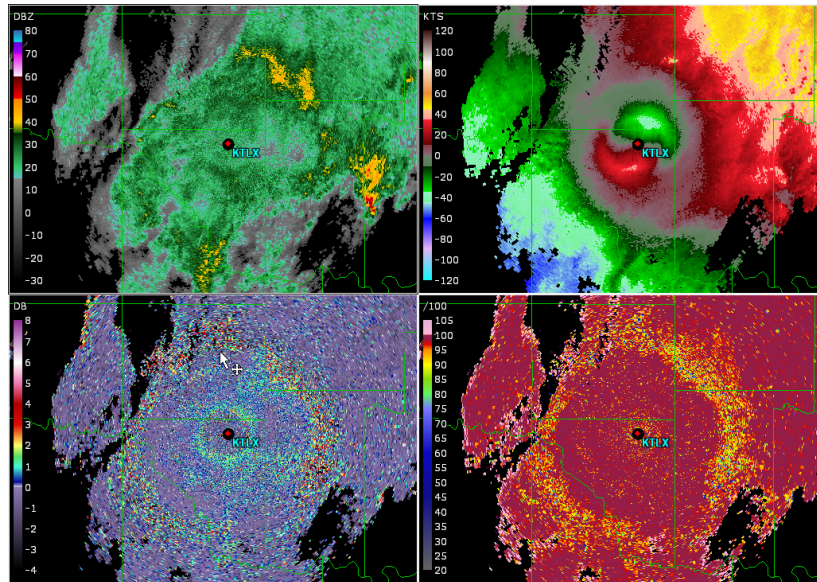


Fig. B-1. Reflectivity (top left), Doppler velocity (top right), differential reflectivity (bottom left), and correlation coefficient (bottom right) for KTLX Norman, OK March 2, 2014 20:37Z at 4.0° elevation.

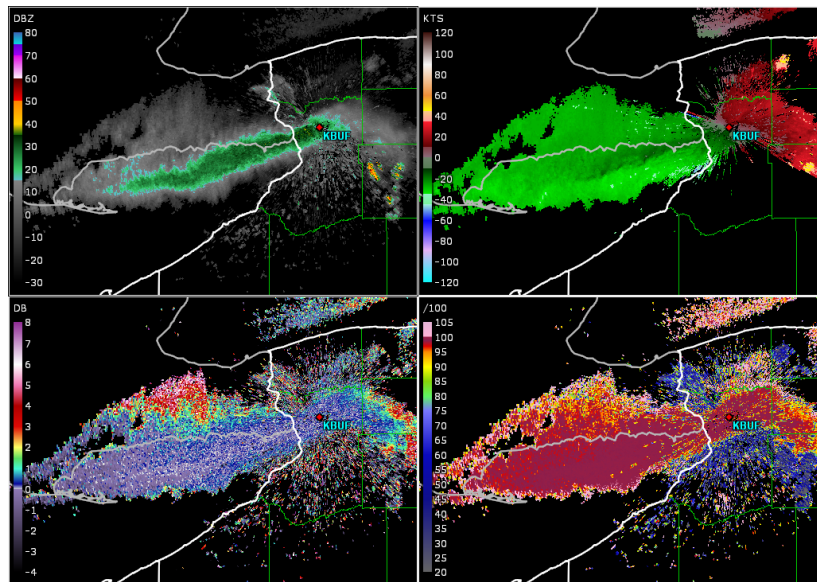


Fig. B-2. Same as Fig. B-1 except for KBUF Buffalo, NY November 19, 2014 12:11Z.

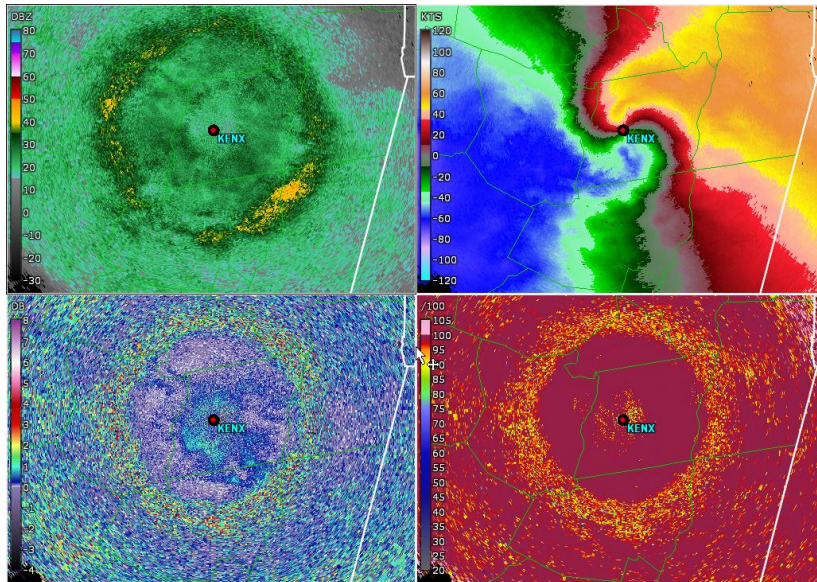


Fig. B-3. Same as Fig. B-1 except for KENX Albany, NY January 4, 2015 00:01Z at 3.4° elevation.

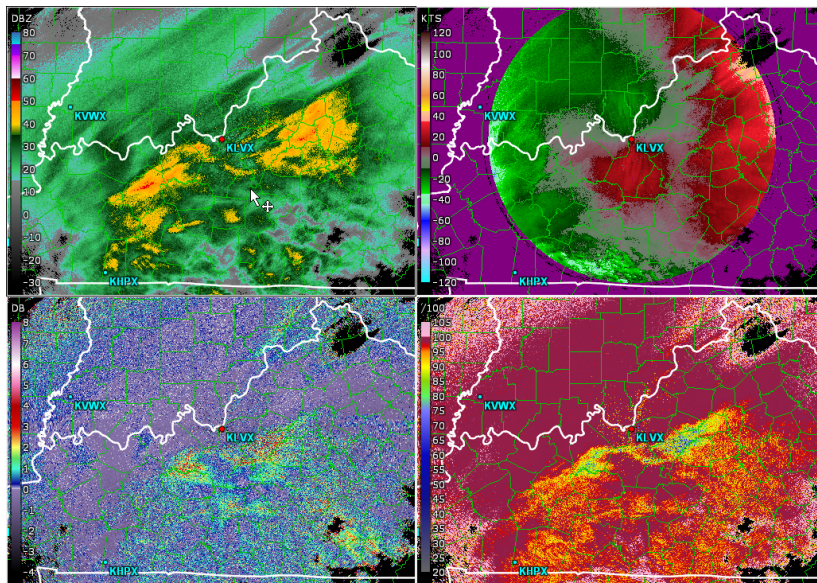


Fig. B-4. Same as Fig. B-1 except for KLVX Louisville, KY March 4, 2015 22:40Z.

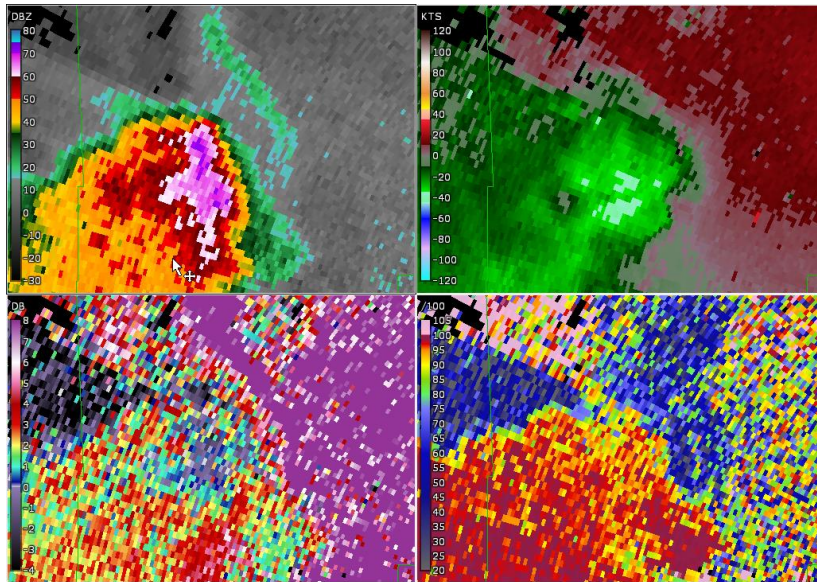


Fig. B-5. Same as Fig. B-1 except for KBGM Binghamton, NY May 3, 2012 23:49Z at 0.9° elevation.

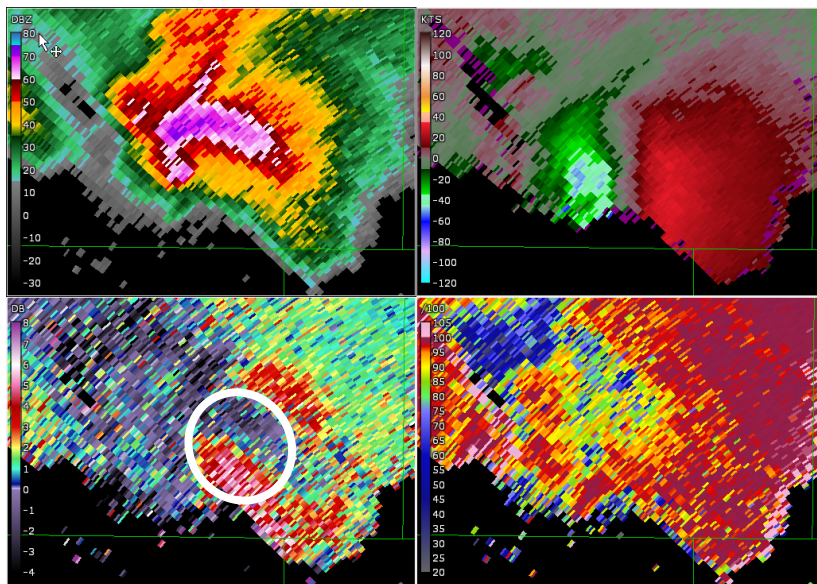


Fig. B-6. Same as Fig. B-1 except for KTWX Topeka, KS September 10, 2015 23:25Z.

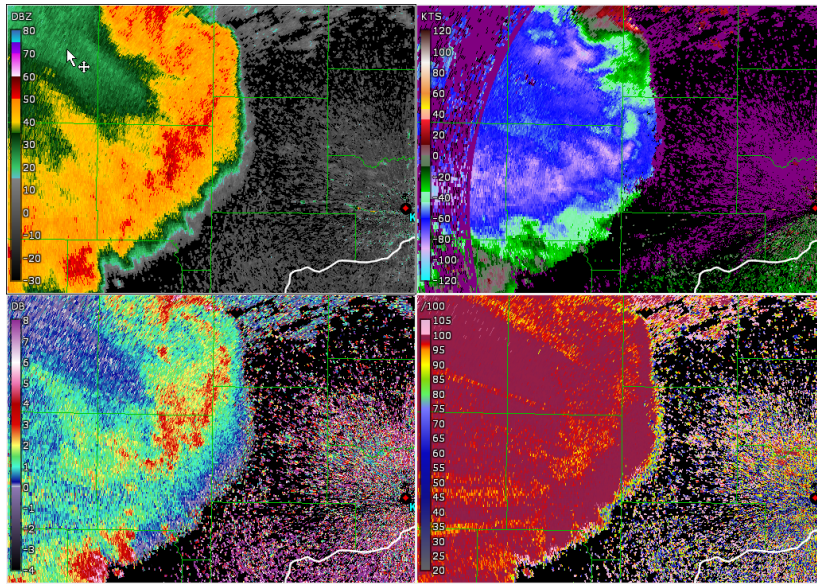


Fig. B-7. Same as Fig. B-1 except for KDVN Quad Cities, IA June 30, 2014 20:06Z.

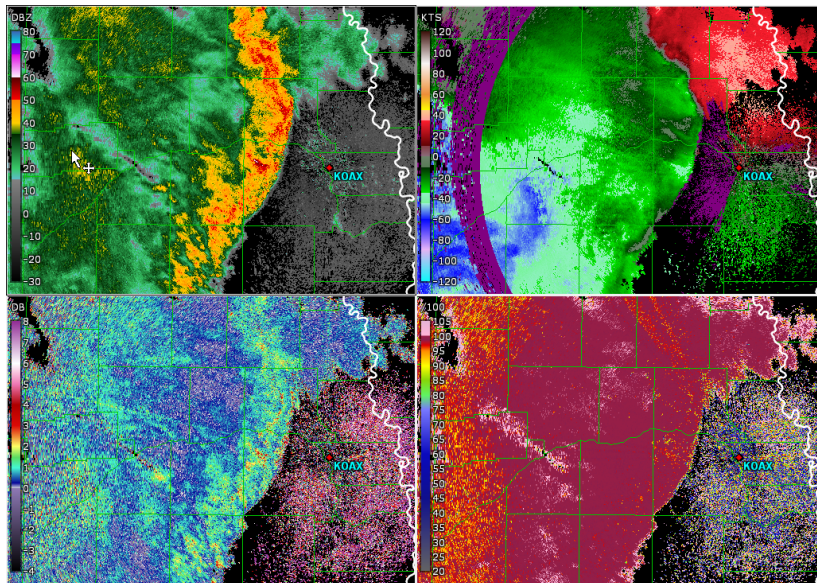


Fig. B-8. Same as Fig. B-1 except for KOAX Omaha, NE June 27, 2014 1159Z.

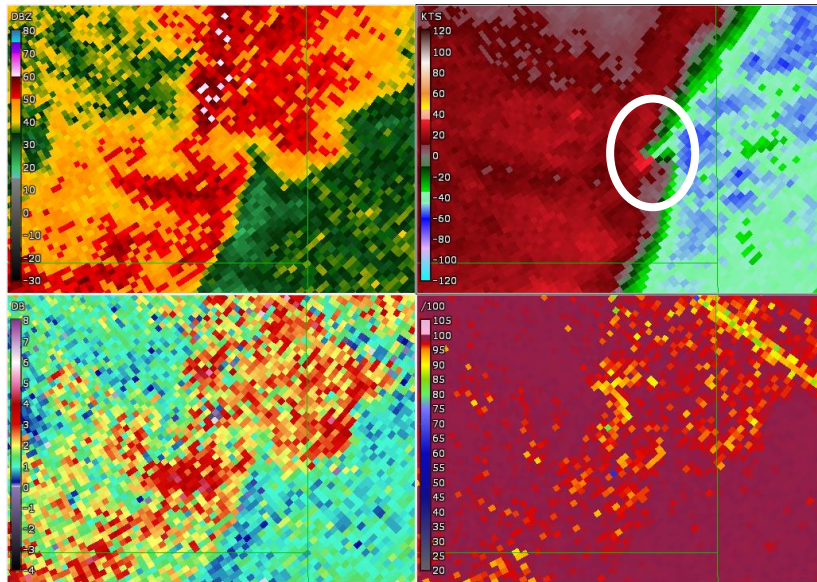


Fig. B-9. Reflectivity (top left), storm-relative velocity (top right), differential reflectivity (bottom left) and correlation coefficient (bottom right) for KTWX Topeka, KS February 29, 2012 03:02Z. The estimated storm motion is  $240^{\circ}$  at 43 kts.

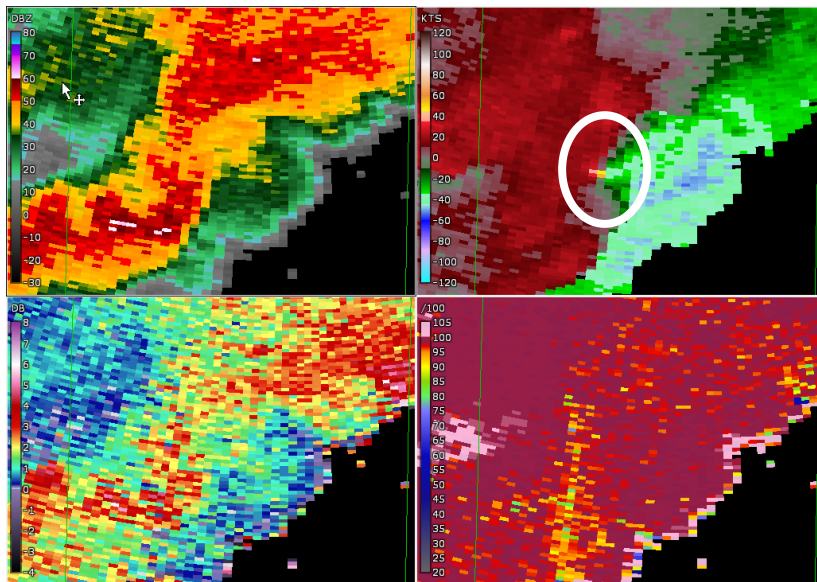


Fig. B-10. Same as Fig. B-9 except for KSGF Springfield, MO February 29, 2012 07:09Z. The estimated storm motion is  $260^{\circ}$  at 57 kts.

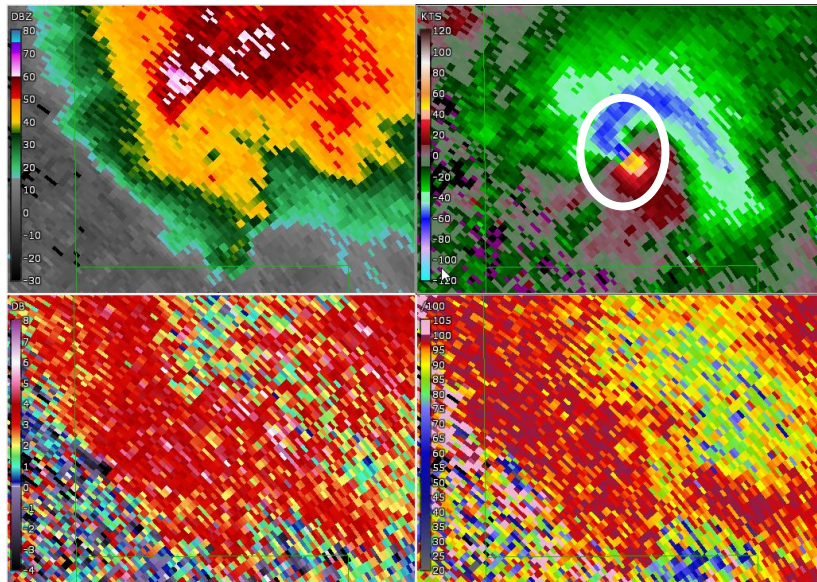


Fig. B-11. Same as Fig. B-9 except for KDDC Dodge City, KS May 19, 2013 00:23Z. The estimated storm motion is  $219^\circ$  at 61 kts.

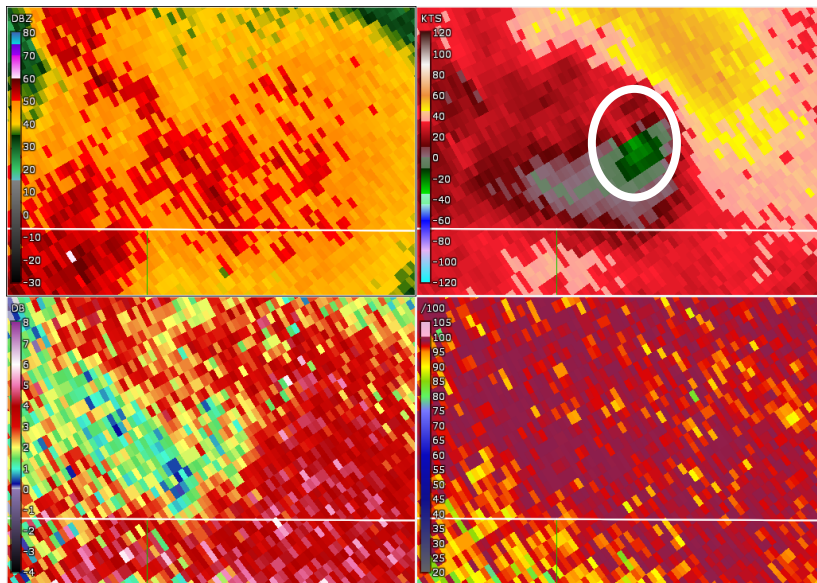


Fig. B-12. Same as Fig. B-9 except for KUEX Hastings, NE May 27, 2013 22:51Z. The estimated storm motion is  $228^\circ$  at 19 kts.

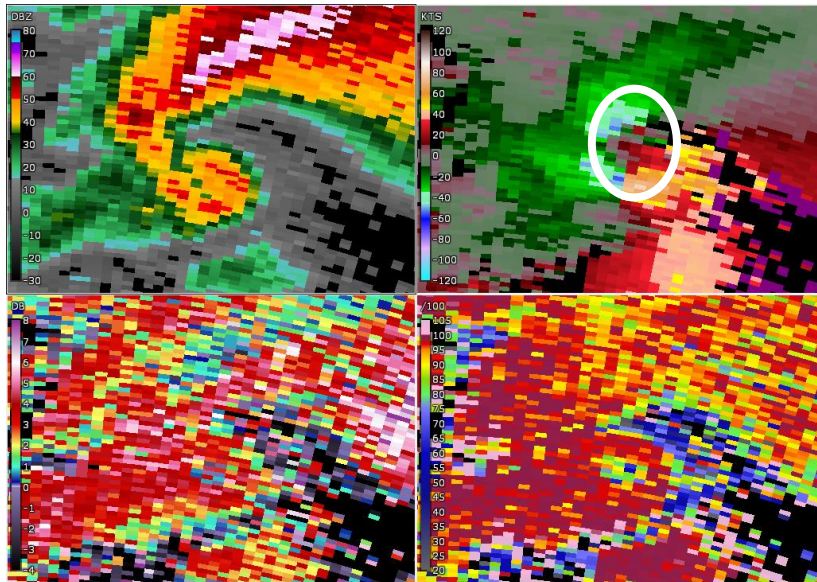


Fig. B-13. Same as Fig. B-9 except for KTWX Topeka, KS May 28, 2013 21:19Z. The estimated storm motion is  $257^\circ$  at 10 kts.

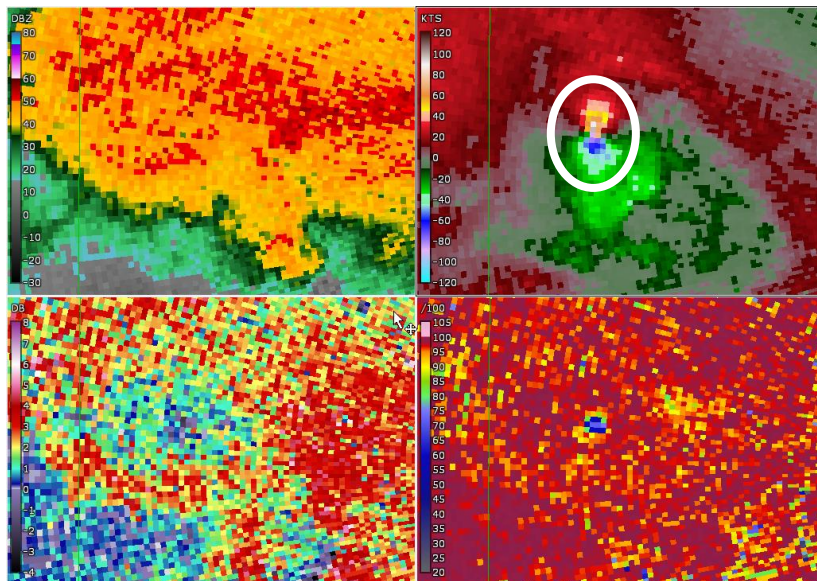


Fig. B-14. Same as Fig. B-9 except for KFSD Sioux Falls, SD June 18, 2014 03:53Z. The estimated storm motion is  $153^\circ$  at 10 kts.

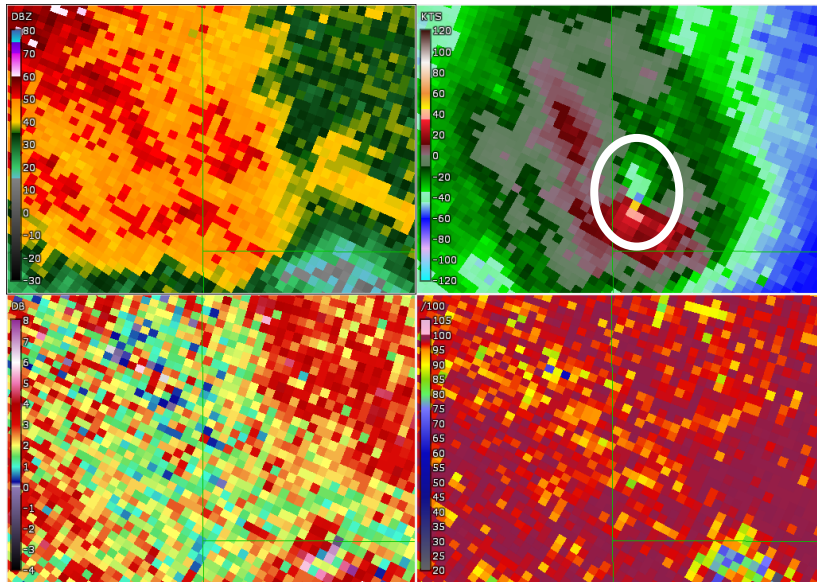


Fig. B-15. Same as Fig. B-9 except for KTWX Topeka, KS September 11, 2015 01:19Z. The estimated storm motion is  $295^\circ$  at 45 kts.

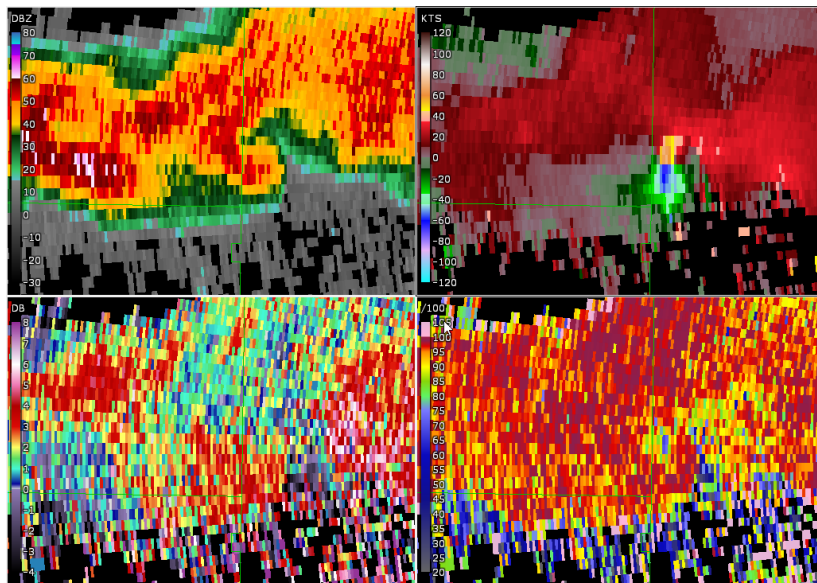


Fig. B-16. Same as Fig. B-9 except for KTWX Topeka, KS May 26, 2016 00:28Z. The estimated storm motion is  $275^\circ$  at 14 kts.

## Appendix C: Summary for Cases in Table 4-1

For the study on the impacts of changing sensitivity, we simulated and analyzed the eight cases listed in Table 4-1. For each case, we simulated data from 20 radar systems having progressively lower sensitivity. Overall, radar data (i.e., three spectral moments and three polarimetric variables) for 160 PPIs were simulated and analyzed for this part of the study. Here, we simply show PPI plots of the WSR-88D data for the cases in Table 4-1 to demonstrate the range of cases from different part of the country that were used in this study. All PPIs are at  $0.5^\circ$  elevation unless noted otherwise.

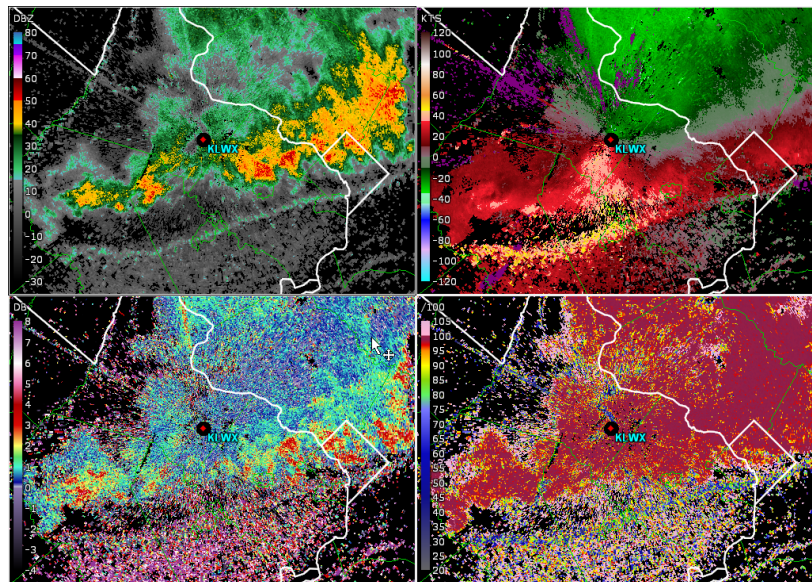


Fig. C-1. Reflectivity (top left), Doppler velocity (top right), differential reflectivity (bottom left), and correlation coefficient (bottom right) for KLWX Sterling, VA July 22, 2017 18:33Z.

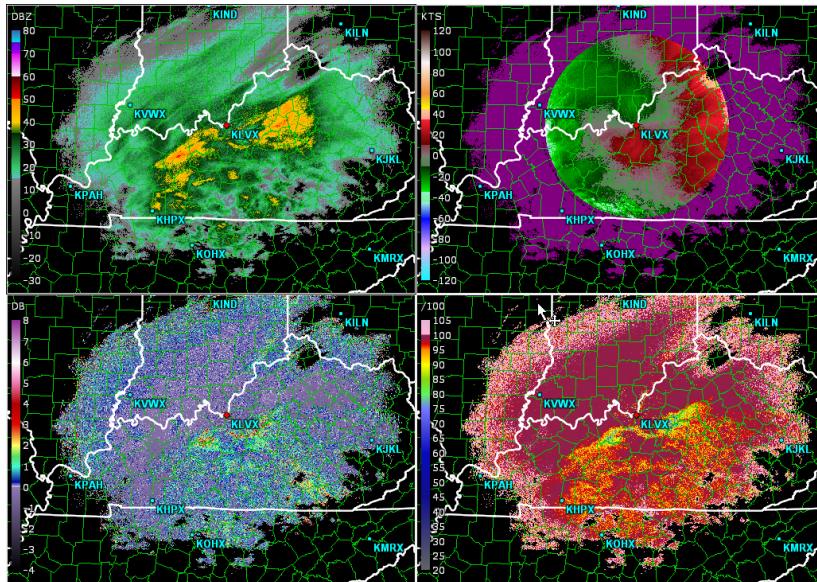


Fig. C-2. Same as Fig. C-1 except for KLVX Louisville, KY March 4, 2015 22:40Z.

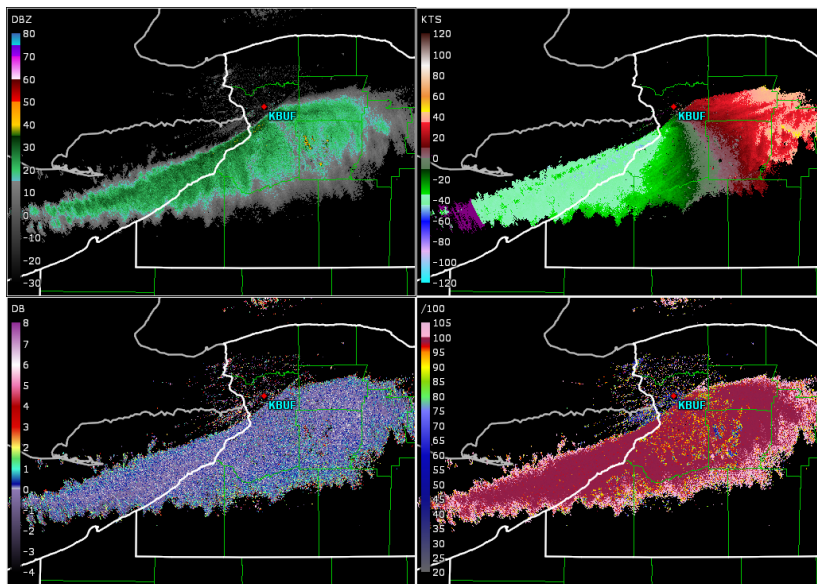


Fig. C-3. Same as Fig. C-1 except for KBUF Buffalo, NY November 18, 2014 20:39Z collected with the short (1.57- $\mu$ s) pulse.

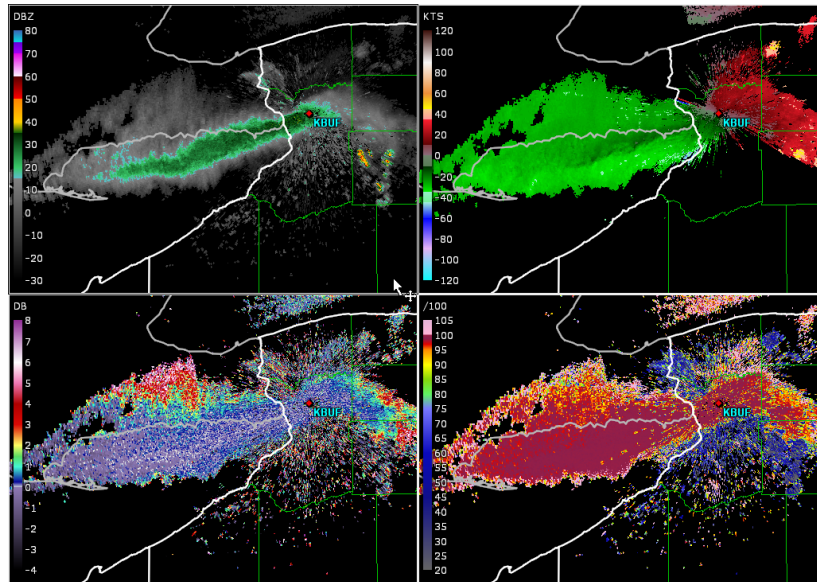


Fig. C-4. Same as Fig. C-1 except for KBUF Buffalo, NY November 19, 2014 12:11Z collected with the long (4.57- $\mu$ s) pulse.

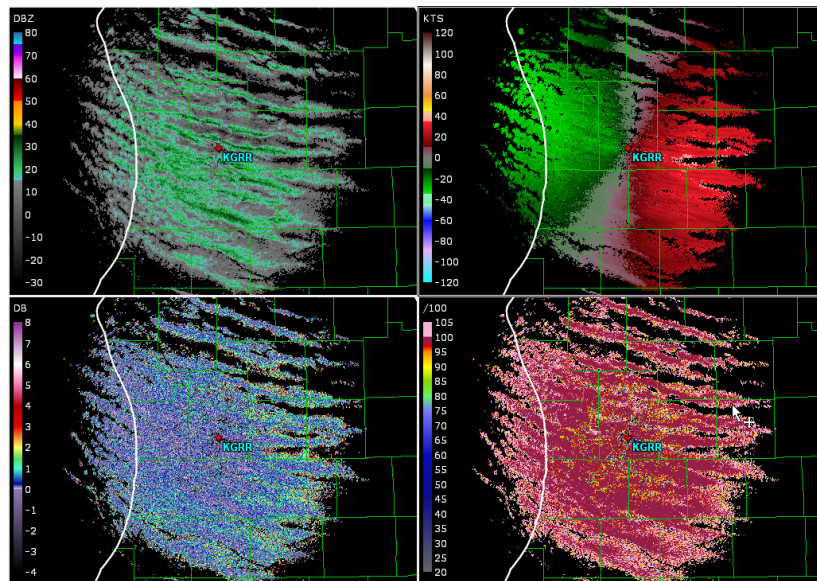


Fig. C-5. Same as Fig. C-1 except for KGRR Grad Rapids, MI January 4, 11:08Z.

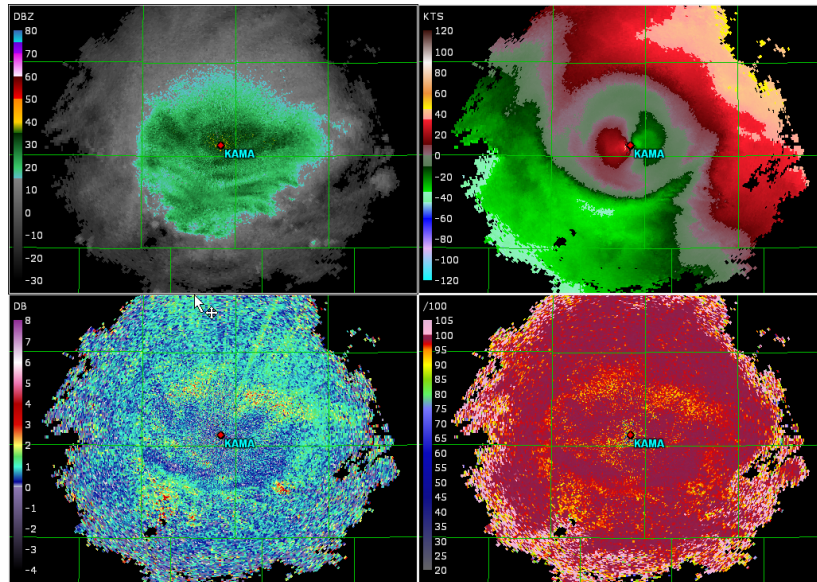


Fig. C-6. Same as Fig. C1 except for KAMA Amarillo, TX January 22, 2015 03:29Z at 4.5° elevation.

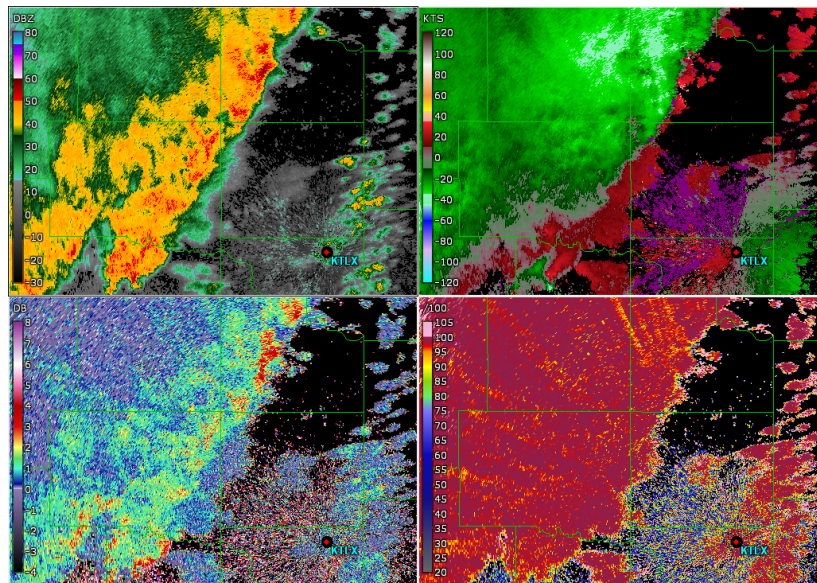


Fig. C-7. Same as Fig. C-1 except for KTLX Norman, OK May 23, 2015 22:19Z.

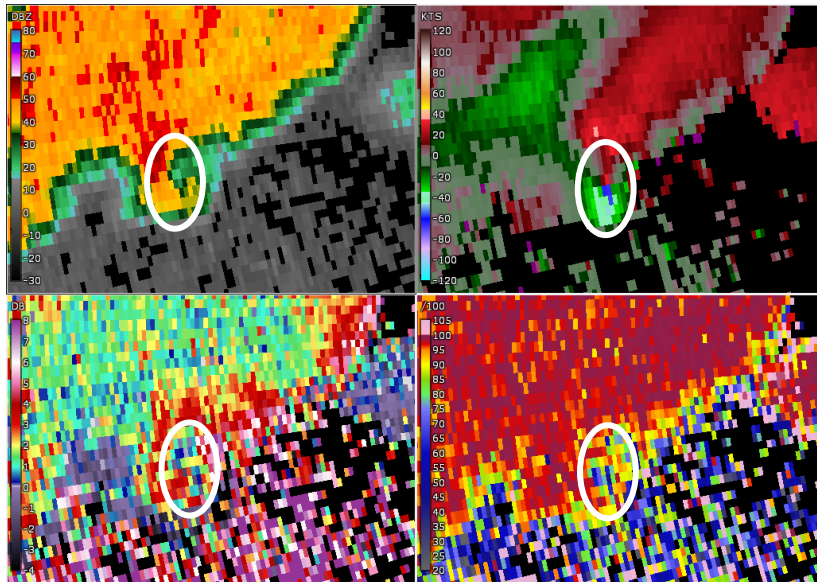


Fig. C-8. Same as Fig. C-7 except zoomed in to focus on the circulation on the leading edge of the storm.

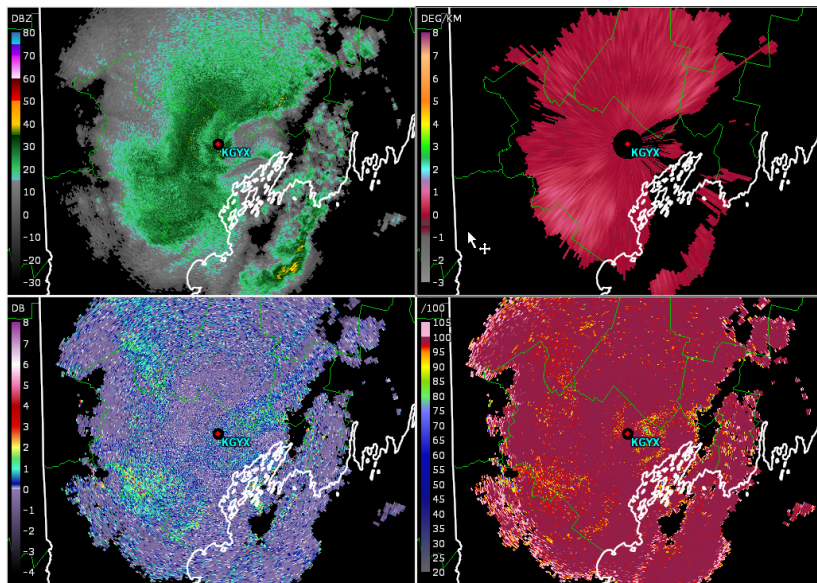


Fig. C-9. Same as Fig. C-1 except for KGYX Portland, ME December 25, 2017 14:57Z.

## **Appendix D: SENSR Preliminary Report**

The preliminary report is included next in its original form.

# **SENSR Data Quality Simulations Antenna Sidelobes: Preliminary Report**

F. Nai, J. Boettcher, D. Schwartzman, C. Curtis, and S. Torres

Cooperative Institute for Mesoscale Meteorological Studies, University of Oklahoma  
and NOAA/National Severe Storms Laboratory

Norman, OK

June 8 2018

## **Executive Summary**

The Spectrum Efficient National Surveillance Radar (SENSR) program is an opportunity to integrate weather and aircraft surveillance capabilities by replacing the aging networks of federally owned, fixed, ground-based radar systems, while making at least 30 MHz of bandwidth in the L band available for auction by 2024. This work qualitatively assesses the impacts of specific radar cost-driving requirements on NOAA/National Weather Service (NWS) mission-critical weather features that affect warning decision making. For this purpose, a robust and flexible simulator was developed: the Signal Processing And Radar Characteristic (SPARC) simulator, which can produce realistic radar data as if they were obtained with radar systems with different designs and performance requirements. In this preliminary study, nine cases involving strong reflectivity gradients were identified and simulated with azimuthal antenna radiation patterns with varying sidelobe levels. By comparing across all cases, we arrived at an antenna radiation pattern with azimuthal sidelobe levels that exceed the current requirements, yet were acceptable for NWS mission-critical decision making. This suggests that it may be possible to relax the antenna radiation pattern requirements in the azimuthal direction for SENSR without impacting the NWS mission. However, a more comprehensive study involving all stakeholders would be needed to determine new requirements. With this in mind, we propose the use of the integrated sidelobe level (ISL) coupled with a maximum sidelobe level as a more relevant way to specify antenna radiation pattern requirements for weather radars.

## **1. Introduction**

The Spectrum Efficient National Surveillance Radar (SENSR) program aims to replace weather and aircraft surveillance capabilities for the aging networks of federally owned, fixed, ground-based radar systems and to make at least 30 MHz of bandwidth in the L band available for auction by 2024. A multi-agency study is being conducted to assess the feasibility of reallocating radar frequencies currently in the L band while addressing cross-agency mission efficiency. One promising candidate to meet the demanding SENSR requirements is a multifunction phased-array radar (MPAR) (Weber et al. 2007). Implementing the NOAA/National Weather Service (NWS) weather-surveillance function using an MPAR lowers maintenance costs, while introducing new capabilities and tradeoffs that depend on the architecture, geometry, and other system design choices. Whereas most of these capabilities and tradeoffs are well understood and can be quantified by experienced radar engineers, communicating radar performance to a diverse set of stakeholders while addressing the impacts to the NWS mission is quite challenging. Simulations can be a useful tool and a natural means to qualitatively convey the impacts of using different radar architectures for weather surveillance. The Signal Processing And Radar Characteristics (SPARC) simulator described by Schwartzman and Curtis (2017) was developed in MATLAB and provides a highly flexible, robust, framework to study the impact of diverse signal processing techniques and radar system characteristics on the radar variables required to support the NWS weather-surveillance mission.

A critical component of the SENSR program is the development of validated functional requirements for the high-resolution weather-surveillance mission to facilitate industry's design of potential solutions. The agencies have developed a Preliminary Performance Requirements (PPR) document largely based on the capabilities of the existing WSR-88D (FAA 2017). As a result,

requirements specific to radars that use more advanced technologies (e.g., phased-array antennas, pulse compression) are either missing, incomplete, or just unclear in the PPR. Furthermore, some of the more stringent requirements in the PPR are likely to be significant cost drivers for SENSAR. We have initially identified specific cost-driving requirements in the PPR that could potentially be refined: angular and range-sidelobe levels, spatial sampling (both azimuthal and range), sensitivity, and dwell time. Herein, we describe the application of the SPARC simulator to qualitatively analyze the impact of adjustments to the azimuthal sidelobe requirements for the antenna radiation pattern, and we present some preliminary conclusions to motivate and justify a more comprehensive study on the angular-sidelobe requirements by the NWS. Section 2 of this report discusses our simulation, case selection, and data analysis methodology. Section 3 presents our detailed analysis for the 3 May 2012 23:50Z case collected by the KBGM radar at Binghamton NY and summaries for other cases. Section 4 discusses our preliminary conclusions.

## **2. Simulation and Analysis Processes**

Simulation is a relatively inexpensive way to perform fair comparisons of different radar systems that meet different performance requirements. The SPARC simulator (Schvartzman and Curtis 2017) is a robust simulator that can be used to study the impacts of signal processing algorithms and system design choices. This preliminary study uses the SPARC simulator to simulate radar data for specific weather events as if they were observed by radars that have different azimuthal antenna radiation patterns with the ultimate goal of determining whether the stringent SENSAR angular-sidelobe requirements can be relaxed while retaining weather features that are important for NWS mission-critical decision making. This section will provide a brief description of the SPARC simulator and the process to simulate antenna radiation patterns, the case selection methodology, and the data analysis process for this study.

### **2.1 Simulation Methodology**

The SPARC simulator consists of a highly flexible framework to study the impact of diverse signal processing techniques and radar system characteristics on radar-variable estimates (i.e., radar base data) required to support the NWS weather-surveillance mission. The SPARC simulator can be used to compare the performance of new techniques with respect to legacy ones, to study the impact of different scanning strategies, or to better understand the data quality implications of adopting different technologies (e.g., phased-array antennas) on radar-variable estimates. A high-level block diagram of the simulation framework is shown in Fig. 1. The SPARC simulator ingests archived WSR-88D radar data from National Center for Environmental Information (NCEI). As the first step, it performs data conditioning, which fills in missing radial velocity and spectrum width estimates and interpolates all fields to produce maps of finely sampled radar variables with the desired azimuthal and range sampling. These fields

and the scanning parameters (e.g., number of samples per dwell, pulse repetition time, and average noise power) are utilized to generate the time-series (also referred to as the IQ data) data corresponding to independent scattering centers. The time-series data for each scattering center represents the total signal backscattered from all the hydrometeors in a volume of space that is, in general, many times smaller than the radar resolution volume. By applying differing antenna radiation patterns and range-weighting functions to the time-series data from the scattering centers, simulated time-series data for each range gate are generated, incorporating the desired radar system and signal characteristics. Thus, radar data corresponding to the same case but observed with differing radar designs can be simulated and studied.

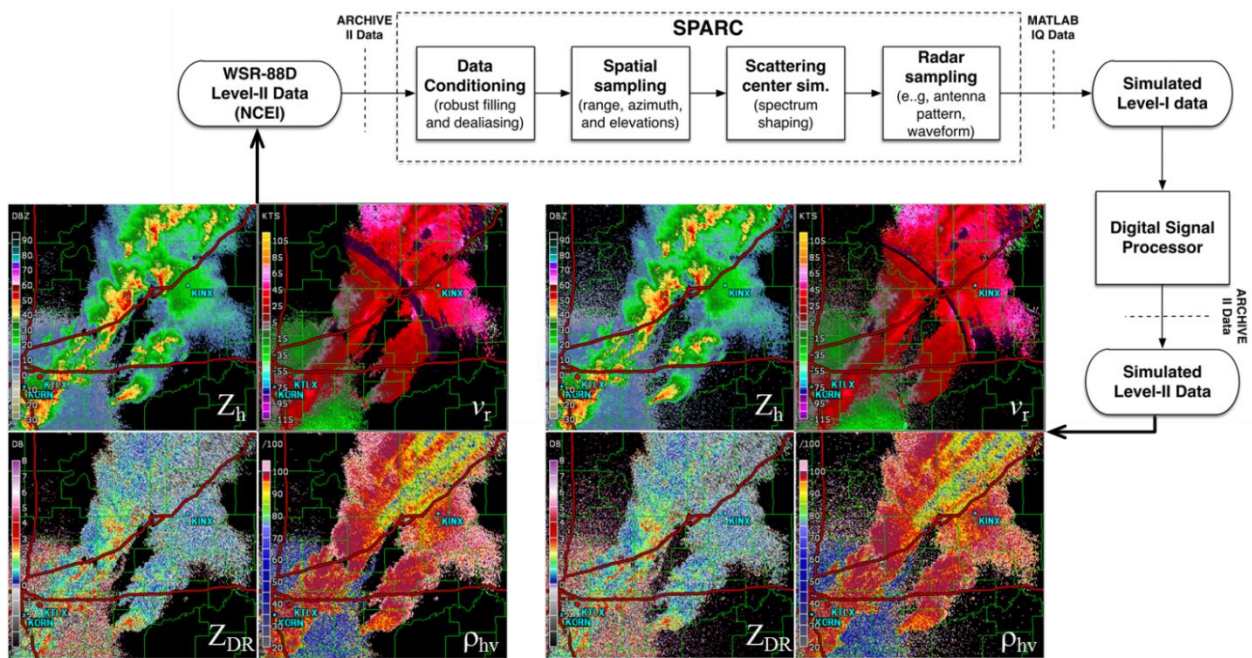


Fig. 1. Simplified block diagram of the SPARC simulator. After data ingestion, a data conditioning function fills in missing data values and de-aliases the velocity field. Then, after the sampling grid is refined based on the range and azimuth samplings defined by the user, the scattering center simulation is carried out. Lastly, radar sampling effects are accounted for, and the SPARC simulator produces time-series data. After processing the data, a suite of radar-variable estimates is produced to simulate fields as would be observed by the desired radar system.

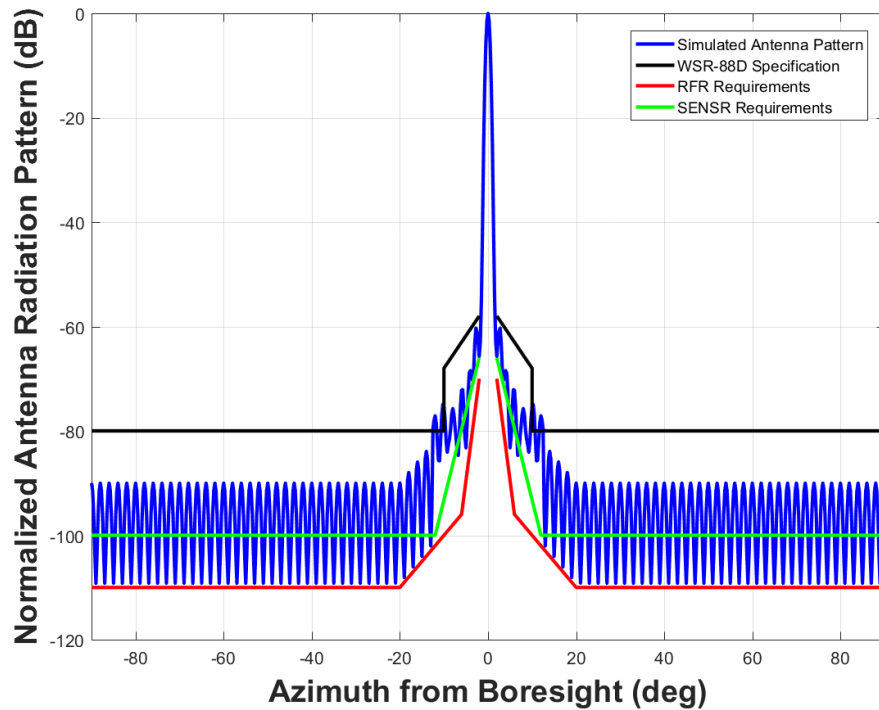


Fig. 2. Example of simulated two-way antenna radiation pattern (blue) with a peak sidelobe level of -60 dB and a far sidelobe level of -90 dB. This simulated pattern meets the WSR-88D specifications (black) but does not meet either the NWS RFR requirements (red) or the SENSR PPR requirements (green).

To simulate antenna radiation patterns, weights were applied to the simulated time-series data for each of the scattering centers. The overall simulated effective antenna radiation pattern is approximated by the convolution of a representative, measured KOUN pattern with the scattering center weights. Fig. 2 shows an example of a simulated effective (two-way) antenna radiation pattern (blue) with a peak sidelobe level of -60 dB and a far sidelobe level of -90 dB. The specifications for the WSR-88D antenna sidelobe levels (black) (ROC 2017), the angular sidelobe requirements in the NWS Radar Functional Requirements (RFR) (red) (NWS 2015), and the angular sidelobe requirements in the SENSR PPR (green) (FAA 2017) are plotted as references. In this example, the simulated antenna radiation pattern lies almost completely below the WSR-88D specification but does not meet either the NWS RFR or the SENSR PPR

requirements. In this study, we simulated radar data for the same weather event as if it were collected by radar systems with different antenna radiation patterns to qualitatively assess the impact of different azimuthal sidelobe levels on the quality of the NWS mission-critical features for several weather events.

## **2.2 Case Selection Methodology**

While this report focuses on results from azimuthal-sidelobe contamination, the following case selection process was used for all the cases selected based on the identified cost-driving requirements. A total of 55 weather “cases” were carefully selected for requirement analysis. The term “case” represents a specific radar, elevation and time step identified for simulation purposes. For some weather events, multiple time steps were used. For example, during a long duration Lake Effect Snow event, the NWS Buffalo office used both a short pulse VCP (212) and a long pulse VCP (31). A representative time step from each of these VCPs was chosen for simulation, thus there were two cases from this single event.

There were two guiding principles for Case Selection. First, the event had to present a type of weather hazard with sufficient threat to require a NWS warning or advisory (e. g., severe convection or winter) decision or localized Decision Support (e. g., wildfire). Second, the radar signature(s) had to highlight, or stress, the specific cost-driving requirement. For example, in order to explore the requirements for azimuthal antenna sidelobe contamination, the selected cases had extreme reflectivity gradients in the azimuthal direction. The nine cases selected for azimuthal antenna sidelobe simulations are summarized in Table 1 and Appendix A.

Table 1. Time and location of cases selected to evaluate azimuthal antenna sidelobes levels.

<b>Time</b>	<b>Elevation</b>	<b>Location</b>
3 May 2012 23:50Z	0.9°	KBGM, Binghamton, NY
3 May 2012 23:58Z	0.5°	KBGM, Binghamton, NY
30 July 2013 22:12Z	19.5°	KGLD, Goodland, KS
30 July 2013 21:40Z	0.5°	KGLD, Goodland, KS
7 May 2016 00:36Z	0.5°	KCBX, Boise, ID
7 May 2016 00:18Z	0.5°	KCBX, Boise, ID
12 June 2017 22:58Z	1.2°	KAMA, Amarillo, TX
12 June 2017 22:42Z	1.2°	KAMA, Amarillo, TX
12 June 2017 22:58Z	0.8°	KAMA, Amarillo, TX

For both Case Selection and Qualitative Simulation Analysis, the radar images were displayed using Gibson Ridge Level 2 Analyst (GR2). GR2 is used by a large number of weather professionals and enthusiasts. This includes NWS forecasters, who use GR2 as a supplement for routine forecasting, severe weather warning operations, post-event analysis, and decision support deployments. It is the one of the best tools for viewing the raw (Level II) radar data generated by the WSR-88D Radar Data Acquisition (RDA) unit. Level II data are readily available at the NCEI for any WSR-88D, allowing for maximum flexibility for case selection.

### **2.3 Simulation Analysis Methodology**

For each case, multiple simulations, each with a different antenna radiation pattern (shown in Appendix B), were presented to the meteorologist. The Simulation Analysis process had two guiding principles. The first goal was to place each of the simulations into one of three possible categories: acceptable, marginal, and unacceptable. The assignment to these categories is dependent on whether or not the NWS mission-critical threat is clearly present in the radar signature. The second guiding principle was that the simulations were presented blindly to the meteorologist, that is, the underlying settings (e.g., different antenna radiation patterns) were not revealed to the meteorologist a priori. This was to prevent any bias in the analysis.

The Simulation Analysis results included a table identifying which simulation(s) fall within the acceptable, marginal, and unacceptable categories. As needed, supplementary information was provided for essential context. This included the specific threat type for the case (damaging wind, heavy snow, etc.), along with the radar data that were most important for identifying the threat. For example, when examining angular sidelobe contamination simulations, spectrum width and radial velocity fields were often the data fields with potentially confusing signatures that could affect an NWS decision maker.

On the current NWS operational system, the Dual Polarization Level II data (differential reflectivity, differential phase, and correlation coefficient) are first preprocessed at the Radar Product Generator (RPG). The RPG Preprocessor smooths and recombines the Dual Polarization base data before product generation. It is unknown at this time what type of downstream data processing would exist for future systems; thus, the analysis for this study was based on the Level II raw radar data. This made the simulation analysis more challenging, especially for areas with low Signal-to-Noise Ratio (SNR).

### 3. Simulation Results

The Binghamton, NY, KBGM case drove the initial evolution of our simulation methodology; therefore, its simulation results are discussed in detail here. Fig. 3 shows the reflectivity, radial velocity, spectrum width, and correlation coefficient fields of a storm observed by the KBGM radar at 23:50Z on 3 May 2012 at 0.9° elevation. The storm, located near 295° azimuth and 28 nm away from the radar, has a strong hail core with a peak reflectivity of 70 dBZ. Near the hail core, there is a gust front at 300° azimuth with a peak reflectivity of 21 dBZ. Between the gust front and the hail core is a clear-air gap with a peak reflectivity of 14 dBZ. This gap supports the conceptual model of a gust front, providing the essential data cue for the warning forecaster that the leading edge of potentially damaging outflow wind needs to be assessed. It is possible that relaxing the angular-sidelobe requirements would result in azimuthal sidelobe contamination that would obscure this clear-air gap that separates the gust front from the main storm. Accurately identifying the leading edge of a potentially damaging gust front wind is essential to NWS warning services.

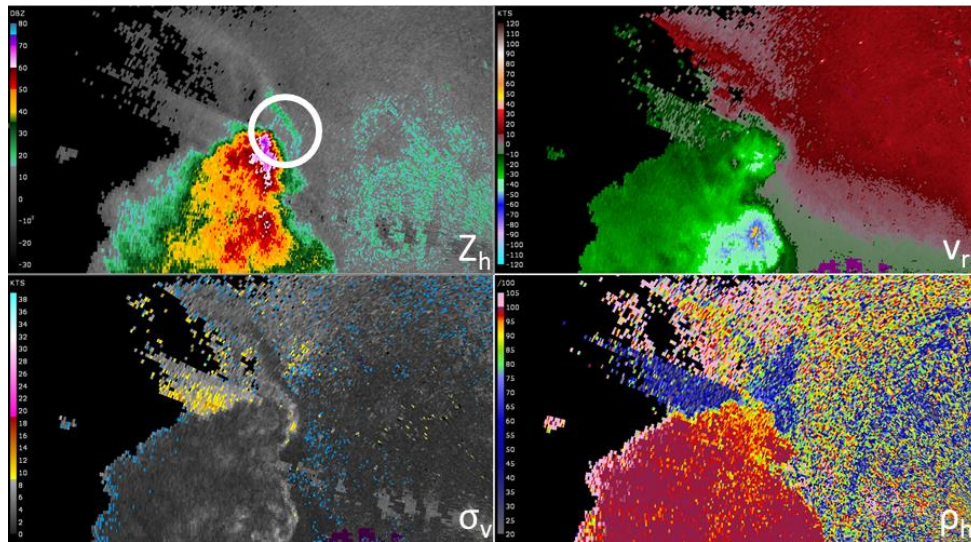


Fig. 3. Reflectivity ( $Z_h$ ), radial velocity ( $V_r$ ), spectrum width ( $\sigma_v$ ), and correlation coefficient ( $\rho_{hv}$ ) of a storm observed by KBGM at 23:50Z on 3 May 2012 at 0.9° elevation. There is a strong hail core (70 dBZ) with giant hail (2.75") on the ground that is located near a gust front in the circled area. Angular sidelobe contamination can easily obscure the clear-air gap between the gust front and the main storm.

Fig. 4 shows a simulation of this case with an antenna radiation pattern that has a peak azimuthal sidelobe level of -50 dB and far azimuthal sidelobe levels of -80 dB. The contamination caused by these higher sidelobe levels can be clearly seen in the fields of reflectivity, radial velocity, and spectrum width. The clear-air gap in reflectivity is partially filled in with reflectivity values above 15 dBZ. Significant velocity estimation errors are present in the clear-air region located to the northeast of the gust front. These false inbound velocity estimates are due to sidelobe contamination from the hail core overpowering the original weather signal. Since the hail core has inbound (negative) radial velocities and the area near the gust front has outbound (positive) radial velocities, the sidelobe contamination from the hail core results in a bimodal spectrum, which leads to the large spectrum width estimates seen in the circled area in the bottom left panel of Fig 4. The higher number of zero estimates for spectrum width is the result of using only the conventional spectrum width estimator in our digital signal processing toolkit instead of the improved hybrid spectrum width estimator currently used by the WSR-88D. This simulated data clearly places the corresponding simulated antenna radiation pattern in the unacceptable category.

Fig.5 shows a simulation of the KBGM case that was classified in the marginal category. In this example, the simulated antenna radiation pattern has a peak sidelobe level of -60 dB and far sidelobe levels of -90 dB. In comparison with Fig. 4, there is almost no sidelobe contamination filling in the clear-air gap between the hail core and the gust front reflectivity. However, there are still erroneous inbound velocity estimates in the clear-air region beyond the gust front, and there are still areas with large spectrum width estimates. The lower sidelobe levels reduced the amount of contamination but the resultant data quality is compromised and could lead to inaccurate threat assessment by an NWS decision maker.

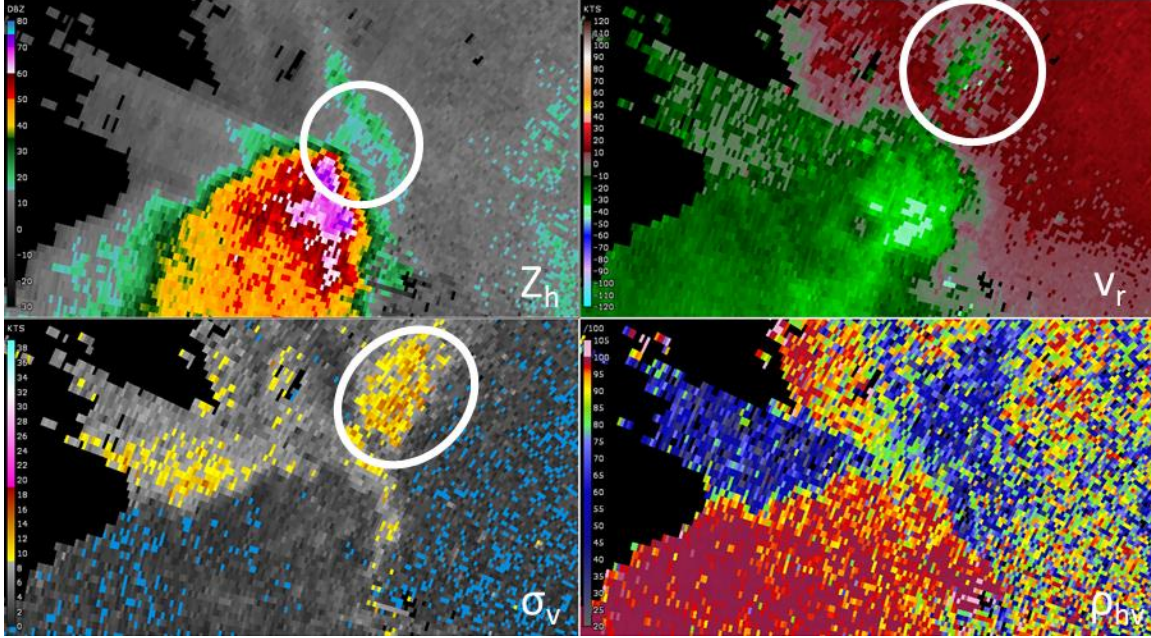


Fig. 4. Example of unacceptable simulated reflectivity ( $Z_h$ ), radial velocity ( $V_r$ ), spectrum width ( $\sigma_h$ ), and correlation coefficient ( $\rho_{hv}$ ) for the same time step shown in Fig. 3. The simulated antenna radiation pattern has a peak sidelobe level of -50 dB and a far sidelobe level of -80 dB. The higher sidelobe levels lead to clearly visible contamination in the reflectivity, radial velocity, and spectrum width in the circled area.

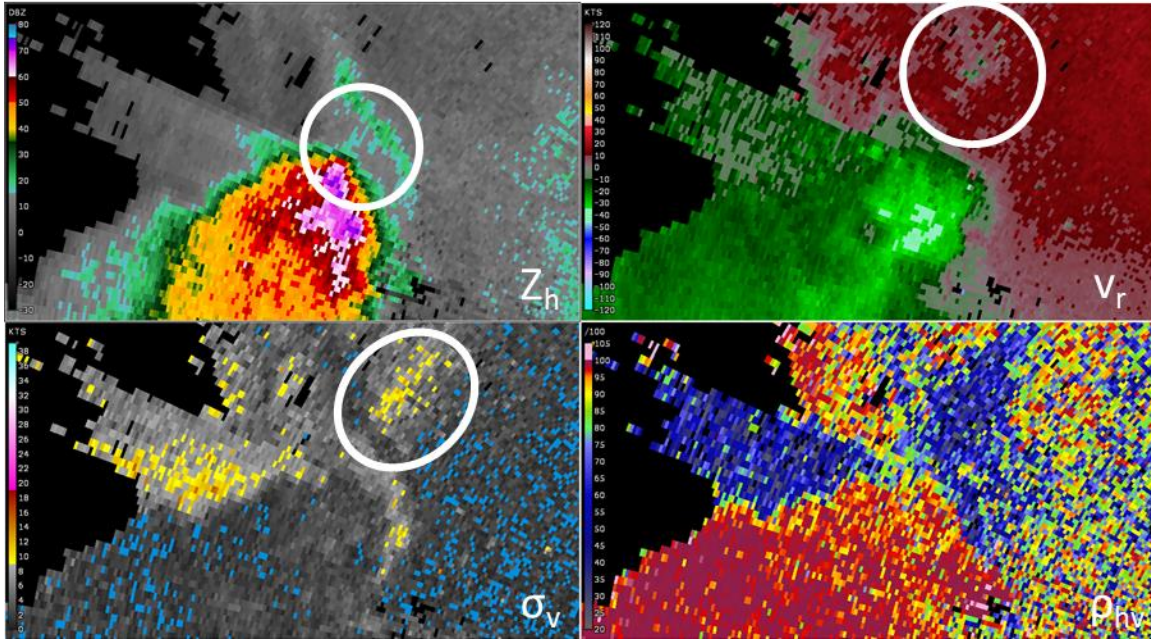


Fig. 5. Example of marginal simulated reflectivity ( $Z_h$ ), radial velocity ( $V_r$ ), spectrum width ( $\sigma_h$ ), and correlation coefficient ( $\rho_{hv}$ ) for the same time step shown in Fig. 3. The simulated antenna radiation pattern has a peak sidelobe level of -60 dB and a far sidelobe level of -90 dB. Since the sidelobe levels are lower than that of Fig. 4, the contamination in velocity and spectrum width are reduced but not eliminated.

Fig. 6 shows a simulation of the KBGM case that was classified in the acceptable category. In this example, the simulated antenna radiation pattern has a peak sidelobe level of -60 dB and far sidelobe levels of -100 dB. Compared to Fig. 4 and Fig. 5, there is no readily apparent sidelobe contamination in the circled area. In addition, there is no data quality deterrent that could lead to an inaccurate threat assessment by an NWS decision maker.

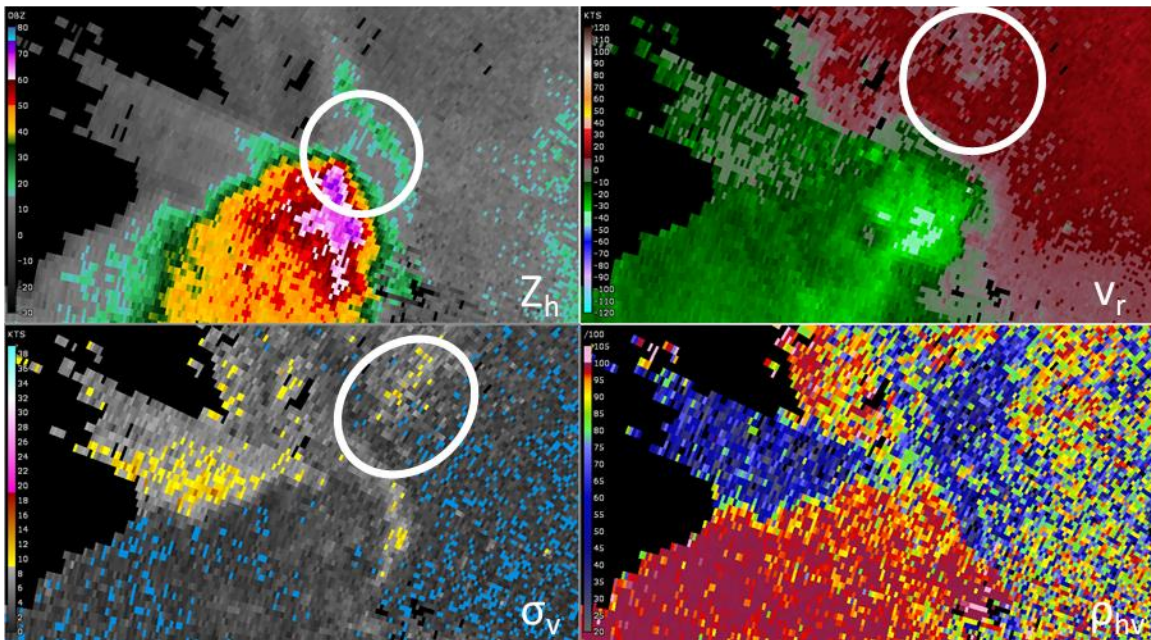


Fig. 6. Example of acceptable simulated reflectivity ( $Z_h$ ), radial velocity ( $V_r$ ), spectrum width ( $\sigma_h$ ), and correlation coefficient ( $\rho_{hv}$ ) for the same time step shown in Fig. 3. The simulated antenna radiation pattern has a peak sidelobe level of -60 dB and a far sidelobe level of -100 dB. The sidelobe contaminations present does not negatively impact interpretation of the data.

Fig. 4, 5, and 6 are representative examples of simulated data that are in the unacceptable, marginal, and acceptable categories, respectively. For each case identified in Table 1 (section 2.2), 16 different simulations with systematically varied azimuthal antenna sidelobe levels were produced and analyzed. Table 2 shows the analysis results for the KBGM 3 May 2012 23:50Z case. The first column of Table 2 is a label used to identify the simulated antenna radiation patterns used for a particular simulation experiment. The second column shows the one-way integrated sidelobe levels (ISL) for the effective antenna radiation patterns simulated, which serve

as a quantitative measure of the overall sidelobe levels for a simulated antenna radiation pattern. For our simulations, the ISL is the numerical integration (i.e., the approximate area under the curve) of the simulated antenna radiation pattern (example shown in Fig. 2) from  $-90^\circ$  to  $-2^\circ$  and from  $2^\circ$  to  $90^\circ$  about the antenna pointing direction<sup>1</sup>. The color of each row in Table 2 indicates whether that simulated data was found to be acceptable (green), marginal (yellow), or unacceptable (red). For the other eight cases, simulations with the same parameters as the KBGM 3 May 2012 23:50Z case were presented to the meteorologist with different ordering. The simulations were ordered to deliberately avoid a systematic degradation in the simulated antenna radiation pattern that could lead to biases in the analysis of the data quality. The individual case results were similar, though the individual case analysis tables are not shown here.

Table 2. Simulation and analysis results for 3 May 2012 23:50Z.

Simulated Pattern	Integrated Sidelobe Level (dB)
A	-21.38
B	-20.39
C	-21.67
D	-23.04
E	-19.07
F	-22.08
G	-20.12
H	-18.07
I	-17.69
J	-16.06
K	-23.94
L	-24.62
M	-22.61
N	-18.65
O	-19.44
P	-23.78

<sup>1</sup> We approximated the simulated antenna radiation pattern using a measured KOUN antenna radiation pattern with limited spatial extension (between  $\pm 13^\circ$ ) as a proxy for the full (between  $\pm 180^\circ$ ) WSR-88D antenna radiation pattern. We estimate that using the full WSR-88D pattern could result in slightly larger ISL (no more than 2 dB for far sidelobes and no more than 0.5 dB overall) for all simulated antenna radiation patterns.

Table 3 is a summary of all the cases showing the number of cases that were placed into the acceptable category for each simulated antenna radiation pattern, sorted by decreasing integrated sidelobe level. Our results show that lowering the ISL to below -23 dB resulted in acceptable data quality for all nine cases simulated.

Table 3. Number of cases where the simulated antenna radiation pattern resulted in acceptable data quality

<b>Simulated Pattern</b>	<b>Integrated Sidelobe Level (dB)</b>	<b>Num. of Acceptable Cases</b>
J	-16.06	2
I	-17.69	3
H	-18.07	3
N	-18.65	4
E	-19.07	5
O	-19.44	5
G	-20.12	4
B	-20.39	6
A	-21.38	7
C	-21.67	6
F	-22.08	8
M	-22.61	8
D	-23.04	9
P	-23.78	9
K	-23.94	9
L	-24.62	9

Based on analyses of all nine cases identified in section 2.2, we determined a simulated antenna radiation pattern (shown in Fig. 7, Pattern D in Table. 3) that resulted in acceptable data quality for all cases and had the highest integrated sidelobe level. Recall that allowing antenna radiation patterns with higher sidelobe levels could result in radar systems with lower cost. This simulated antenna radiation pattern (blue) has a peak sidelobe level of -60 dB and far sidelobe levels of -100 dB. The entire simulated pattern lies below the WSR-88D antenna-sidelobe specifications (black) but exceeds the NWS RFR requirements (red). The far sidelobes of this

simulated antenna radiation pattern meet the SENSr PPR requirements (green), but its sidelobes between  $2^\circ$  and  $20^\circ$  exceed it. This suggests that **it is possible to relax the SENSr azimuthal sidelobe requirements while retaining sufficient data quality for NWS warning decision making**. Whereas this is a preliminary study with a limited number of cases, it presents a clear justification for a more comprehensive study involving a larger group of forecasters looking at simulated data for additional cases, just as studies and assessments were conducted before the dual-polarization upgrade for the WSR-88D.

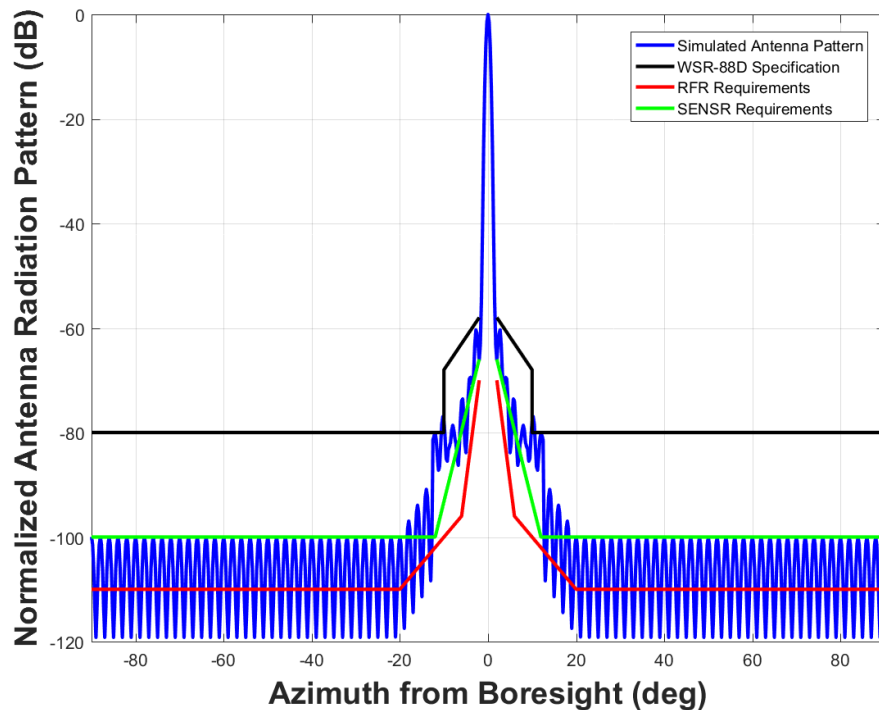


Fig. 7. Simulated antenna radiation pattern (blue) with a peak sidelobe level of -60 dB, a far sidelobe level of -100 dB and an integrated sidelobe level of -23.04 dB. This simulated pattern meets the WSR-88D specifications (black) but does not meet the NWS RFR requirements (red) or the SENSr PPR requirements (green).

Table 3 shows a clear correlation between the ISL and the number of cases with acceptable data quality. Since the ISL is a summation of the antenna radiation pattern over azimuth angles from  $\pm 90^\circ$  to  $\pm 2^\circ$ , it can be broken down into two components: near ISL (from  $\pm 2^\circ$  to  $\pm 20^\circ$ ) and far ISL (from  $\pm 20^\circ$  to  $\pm 90^\circ$ ). The near sidelobes usually have higher peaks, and therefore, a

conservative envelope specifying the maximum sidelobe levels is needed since any individual sidelobe with a high peak could induce significant errors to the radar-variable estimates. While the near ISL is the most significant contributor to the overall ISL, the effects of far ISL in determining the data quality cannot be ignored, especially in cases where there are widespread weather echoes far away from the main lobe. Using Fig. 7 as an example, the far ISL for the simulated antenna radiation pattern (blue) is -31.25 dB while the far ISL for the envelopes specifying the SENSR PPR requirements (green) and RFR requirements (red) are -28.54 dB and -33.54 dB, respectively. The difference (2.7 dB) between the far ISL for the SENSR PPR requirement and the simulated antenna radiation pattern means that there could be antenna radiation patterns that meet the SENSR PPR requirements yet produce marginal or unacceptable data quality. On the other hand, the far ISL of the simulated antenna radiation pattern shown in Fig. 7 is equal to the far ISL of a hypothetical flat envelope with a far sidelobe level of -105 dB between  $\pm 90^\circ$  and  $\pm 20^\circ$ . Using this hypothetical flat envelope to define the far sidelobe requirements would guarantee acceptable data quality, but it appears to be overly stringent and would make the simulated antenna radiation pattern shown in Fig. 7 to fail meeting the requirements. This example shows that the far ISL is more robust at capturing the integrated effects of the far sidelobes compared to flat envelopes. Furthermore, the current SENSR PPR requirements allow individual far sidelobes to exceed the flat envelope as long as the average of that particular sidelobe with its neighboring sidelobes is below the envelope, suggesting that integrated effects for these far sidelobes are more important than the amplitudes of individual sidelobe levels. These observations suggest that, **for the far sidelobes (between  $\pm 20^\circ$  and  $\pm 90^\circ$ ), the ISL coupled with a maximum sidelobe level is a more relevant way to specify antenna-sidelobe requirements for weather radars.**

#### **4. Preliminary Conclusions**

We have been using the SPARC simulator to study the impact of antenna-sidelobe requirements on data quality. To date, nine cases involving strong reflectivity gradients were identified and used in this study. For each case, we simulated antenna radiation patterns with different peak and far azimuthal sidelobe levels and analyzed the corresponding simulated data to determine whether the change in azimuthal radiation pattern resulted in acceptable, marginal, or unacceptable data quality. By comparing across all cases, we obtained an antenna radiation pattern whose azimuthal sidelobes exceeded the SENSr PPR and NWS RFR requirements, yet produced data that were acceptable for NWS mission-critical decision making. This suggests that it is possible to relax the SENSr's antenna radiation pattern requirements in the azimuthal direction. However, a more comprehensive study would be required to determine the new requirements. With this in mind, we propose the ISL coupled with a maximum sidelobe level as a more relevant way to specify antenna radiation requirements for weather radars.

Our next step will focus on expanding the simulator to incorporate the effects of two-dimensional antenna radiation patterns. Since the WSR-88Ds sample a finite set of elevation angles, filling elevation gaps with weather data to produce realistic simulations is a challenge. However, this will allow us to study the impact of elevation sidelobes on data quality. Also, because a planar phased-array antenna produces radar beams with variable beamwidth, we will study the impacts of different spatial sampling schemes on data interpretation and decision making. Finally, we will look into the impacts of other cost-driving requirements, such as sensitivity and dwell time.

## Appendix A: Case Summaries

Strong hail cores typically present sharp azimuthal reflectivity gradients that can result in significant antenna sidelobe contamination. Some of the cases selected contained azimuthal sidelobe contamination in the original WSR-88D data, while others did not (despite significant reflectivity gradients). The cases included in the analysis, which are illustrated in this appendix, were chosen to test the effects of azimuthal sidelobe contamination on a variety of reflectivity gradients. The impact of azimuthal sidelobe contamination is evaluated in terms of the NWS decision maker's ability to recognize this data quality problem from an operational perspective, where radar data interpretation must occur in real time. Thus, any contamination of important weather features that could confuse the NWS decision maker was rated as unacceptable because degraded data quality compromises timely warnings that are the core of the NWS mission.

The reflectivity field observed by the WSR-88D for each simulated case is shown below.

Case 1:

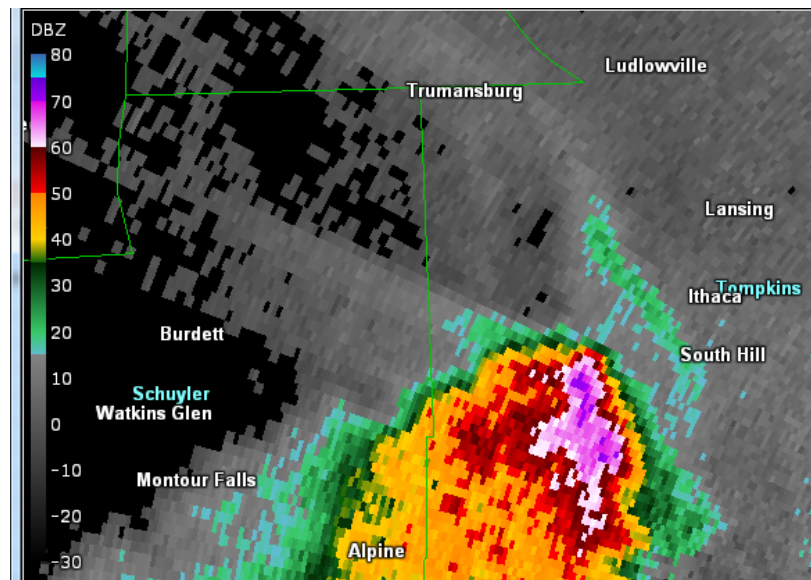


Fig. A.1. 3 May 2012 23:50Z, 0.9°, KBGM, Binghamton, NY, This storm presents a strong hail core and reflectivity gradient, with a gust front just ahead of the storm core. There is little sidelobe contamination at this time step. Retaining the crucial clear air gap for gust front identification makes this an important case for sidelobe analysis.

Case 2:

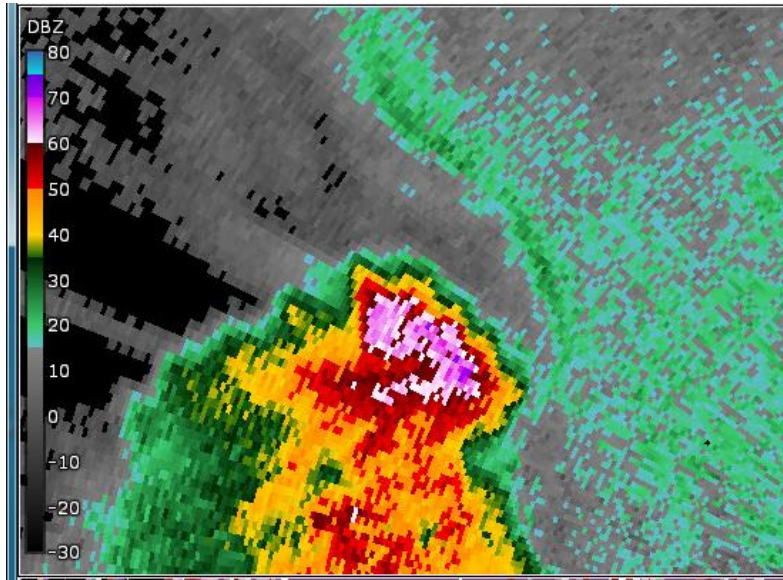


Fig. A.2. 3 May 2012 23:58Z, 0.5°, KBGM, Binghamton, NY. Eight minutes later (Case 1) and at a lower elevation angle, the reflectivity gradient has relaxed just enough for no sidelobe contamination within the gap.

Case 3:

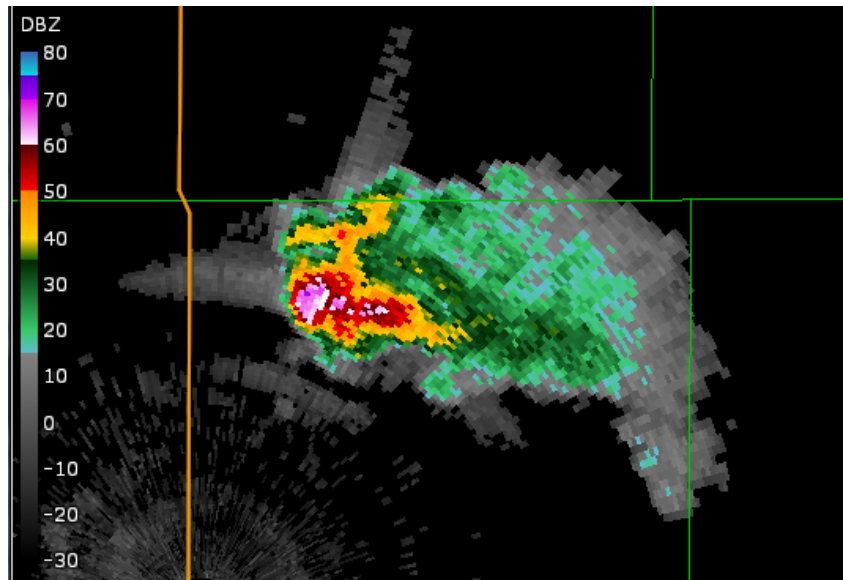


Fig. A.3. 30 July 2013 22:12Z, 19.5°, KGLD, Goodland, KS. This storm presented a strong reflectivity gradient with a sidelobe spike, as well as a Three Body Scatter Spike (which is an artifact that is helpful for NWS decision makers).

Case 4:

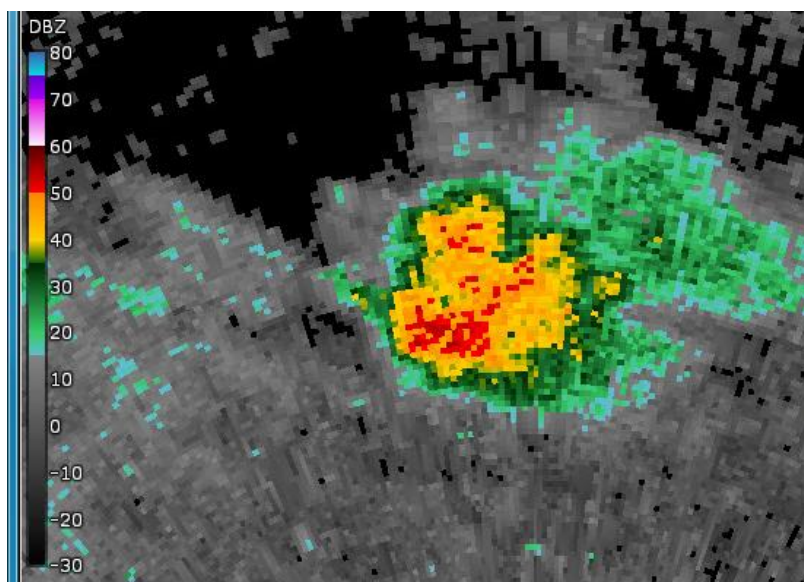


Fig. A.4. 30 July 2013 21:40Z, 0.5°, KGLD, Goodland, KS. This is the same storm, early in its evolution. We wanted to test a storm with no sidelobe contamination.

Case 5:

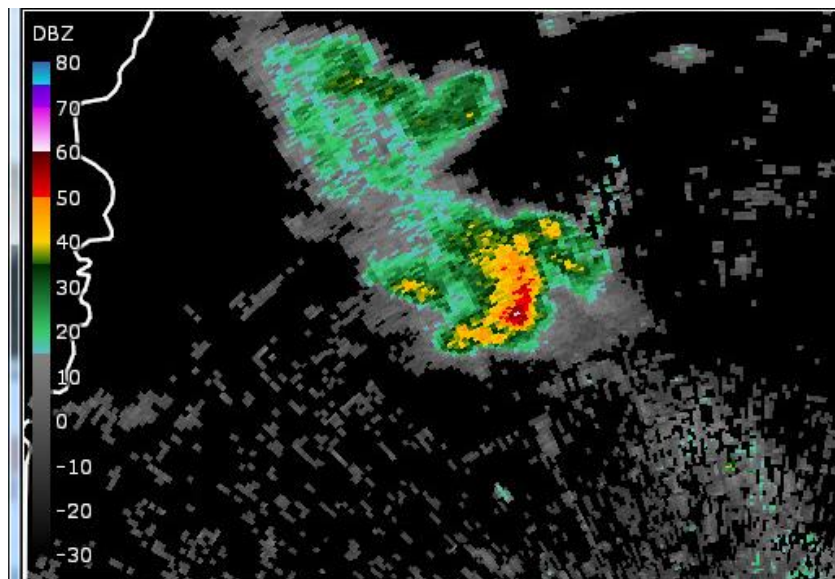


Fig. A.5. 7 May 2016 00:18Z, 0.5°, KCBX, Boise, ID. This is the time step before the onset of sidelobe contamination.

Case 6:

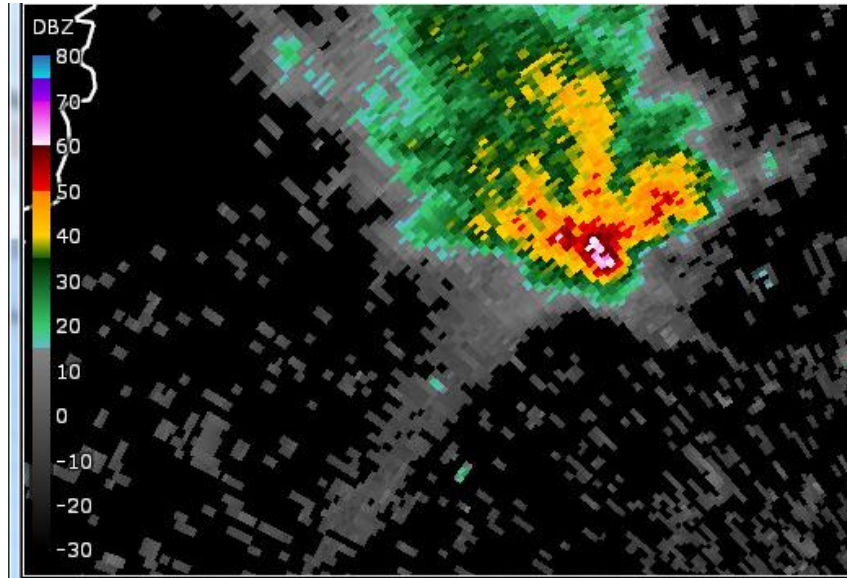


Fig. A.6. 7 May 2016 00:36Z, 0.5°, KCBX, Boise, ID. Same storm as Case 5, with significant sidelobe contamination present at this time.

Case 7:



Fig. A.7. 12 June 2017 22:42Z, 1.2°, KAMA, Amarillo, TX. The storm is located southeast of the radar at a range of approximately 55 nm, with a strong reflectivity gradient and minor sidelobe contamination.

Case 8:

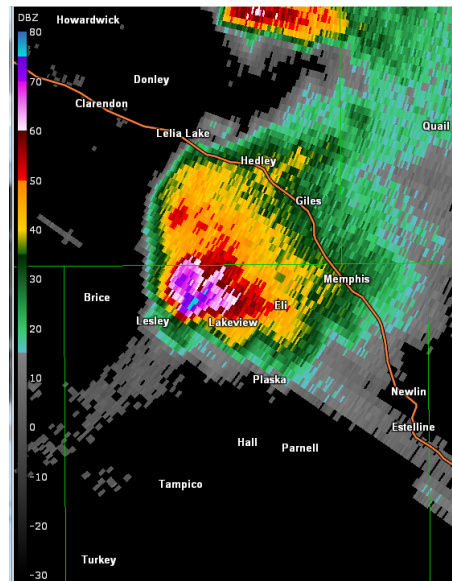


Fig. A.8. 12 June 2017 22:58Z, 1.2°, KAMA, Amarillo, TX. Same storm as Case 7 but 16 minutes later with very strong hail core and significant sidelobe contamination.

Case 9:

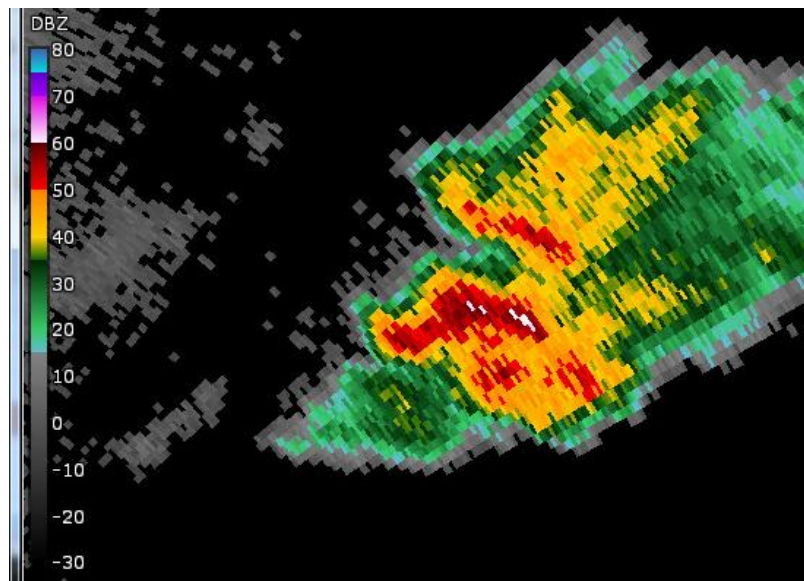


Fig. A.9. 12 June 2017 22:58Z, 0.8°, KAMA, Amarillo, TX. This is a different storm at the same time step as Case 8, located northeast of the radar at a range of approximately 44 nm.

## Appendix B: Simulated Antenna Patterns

To qualitatively evaluate the impact of azimuthal antenna-sidelobe requirements on data quality, 16 ~~azimuthal~~ azimuthal antenna radiation patterns with varying sidelobe levels were produced and their impacts were simulated for each case. The antenna radiation patterns applied in the simulations are presented here in the order of decreasing integrated sidelobe level (ISL).

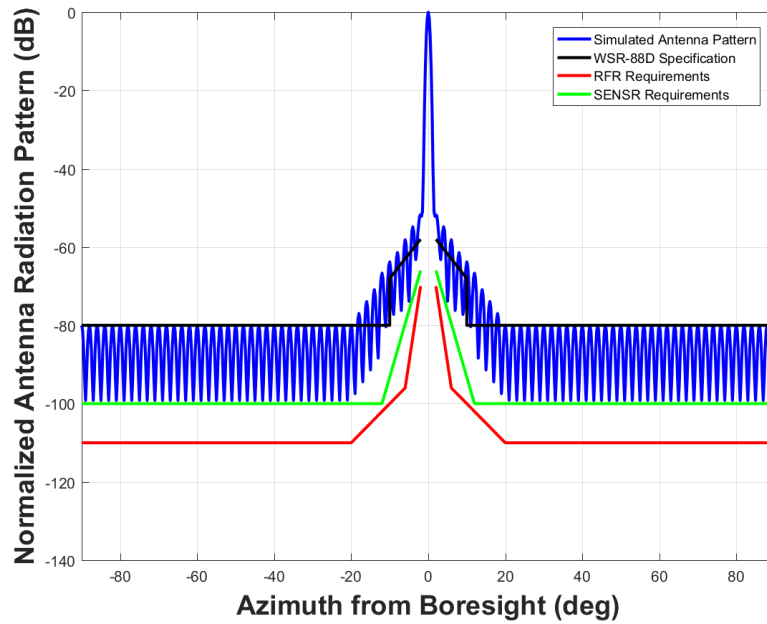


Fig. B.1 Simulated antenna radiation pattern (J in Table 3) with a peak sidelobe level of -52.2 dB, a far sidelobe level of -80 dB, and an integrated sidelobe level of -16.06 dB.

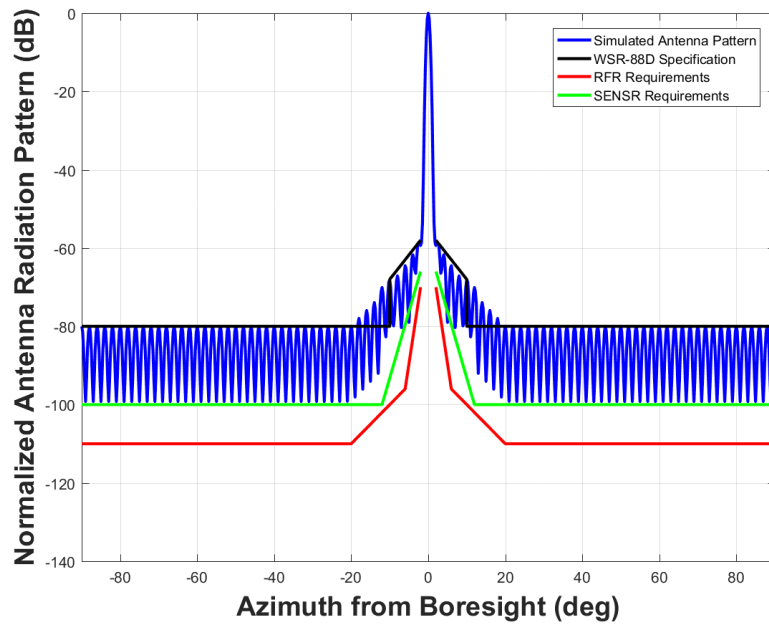


Fig. B.2 Simulated antenna radiation pattern (I in Table 3) with a peak sidelobe level of -58.5dB, a far sidelobe level of -80 dB, and an integrated sidelobe level of -17.69 dB.

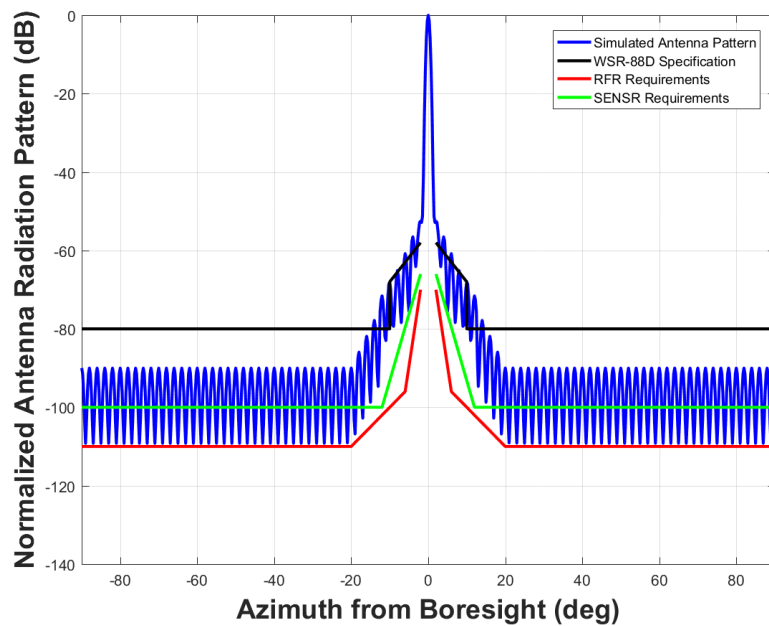


Fig. B.3 Simulated antenna radiation pattern (H in Table 3) with a peak sidelobe level of -52.8 dB, a far sidelobe level of -90 dB, and an integrated sidelobe level of -18.07 dB.

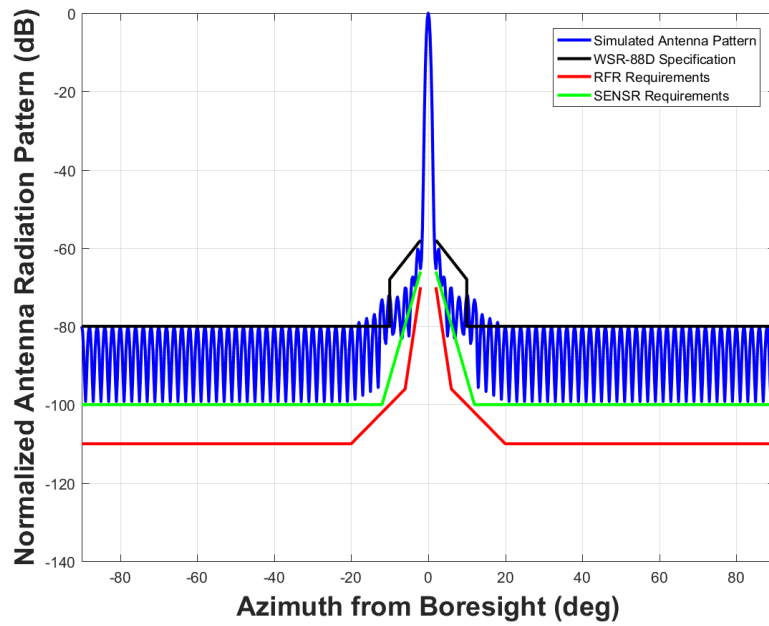


Fig. B.4 Simulated antenna radiation pattern (N in Table 3) with a peak sidelobe level of -60.2 dB, a far sidelobe level of -80 dB, and an integrated sidelobe level of -18.65 dB.

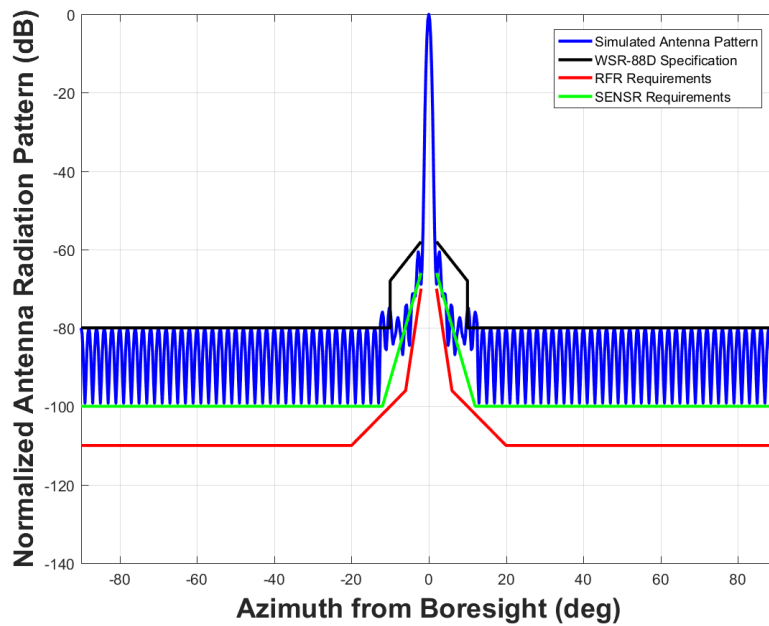


Fig. B.5 Simulated antenna radiation pattern (E in Table 3) with a peak sidelobe level of -60.6 dB, a far sidelobe level of -80 dB, and an integrated sidelobe level of -19.17 dB.

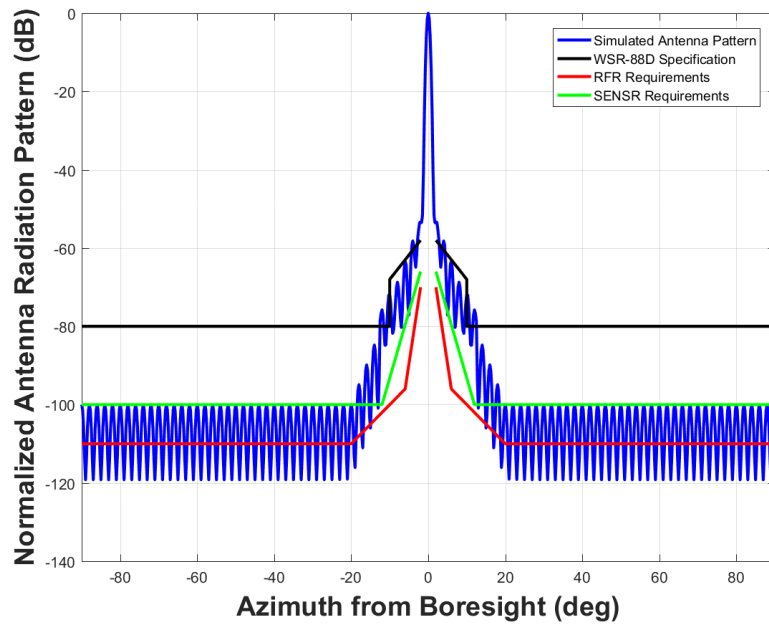


Fig. B.6 Simulated antenna radiation pattern (O in Table 3) with a peak sidelobe level of -53.3 dB, a far sidelobe level of -100 dB, and an integrated sidelobe level of -19.44 dB.

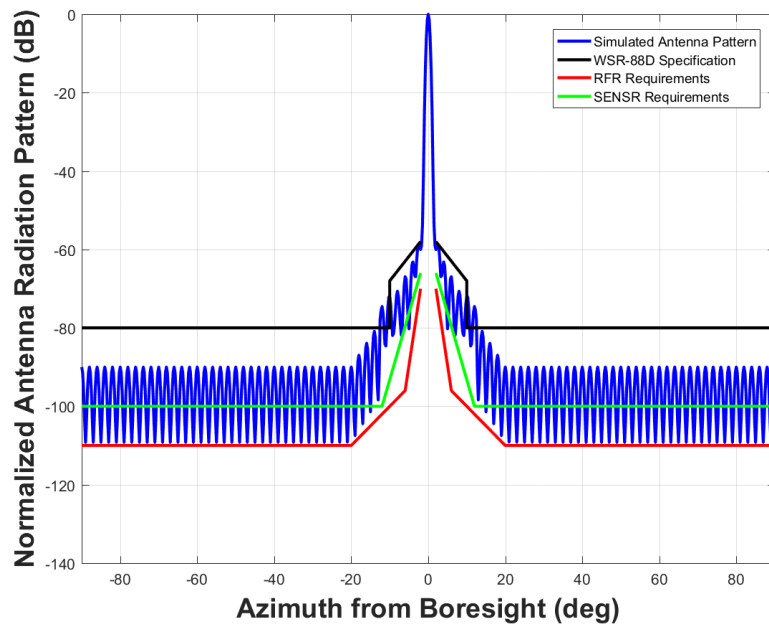


Fig. B.7 Simulated antenna radiation pattern (G in Table 3) with a peak sidelobe level of -58.9 dB, a far sidelobe level of -90 dB, and an integrated sidelobe level of -20.12 dB.

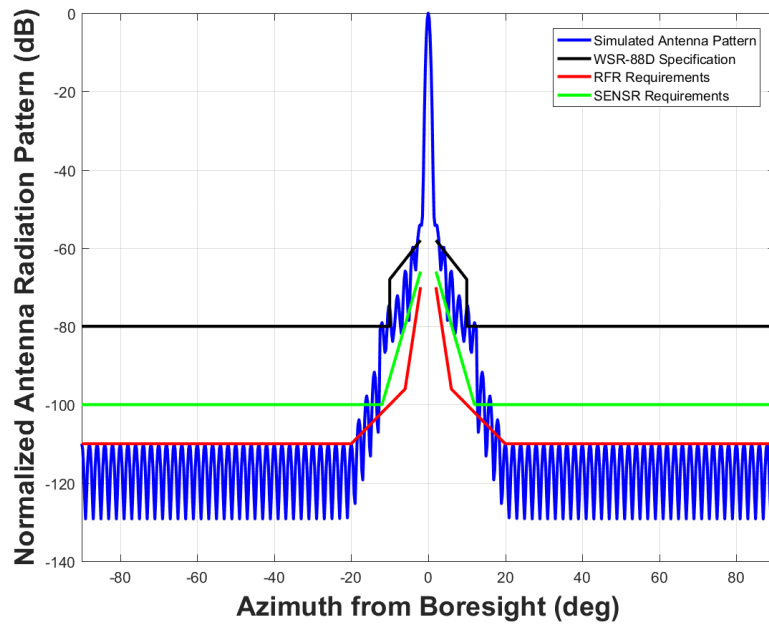


Fig. B.8 Simulated antenna radiation pattern (B in Table 3) with a peak sidelobe level of -54.1 dB, a far sidelobe level of -110 dB, and an integrated sidelobe level of -20.39 dB.

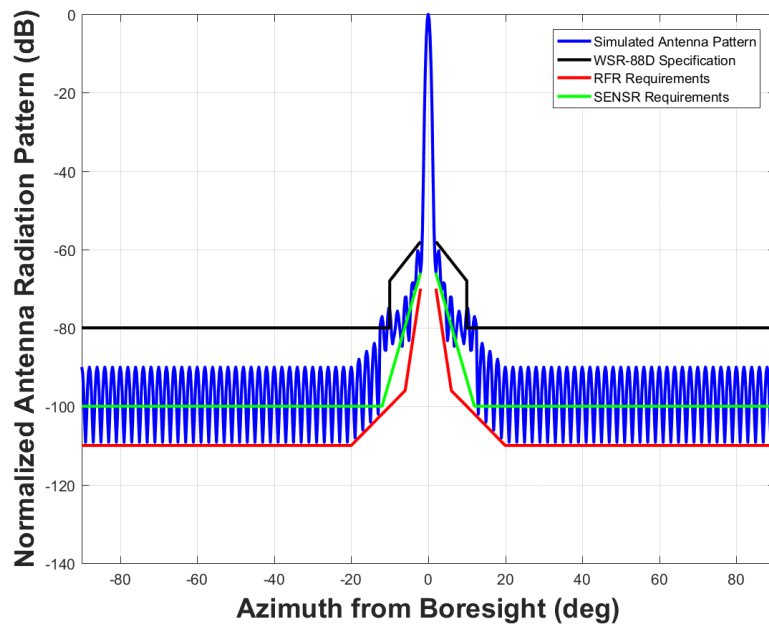


Fig. B.9 Simulated antenna radiation pattern (A in Table 3) with a peak sidelobe level of -60.3dB, a far sidelobe level of -90 dB, and an integrated sidelobe level of -21.38 dB.

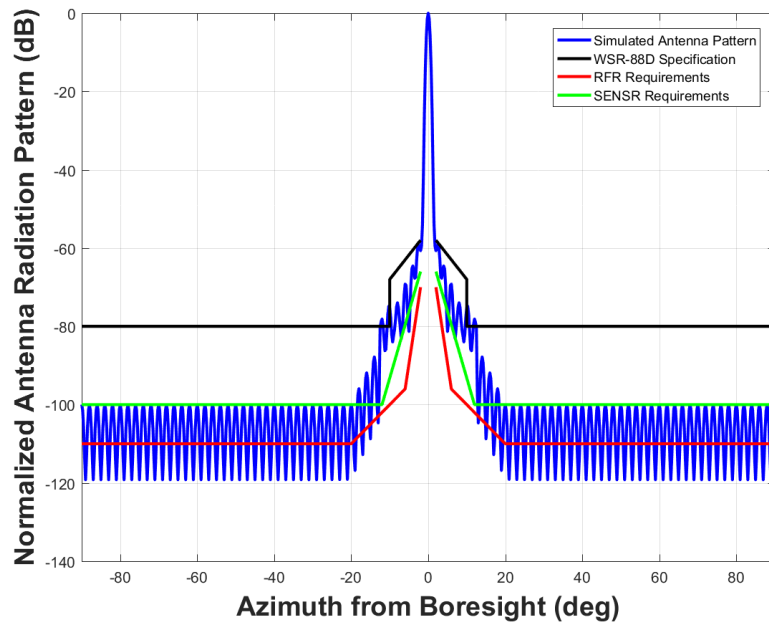


Fig. B.10 Simulated antenna radiation pattern (C in Table 3) with a peak sidelobe level of -59.2 dB, a far sidelobe level of -100 dB, and an integrated sidelobe level of -21.67 dB.

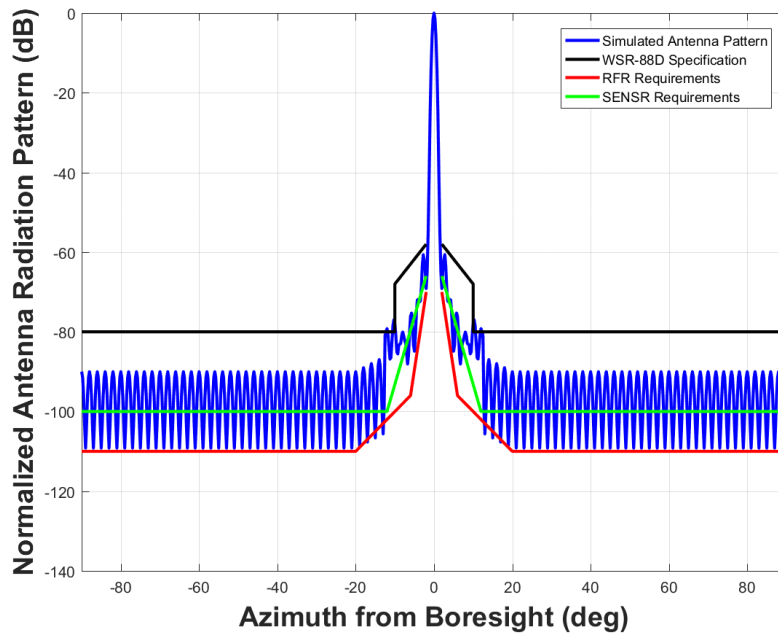


Fig. B.11 Simulated antenna radiation pattern (F in Table 3) with a peak sidelobe level of -60.6 dB, a far sidelobe level of -90 dB, and an integrated sidelobe level of -22.08 dB.

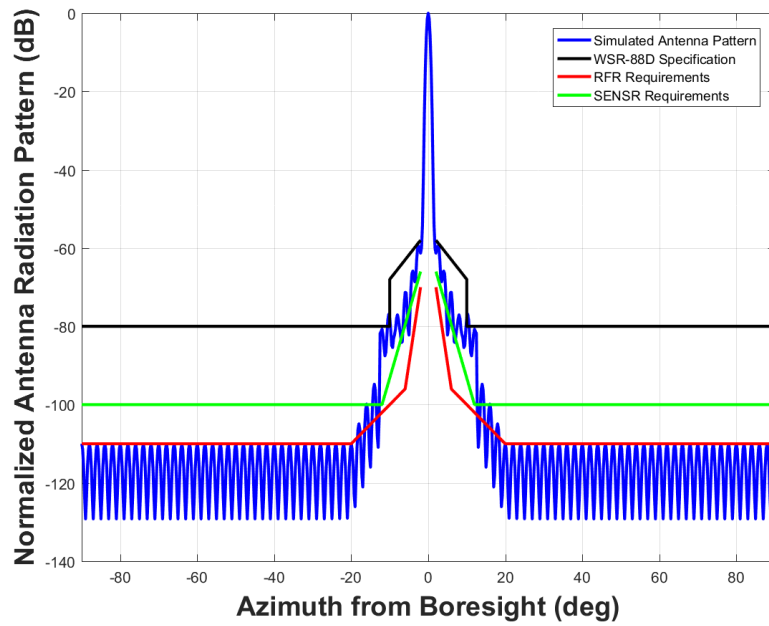


Fig. B.12 Simulated antenna radiation pattern (M in Table 3) with a peak sidelobe level of -59.5 dB, a far sidelobe level of -110 dB, and an integrated sidelobe level of -22.61 dB.

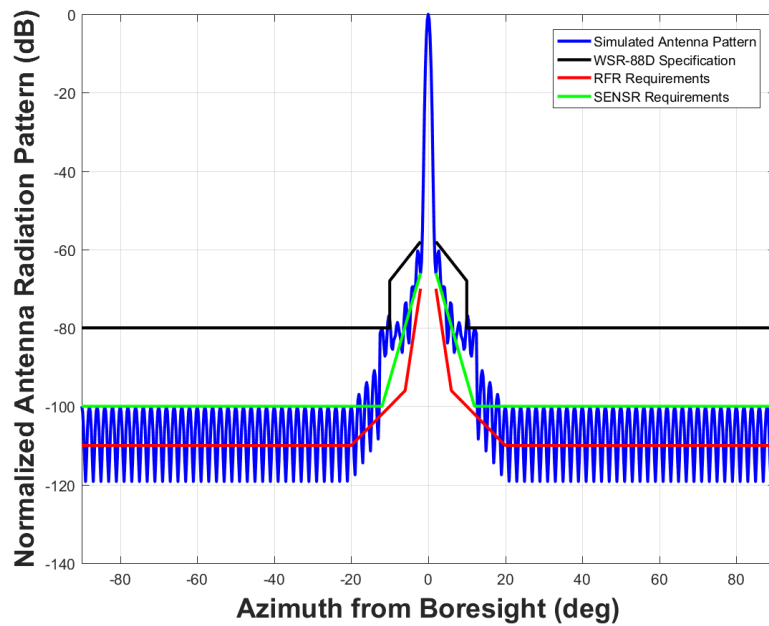


Fig. B.13 Simulated antenna radiation pattern (D in Table 3) with a peak sidelobe level of -60.3 dB, a far sidelobe level of -100 dB, and an integrated sidelobe level of -23.04 dB.

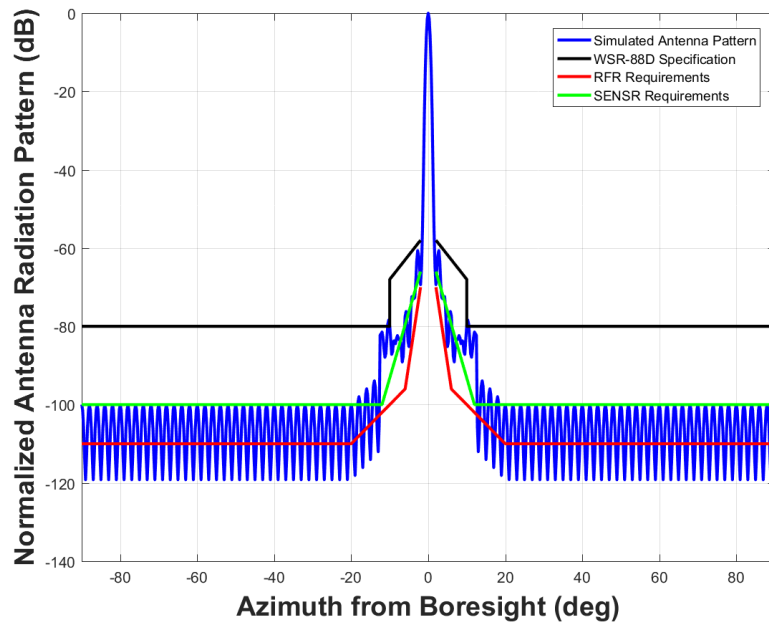


Fig. B.14 Simulated antenna radiation pattern (P in Table 3) with a peak sidelobe level of -60.6 dB, a far sidelobe level of -100 dB, and an integrated sidelobe level of -23.78 dB.

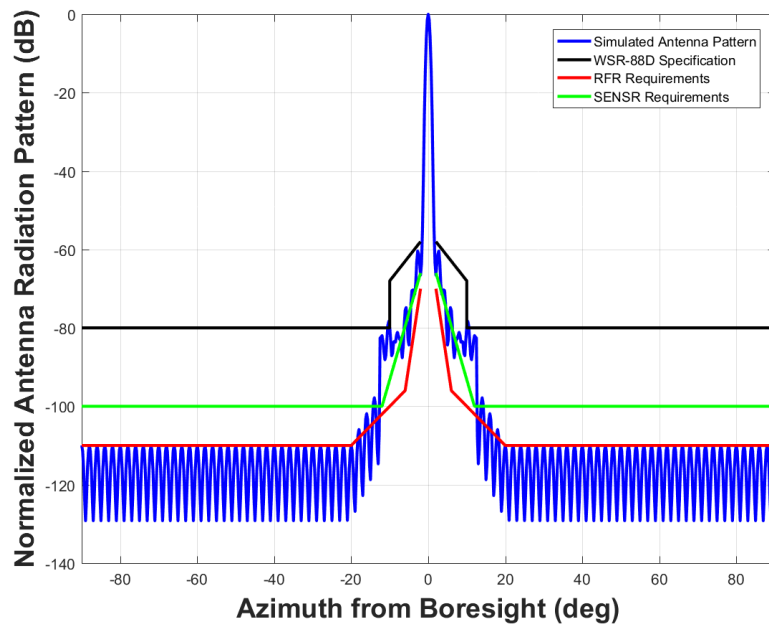


Fig. B.15 Simulated antenna radiation pattern (K in Table 3) with a peak sidelobe level of -60.4 dB, a far sidelobe level of -110 dB, and an integrated sidelobe level of -23.94 dB.

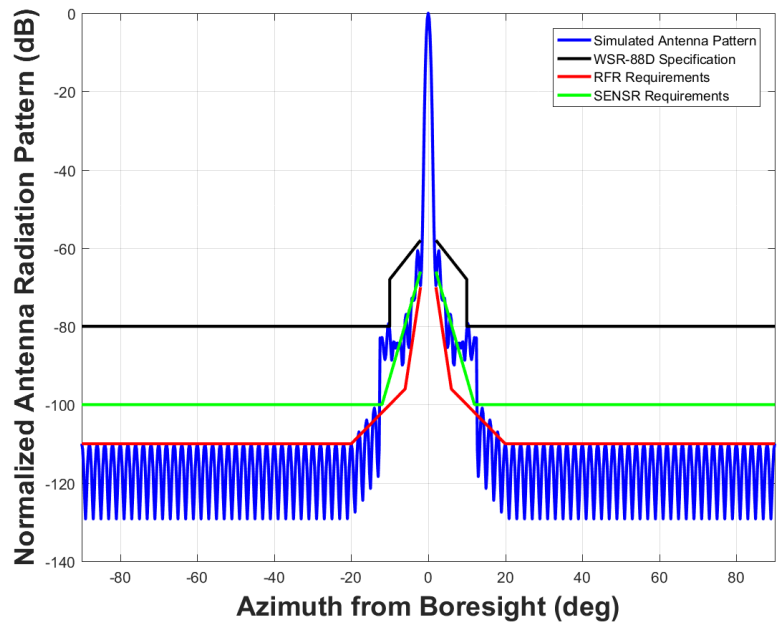


Fig. B.16 Simulated antenna radiation pattern (L in Table 3) with a peak sidelobe level of -60.6 dB, a far sidelobe level of -110 dB, and an integrated sidelobe level of -24.61 dB.

## References

- Doviak, R. J., and D. S. Zrnic, 1998: “Polarimetric Upgrades to Improve Rainfall Measurements”, Report and errata can be obtained online at [www.nssl.noaa.gov](http://www.nssl.noaa.gov), 120 pp.
- Federal Aviation Administration, 2017: Spectrum Efficient National Surveillance Radar (SENSR) Preliminary Performance Requirements, Accessed 20 April 2018, <https://faaco.faa.gov/index.cfm/attachment/download/75810>.
- National Weather Service, 2015: NOAA/National Weather Service Radar Functional Requirements, NOAA Reference Document.
- Radar Operations Center, 2017: NEXRAD Technical Information, Accessed 20 April 2018, <https://www.roc.noaa.gov/WSR88D/Engineering/NEXRADTechInfo.aspx>.
- Schwartzman, D, and C. Curtis, 2017: A realistic dual-polarization radar time-series simulator based on archived data. *Proc. 38th Conference on Radar Meteorology*, Chicago, IL, Amer. Meteor. Soc., 196.
- Weber, M. E., J. Y. N. Cho, J. S. Herd, J. M. Flavin, W. E. Benner, and G. S. Torok, 2007: The next-generation multimission U.S. surveillance radar network. *Bull. Amer. Meteor. Soc.*, **88**, 1739–1751.